Cavitation instabilities in amorphous solids: an athermal study

By

Umang Ashwin Dattani

PHYS10201704004

The Institute of Mathematical Sciences, Chennai

A thesis submitted to the

Board of Studies in Physical Sciences

In partial fulfilment of requirements

For the Degree of

DOCTOR OF PHILOSOPHY

of

HOMI BHABHA NATIONAL INSTITUTE

June, 2023

Homi Bhabha National Institute

Recommendations of the Viva Voce Board

As members of the Viva Voce Board, we certify that we have read the dissertation prepared by Mr. Umang Ashwin Dattani entitled “Cavitation instabilities in amorphous solids: an athermal study" and recommend that it maybe accepted as fulfilling the dissertation requirement for the Degree of Doctor of Philosophy.

Date: 04/10/2023

Chair - Prof. Sitabhra Sinha

Date: 04/10/2023

Guide/Convener - Prof. Pinaki Chaudhuri

Date: 04/10/2023

Member 1 - Prof. R. Rajesh

Date: 04/10/2023

Member 2 - Prof. Satyavani Vemparala

Date: 04/10/2023

Member 3 - Prof. C. M. Chandrashekar

Date: 04/10/2023

External Examiner - Prof. Saroj Kumar Nandi

Final approval and acceptance of this dissertation is contingent upon the candidate’s submission of the final copies of the dissertation to HBNI.

I hereby certify that I have read this dissertation prepared under my direction and recommend that it may be accepted as fulfilling the dissertation requirement.

Date: 04/10/2023

Place: IMSc, Chennai

Guide - Prof. Pinaki Chaudhuri

STATEMENT BY AUTHOR

This dissertation has been submitted in partial fulfilment of requirements for an advanced degree at Homi Bhabha National Institute (HBNI) and is deposited in the Library to be made available to borrowers under rules of the HBNI.

Brief quotations from this dissertation are allowable without special permission, provided that accurate acknowledgement of source is made. Requests for permission for extended quotation from or reproduction of this manuscript in whole or in part may be granted by the Competent Authority of HBNI when in his or her judgment the proposed use of the material is in the interests of scholarship. In all other instances, however, permission must be obtained from the author.

Dattani

Umang Ashwin Dattani

DECLARATION

I, hereby declare that the investigation presented in the thesis has been carried out by me. The work is original and has not been submitted earlier as a whole or in part for a degree / diploma at this or any other Institution / University.

Dattani

Umang Ashwin Dattani

List of Publications arising from the thesis

Published

“Universal mechanical instabilities in the energy landscape of amorphous solids: Evidence from athermal quasistatic expansion”,
Umang A. Dattani, *Smarajit Karmakar, and Pinaki Chaudhuri*,
Phys. Rev. E 106, 055004, 2022 .

“Athermal quasistatic cavitation in amorphous solids: effect of random pinning",
Umang A. Dattani, *Smarajit Karmakar, Pinaki Chaudhuri*,
accepted, Journal of Chemical Physics, 2023.

Submitted

“Cavitation instabilities in amorphous solids via secondary mechanical perturbations",
Umang A. Dattani, *Rishabh Sharma, Smarajit Karmakar, Pinaki Chaudhuri*,
arXiv:2303.04529, 2023.

Dattani

Communication of research: posters and talks

1. Presented a poster titled "Cavitation in amorphous solids: effect of pinning" at Indian Statistical Physics Community Meeting, ICTS, Bangalore, Feb 2020

2. Presented a online poster titled "Amorphous solids under athermal quasistatic expansion", at CECAM Mixed-Gen Season 2 session 5: simulating glasses, Feb 2022

3. Presented a poster titled "Amorphous solids under athermal quasistatic expansion", at the school "Disorder in complex systems" at Institut Pascal, Paris, June 2022

4. Delivered a talk titled “Amorphous solids under athermal quasistatic expansion" at PMMH, ESPCI, Paris, June 2022

5. Delivered a talk titled “Amorphous solids under athermal quasistatic expansion" at University of Göttingen, Germany, June 2022

6. Delivered a talk titled “Cavitation instabilities in amorphous solids" at workshop on Frontiers in Non-equilibrium Physics, IMSc, Feb 2023

7. Delivered a talk titled “Cavitation instabilities in amorphous solids" at APS March meeting, virtual session, March 2023.

8. Delivered a talk titled “Cavitation instabilities in amorphous solids" at the workshop ‘Interaction, Disorder & Elasticity’, Les Houches, France, April 2023

ACKNOWLEDGEMENTS

This thesis is the result of a six-year PhD, during which I have learnt a lot about physics, as well as about life. My time spent studying and living at IMSc has been truly rewarding in terms of both academic and non-academic associations. Today, when I look back, I am grateful to many people who have come across my journey and left an impression which deserves to be remembered.

First and foremost, I am extremely grateful to my supervisor, Pinaki Chaudhuri for his guidance, continuous support, and immense patience during my PhD. He has been my first window to the world of amorphous materials. His invaluable feedback on academic matters has helped me grow a lot. Along with my supervisor, I would also like to express gratitude to our collaborator Smarajit Karmakar. His inputs on our research have been immensely useful. Our joint discussions with Pinaki on physics have helped me learn a lot about my research area and about doing research.

Besides my supervisor, I would like to thank Sitabhra, Rajesh, Vani and Chandrashekhar for their useful inputs as a part of my doctoral committee. Course on Statistical Mechanics in the first semester by Sitabhra was really inspiring. I would also like to thank Purusattam for introducing the subject of soft-matter physics and for his encouragement at various points of time.

I am thankful to my colleagues Arjun, Sayantan, Suman & Vinay. The time spent with them in group discussions has been pivotal in improving my understanding of my PhD subject. They have also been instrumental in helping me learn various numerical techniques at different points of time. I would specially like to mention Sayantan for all the insightful discussions on a wide-range of topics at various points and for all the fun during our outings.

Apart from the research, IMSc has been a great place for exploring other activities too. The time spent mostly in playing cricket has added a great amount of balance to my

life. I convey my heartiest thanks to my regular fellow sport-mates Raghvendra, Sahil, Bhargava, Devanand, Rajesh, Soham, Rakesh, Gopal, Mahaveer, Hitesh, Anuj, Vijay & Vishwajeet for making the on-field cricket time memorable.

I would like to express my special thanks to my beloved friend Aparna for the love, trust and constant support during my PhD, who is now my wife.

Finally, I am thankful to my parents and parents-in-law for their love and support without whom it would be impossible to achieve my PhD.

Synopsis

Introduction

Amorphous solids are ubiquitous in nature. They are known to exist in diverse forms, ranging from hard solids like metallic glasses, polymeric glasses etc. to soft solids like gels, emulsions, colloidal glasses, biological tissues etc. Even though they have widespread applications, understanding the physical processes leading to their failure still remains a challenge. Due to the disordered structure of the amorphous solids, the notion of defects from which the failure stems is difficult to understand unlike the case of their crystalline counterparts where the defects are well defined. There also exists diversity in the failure-mechanisms of amorphous solids. The soft-solids fail in a ductile manner whereas, the hard-solids fail in a brittle manner even though both share similarities in their mechanical responses. Therefore, understanding failure of amorphous solids is a complex challenge.

Formation of voids in a material via some mechanical process is usually referred to as cavitation. In many cases of failure in amorphous solids, these cavitation instabilities are known to play a major role. Amorphous solids breaking via propagation of cavities at nano-scale has been observed in numerous fracture experiments[6, 19] and recently, has also been studied in numerical simulations[2, 7, 11, 16]. Despite these studies, the phenomenon has not received much theoretical attention, unlike the case of cavitation in liquids[5]. Understanding how cavitation occurs and leads to fracture in amorphous solids would not only shed light on the physics of failure of these solids but also on the problem of making better and stronger glasses.

In the temperature-density phase diagram of cohesive glass-forming liquids, the phase coexistence of liquid and gas is marked by a binodal line which marks the beginning of phase separation by nucleation and a spinodal line which marks the beginning of phase separation via spinodal-decomposition[20]. For glass-forming liquids, the glass transition line in $T-\rho$ plane was shown to cut the spinodal at finite temperatures[18], implying the existence of a mechanical instability at the intersection and also a gas-glass coexistence region below the glass-transition temperature of the coexisting liquid. Cavitation instabilities in amorphous solids stem from this glass-gas coexistence and manifest when the amorphous solid is driven into this region. Recently, several studies involving numerical simulations have explored different aspects of the cavitation process; which include, computing nucleation barriers[11], role of expansion rates and consequent hysteresis[7], failure under confinement via uniaxial tension at nanoscales[16], probing the nature of the cavitation transition on the energy landscape of high-temperature liquids in models with varying degree of cohesion [1, 2]. However, major understanding of these cavitation instabilities from the point of view of amorphous plasticity and from the potential energy landscape is still lacking, and in our work, we attempt to bridge that gap.

In this thesis, we aim to study cavitation instabilities under different settings as summarised in Figure. 1. In the first part, we study the elasto-plastic response of an amorphous solid under athermal quasistatic expansion which results in cavitation of the solid[2]. In the second part, we investigate the effect of combinations of uniform expansion with cyclic shear, as illustrated. In the third part, we explore a way to make stronger glasses resistant to cavitation via pinning a small fraction of particles in the solid.

Athermal quasistatic expansion: elasto-plastic phenomenology

The potential energy landscape (or PEL) of amorphous solids is extremely rugged and it has been shown by various studies, how the observed properties of these materials are

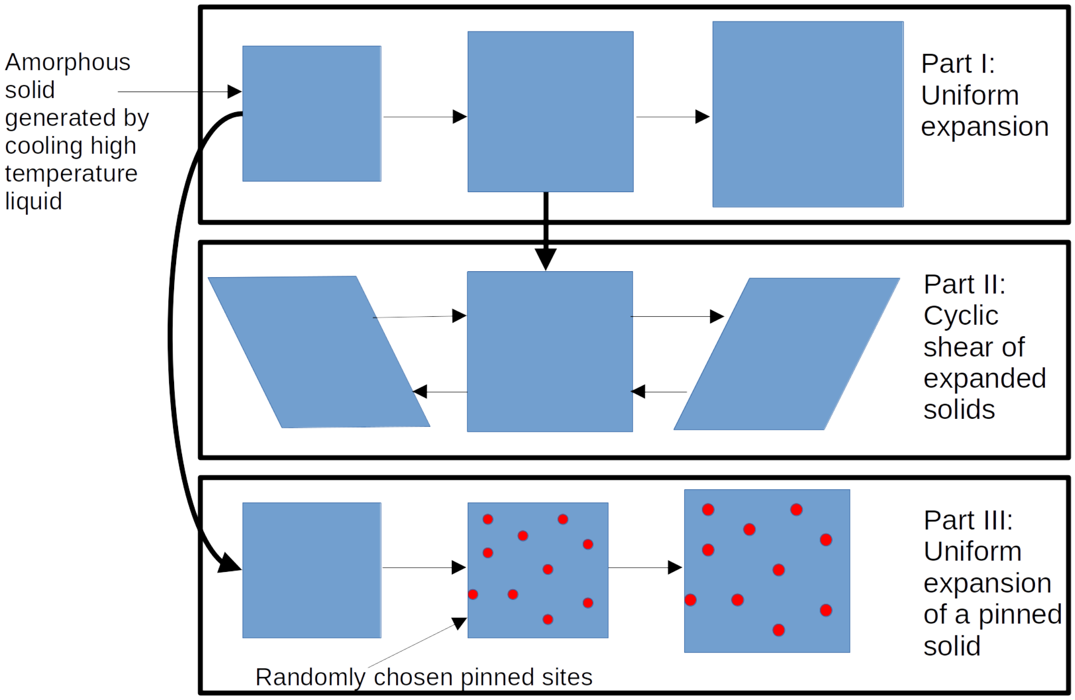
Amorphous solid generated by cooling high temperature liquid
Part I: Uniform expansion
Part II: Cyclic shear of expanded solids
Part III: Uniform expansion of a pinned solid
Randomly chosen pinned sites

Figure 1: Schematic illustrating the three different directions of study explored in this thesis, and there inter-linking.

connected to the features of this landscape. In the case of mechanical response of the amorphous solids, it has been shown that upto a certain temperature below the glass-transition, the behaviour is determined by the PEL.

Purely mechanical response of the solid in absence of thermal fluctuations and vanishing strain rates, i.e. $T \rightarrow 0$ and $\dot{\gamma} \rightarrow 0$, is studied via athermal quasistatic protocols, the most common one being athermal quasistatic shear[14]. In numerical simulations, the potential energy can be computed from the interactions and is therefore accessible during deformations. Hence, athermal quasistatic protocols allow us to decipher the mechanism of plasticity on the PEL(via potential and its derivatives) and calculate avalanche size distributions with ease.

In our work[8], we therefore subject a spatially homogenous model amorphous solid to athermal quasistatic expansion. This allows us to drive the system into gas-glass coexistence region under athermal conditions. Starting with an amorphous solid obtained by cooling a high-temperature liquid, we apply homogenous constant strain $d\gamma$ on the solid in each step by rescaling the coordinates, which is then followed by relaxation to nearest local minimum via energy minimization. This ensures the limit, temperature $T \to 0$ and strain rate $\dot{\gamma} \to 0$.

We find that upon expansion, the pressure of the solid decreases. Beyond a certain point, it even becomes negative. After crossing a certain density threshold, the solid undergoes cavitation accompanied by a large jump in pressure(and a drop in energy). Upon further expansion, these cavities grow via smaller pressure jumps and eventually result in system spanning fracture of the solid. The pressure susceptibility defined as size independent fluctuations of pressure $\chi_p(\rho) = N\left(\langle P^2(\rho)\rangle - \langle P(\rho)\rangle^2\right)$ at a given density shows a peak at the first big cavitation event. We find that the peak height scales extensively with the system size suggesting a macroscopic stress drop which has been seen for the case of brittle-yielding under shear[15, 17].

The cavitation occurs via irreversible/plastic events accompanied by a pressure jump and an energy drop. We look at the stability of the system near irreversible pressure jumps on the potential energy landscape by monitoring the lowest eigenvalues of the Hessian of the potential energy. In the context of shear, at each irreversible rearrangement/plastic event, the lowest non-zero eigenvalue of the Hessian is known to vanish as $\lambda_{min} \sim \sqrt{\gamma_c - \gamma}$. In our work, we find that near all the plastic events, the lowest nonzero eigenvalue of the Hessian vanishes as square root of difference in density from the critical density i.e. $\lambda_{min} \sim \sqrt{\rho - \rho_c}$. This corresponds to a saddle-node bifurcation on the potential energy landscape as shown in the context of plastic events under shear[14]. The fact that only one eigenvalue goes to zero, also manifests in the fact that, near the plastic events, the spatial map of the eigenmode corresponding to vanishing eigenvalue mimics the displacement field near plastic events. However, the displacement field across the plastic jump though has a much smaller overlap with the eigenmode just before the plastic drop, which suggests avalanche/cascade nature of the plastic jump. The main cavitation events and the merging of cavities towards the fracture occurs via these avalanches.

To get an estimate of size of avalanches that lead to fracture, we look at the statistics of pressure jumps ΔP and energy drops ΔU for different system sizes after the first main caviation event. It turns out that the distributions of both pressure jumps and energy drops collapse on scaling the arguments ΔP & ΔU by exponents -0.34 and 0.53 respectively. The mean values too scale with the same exponents. The statistics therefore reveal that the post-yield plasticity under expansion is scale free and sub-extensive but the distributions and exponents for avalanche sizes of cavitation instabilities are different from size of plastic events under shear.

We find that in the pre-yield region too, λ_{min} goes to zero multiple times. These events too show a saddle-node bifurcation via a square-root vanishing of the λ_{min}. The displacement fields corresponding to these pre-yield plastic events that occur in absence of large density inhomogeneities, show a Eshelby-like quadrupolar shape as seen in plastic events under shear. This suggests that, even under expansion, shear stress relaxation occurs.

To summarise, our work explores the phenomenology of response of amorphous solids to athermal quasistatic expansion and connects it to the phenomenology of well-studied athermal quasistatic shear in previous studies[14].

Cavitation instabilities under secondary cyclic shear deformations

In our previous work, we have studied the elasto-plastic response of amorphous solids under uniform expansion. As we have shown, under uniform expansion, the pressure of the solid decreases on expansion, as the expansion is continued, it becomes negative and eventually leads to a pressure jump and cavitation of the solid. The negative pressure states around the liquid-gas coexistence are known to be metastable and short-lived. But in our case, the liquid has solidified into an amorphous solid, so whether these negative pressure states would be stable to other driving mechanism or not is a question of interest. In our previous work, we have also observed some characteristics of shear relaxation, especially Eshelby-like quadrupolar displacement fields for pre-yield events. The real-life scenarios of loading of amorphous solids also involve combinations of different deformations. Based on these observations, we examine the stability of these spatially homogeneous states, obtained during an expansion trajectory, to an additional drive, viz. macroscopic cyclic shear deformation[13] which we refer as secondary deformation[9].

We find that upon cyclic deformation, the solid starts to cavitate at higher densities depending upon the magnitude of cyclic shear amplitude. We summarise this dependence of cavitation on the amplitude of cyclic shear in a two-parameter phase diagram with density and amplitude of cyclic shear γ_{max} as control parameters. We observe that higher amplitudes cavitate the solid at higher densities and vice-versa. Further, a spatial analysis of these inhomogeneous structures reveals that the location of cavities for the same trajectory at different points in the phase diagram is usually not the same. This implies the existence of abundant cavitation modes in $P < 0$ region. We also find that for higher amplitudes of cyclic shear, cavitation occurs via system spanning avalanches like spatial structures that look like shear bands seen in the shear response of amorphous solids.

A pertinent question to ask is whether cavitation via the secondary cyclic shear leads to largescale irreversible plasticity. So we track the stroboscopic steady-state energy with shear-cycles. It shows a cusp at the yielding amplitude as seen in studies of cyclic shear of dense amorphous solids[3]. The yield amplitudes determined from the cusp are marked in the $\gamma_{max} - \rho$ phase diagram. The cavitation occurs both below and above this yielding line. At higher densities, the cavitation occurs above the yield amplitude and at lower densities, it occurs below the yield line too. We also note that the stroboscopic relaxation of the energy with cycles shows that the system relaxes to a absorbed state or a limit cycle for low γ_{max}. At a fixed density, as the amplitude is increased, the number of cycles required to reach a limit cycle diverges, viz. $\tau_{rel} \approx (\gamma_{yield} - \gamma_{max})^{-2.8}$ as observed in Ref[12].

To summarise, our study establishes that, under secondary deformation, the expanded solid cavitates much earlier and at lower energy thresholds. This establishes an enhanced coupling of the cyclic shear deformation to cavitation instabilities as compared to the uniform expansion. This early onset of cavitation occurs both below and above the yielding under cyclic shear which is summarised in a two parameter phase diagram. We have also found that below the yielding amplitudes, the plasticity is localised in the region of cavity where as for amplitudes around & above the yield, the plasticity occurs via avalanches which may system-spanning in many cases. Analogous results of cavitation at higher densities under local random deformation via activity have been obtained by our collaborators, which has been reported in our collaborative manuscript[9].

Effect of pinning on cavitation in amorphous solids

As discussed in the introduction, cavitation instabilities play a crucial role in the fracture of amorphous solid. Therefore, understanding how cavitation can be avoided or restricted is central to making better and stronger glasses. In this context, a recent study[4] had shown how pinning a small fraction of particles delays the sharp heterogeneous yielding transition under simple shear and makes it more spatially homogeneous. Micro-alloying via addition of a small-fraction of foreign particles in solids has been known to dramatically alter the properties of a material[10, 21]. These pinned sites are a simple way to model seeded inclusions which are often used to make the solid stronger. In our work, we explore how the cavitation occurs under uniform expansion when a small fraction of particles in the solid are pinned.

Starting from an amorphous solid generated by cooling a high temperature liquid, we randomly choose a small fraction of particles for pinning. We deform this pinned solid via athermal quasistatic expansion which is outlined above. Upon expansion, we find that the big pressure jump, observed in the solid without pinned particles, is absent in the solid with pinning. The small pressure jumps end up creating small cavities throughout the solid as opposed to one or two cavities as seen in the unpinned case. At the same time, energy of the pinned solid does not show a large jump either at the cavitation point; instead, the average energy just keeps increasing with expansion. This suggests that pinning blocks the pathways of relaxation that are present in the unpinned solid.

As studied in the first part, we look at the eigenvalues of the Hessian of potential energy near plastic instabilities; the lowest eigenvalue λ_{min} goes to zero near the plastic events and the displacement fields on approach to the instabilities are predicted by eigenmode of the vanishing eigenvalue. This is consistent with the scenario of saddle-node bifurcation which we have showed for unpinned solids under uniform expansion. Here too, the displacement field across the drop shows signs of a cascade as discussed above.

To understand the response of pinned solids under expansion, we look at angle-averaged profile of the spatial displacements $e(r)$ in eigenmodes of λ_{min} near a plastic instability, as these modes are known to trigger the plasticity. For an unpinned solid, the decay is long-ranged i.e. $e(r) \sim 1/r$. For pinned solids, we find two different regimes of $e(r)$ depending upon concentrations. For lower pinning concentrations, we observe a screened profile, viz. $e(r) \sim \exp(-r/\xi)/r^{\eta}$, whereas for larger c, we see purely exponential relaxation, $e(r) \sim \exp(-r/\xi)$. The exponential decays allows us to extract the length scale ξ which decreases with increasing pinning concentration c. This effect of suppression of long-range nature of the eigenmodes that leads to plasticity in pinned solids, is also reflected in the average pressure-jump size and average energy drop size which decreases with increasing pinning concentration and are much smaller their pinned counterparts. We have also looked at the system-size effects in the pressure-density and energy-density curves. Unlike the case of unpinned solids, the pinned solids have little to no finite size dependence just like a ductile solid: the pressure-density and energy-density curves for different system sizes fall on top of each other. Due to the presence of an intrinsic length scale in pinned solids, the system size does not seem to matter.

Our work thus shows a possible way to make amorphous solids which can resist the cavitation instabilities better. We explain the observed response of pinned amorphous solids by a length scale of plasticity extracted from the eigenmodes just before a plastic event. Our study thus paves the way to make better and stronger glasses via use of inclusions.

Summary

Our work, using numerical simulations, explores the scenarios under which the cavitation instabilities arise in the athermal limit. In the first part, under athermal quasistatic expansion, we have found numerous similarities with the response of amorphous solids under shear *viz.* plasticity via saddle-node bifurcation on potential energy landscape, scale-free and sub-extensive scaling of plastic pressure jumps as well as energy drops and presence of pre-yield Eshelby-like quadrupolar plastic events. In the second part of our work, we have explored combination of uniform expansion with cyclic shear to realise the scenarios in which these instabilities could arise. Our work shows that deformation modes like shear are energetically favorable routes to cavitation suggesting an enhanced coupling of shear to cavitation instabilities when the solid is under tension due to expansion. In the third part of our work, we have looked at the response of the amorphous solid to expansion in the presence of pinning. We show that pinning a small fraction of particles delays the cavitation and makes the cavitation more homogeneous throughout the system. We extract a novel length scale ξ from the decay profile of eigenmodes near a plastic instability and show that ξ decreases with increasing fraction of pinning sites which explains the observed spatial homogenisation of cavitation. Our work thus establishes a major set of results in understanding cavitation instabilities in amorphous solids and also connects it with the extensively studied shear response of amorphous solids. Our work also explores a possible way to make stronger amorphous solid that are more resistant to these cavitation instabilities.

References

[1] ALTABET, Y. E., FENLEY, A. L., STILLINGER, F. H., AND DEBENEDETTI, P. G. Cavitation transition in the energy landscape: Distinct tensile yielding behavior in strongly and weakly attractive systems. *The Journal of Chemical Physics 148*, 11 (2018), 114501.

[2] ALTABET, Y. E., STILLINGER, F. H., AND DEBENEDETTI, P. G. A cavitation transition in the energy landscape of simple cohesive liquids and glasses. *The Journal of Chemical Physics 145*, 21 (2016), 211905.

[3] BHAUMIK, H., FOFFI, G., AND SASTRY, S. The role of annealing in determining the yielding behavior of glasses under cyclic shear deformation. *Proceedings of the National Academy of Sciences 118*, 16 (2021), e2100227118.

[4] BHOWMIK, B. P., CHAUDHURI, P., AND KARMAKAR, S. Effect of pinning on the yielding transition of amorphous solids. *Phys. Rev. Lett. 123* (Oct 2019), 185501.

[5] CAUPIN, F., AND HERBERT, E. Cavitation in water: a review. *Comptes Rendus Physique 7*, 9-10 (2006), 1000–1017.

[6] CÉLARIÉ, F., PRADES, S., BONAMY, D., FERRERO, L., BOUCHAUD, E., GUILLOT, C., AND MARLIÈRE, C. Glass breaks like metal, but at the nanometer scale. *Phys. Rev. Lett. 90* (Feb 2003), 075504.

[7] CHAUDHURI, P., AND HORBACH, J. Structural inhomogeneities in glasses via cavitation. *Phys. Rev. B 94* (Sep 2016), 094203.

[8] DATTANI, U. A., KARMAKAR, S., AND CHAUDHURI, P. Universal mechanical instabilities in the energy landscape of amorphous solids: Evidence from athermal quasistatic expansion. *Phys. Rev. E 106* (Nov 2022), 055004.

[9] DATTANI, U. A., SHARMA, R., KARMAKAR, S., AND CHAUDHURI, P. Cavitation instabilities in amorphous solids via secondary mechanical perturbations. *arXiv:2303.04529* (Mar 2023).

[10] DEMETRIOU, M. D., LAUNEY, M. E., GARRETT, G., SCHRAMM, J. P., HOFMANN, D. C., JOHNSON, W. L., AND RITCHIE, R. O. A damage-tolerant glass. *Nature materials 10*, 2 (2011), 123–128.

[11] GUAN, P., LU, S., SPECTOR, M. J. B., VALAVALA, P. K., AND FALK, M. L. Cavitation in amorphous solids. *Phys. Rev. Lett. 110* (Apr 2013), 185502.

[12] KUMAR, D., PATINET, S., MALONEY, C. E., REGEV, I., VANDEMBROUCQ, D., AND MUNGAN, M. Mapping out the glassy landscape of a mesoscopic elastoplastic model. *The Journal of Chemical Physics 157*, 17 (2022), 174504.

[13] LEISHANGTHEM, P., PARMAR, A. D., AND SASTRY, S. The yielding transition in amorphous solids under oscillatory shear deformation. *Nature communications 8*, 1 (2017), 14653.

[14] MALONEY, C. E., AND LEMAÎTRE, A. Amorphous systems in athermal, quasistatic shear. *Phys. Rev. E 74* (Jul 2006), 016118.

[15] OZAWA, M., BERTHIER, L., BIROLI, G., ROSSO, A., AND TARJUS, G. Random critical point separates brittle and ductile yielding transitions in amorphous materials. *Proceedings of the National Academy of Sciences 115*, 26 (2018), 6656–6661.

[16] PAUL, K., DASGUPTA, R., HORBACH, J., AND KARMAKAR, S. Cavity formation in deformed amorphous solids on the nanoscale. *Phys. Rev. Res. 2* (Oct 2020), 042012.

[17] RICHARD, D., RAINONE, C., AND LERNER, E. Finite-size study of the athermal quasistatic yielding transition in structural glasses. *The Journal of Chemical Physics 155*, 5 (2021), 056101.

[18] SASTRY, S. Liquid limits: Glass transition and liquid-gas spinodal boundaries of metastable liquids. *Phys. Rev. Lett. 85* (Jul 2000), 590–593.

[19] SHEN, L.-Q., YU, J.-H., TANG, X.-C., SUN, B.-A., LIU, Y.-H., BAI, H.-Y., AND WANG, W.-H. Observation of cavitation governing fracture in glasses. *Science Advances 7*, 14 (2021), eabf7293.

[20] TESTARD, V., BERTHIER, L., AND KOB, W. Intermittent dynamics and logarithmic domain growth during the spinodal decomposition of a glass-forming liquid. *The Journal of Chemical Physics 140*, 16 (2014), 164502.

[21] WANG, W. H. Roles of minor additions in formation and properties of bulk metallic glasses. *Progress in materials science 52*, 4 (2007), 540–596.

List of Figures

1.1 Schematic showing different types of structural order in solids; source: Ref [1] 11

1.2 A figure from Ref [2] showing diverse amorphous solids. Their constituent particle sizes are shown on the X-axis and the Y-axis shows the dynamics of these solids. 12

1.3 Left: Dependence of the enthalpy/volume upon temperature for crystalline and glass-forming systems [6]. Right: Dependence of relaxation timescales on temperature for different glass-forming systems [5]. 14

1.4 A schematic of a patch of potential energy landscape of amorphous solids from Ref [8] 16

1.5 (a) A schematic of shear deformation on the simiulation box (b) Algorithm of the AQS protocol. 20

1.6 (a) A typical stress-strain curve seen under AQS. (b) A quadrupolar displacement field corresponding to irreversible particle rearrangements in AQS. 21

1.7 A schematic of a sadlle-node bifurcation. 22

1.8 A schematic illustrating the protocol of cyclic shear. 22

1.9 Image taken from Ref [44]. Effect of different level of annealing on the cyclic shear response of a model amorphous solid. 24

1.10 A schematic of an amorphous solids undergoing fracture via coalesence of cavities as reported in multiple experimental studies. 25

1.11 A schematic phase diagram of an attractive glass-forming system in the (temperature)$T - \rho$(density) plane. 26

1.12 A schematic summarising the directions that we explore in this thesis . . 30

2.1 A figure illustrating distance calculation between two particles under periodic boundary conditions for a square box. 43

2.2 A figure illustrating distance calculation between two particles under periodic boundary conditions for a sheared triclinic box. 44

3.1 For different system sizes and averaged over ensembles, (a) Pressure P vs Density ρ curve (b) Energy per particle U/N vs Density ρ (c) Pressure susceptibility, inset: system-size scaling of the pressure susceptibility peak, $\chi_p^{peak} \sim N$ (d) Energy susceptibility, inset: system-size scaling of the energy susceptibility peak, $\chi_u^{peak} \sim N$ (e) Density dependence of the first and second peaks in the susceptibility. 53

3.2 For a trajectory of $N = 10^5$, (a) The pressure jumps marked in red on the $P - \rho$ curve (b)-(g) Snapshots of the solid at the points marked in (a). . . 54

3.3 (a) The lowest non-zero eigenvalue of the Hessian of potential energy λ_{min} vs density ρ (b) The corresponding patch of P-ρ trajectory (c) Near the pressure-jumps marked in (a), λ_{min} as a function of $(\rho-\rho_c)/\rho_c$ for different models of amorphous solids (1) 2D Kob-Andersen model(shown in (a) & (b)) (2) Model from Lancon et al. (3)3D Kob-Andersen (4) Wahnstorm mixture in 3D. Columns (d) & (e) show the spatial maps of eigenvectors of λ_{min} and the corresponding displacement map on approach to a plastic jumps marked jumps in (a). 56

3.4 A schematic illustrating the mechanism of saddle-node-bifurcation on the potential energy landscape. 57

3.5 For the yielding avalanche: (a) Spatial map of the eigenvector on approach to the yielding pressure jump (b) Displacement fields on approach to the yielding pressure jump (c) Displacement fields across the yielding pressure jump. 59

3.6 For different system-sizes: (a) Distributions of pressure jumps ΔP in the post-yield regime; (b) Distributions of energy drops ΔU in the post-yield regime; (c) Collapse of the pressure distributions on scaling the pressure drops with a factor $N^{0.53}$, the small-strain values of the pressure-distribution obey a power law, $P(\Delta P) \sim (\Delta P)^{0.91}$; (d) Collapse of the pressure distributions on scaling the pressure drops with a factor $N^{0.53}$, the small-strain values of the energy-distribution obey a power law, $P(\Delta U) \sim (\Delta U)^{0.93}$. 60

3.7 For the plastic events in the pre-yield branch of $P - \rho$: (a) The lowest non-zero eigenvalue of the Hessian of potential energy, λ_{min} as a function of density; (b) Vanishing of the eigenvalue as a square-root near a plastic event for different system sizes; (c) Eigenmode on approach to the plastic event; (d) Displacement field on approach to plastic event; (d) Coarse-grained density field of the solid after the event showing no density-inhomogenieties. 61

4.1 A schematic diagram of the protocol followed in our study: states generated during the expansion from a dense spatially homogeneous amorphous solid are subjected to secondary deformations in the form of a cyclic shear. 68

4.2 Early onset of cavitation: (a) Phase diagram showing the region where cavitation (marked in green) occurs under cyclic shear in the γ_{max}-ρ plane. (b) For $\gamma_{max} = 0.06$, pressure jumps corresponding to a cavitation under cyclic shear at higher densities marked on the uniform expansion trajectory in the pressure (P) vs density (ρ) plane. The inset shows the evolution of pressure with the cycles of cyclic shear (c) The energy drops corresponding to the pressure jumps in (b) are marked on the uniform expansion trajectory in the energy per particle (U/N) vs density (ρ) plane (d) Energy per particle (U/N) as a function of shear strain within the first cycle of cyclic shear. The black horizontal line on the top marks the energy at which cavitation occurs under expansion and the evolution of the energy per particle U/N with cycles is shown in the inset. 71

4.3 (a) Stroboscopic evolution of scaled energy (defined in the text) with cycles of cyclic shear (b) Mean values of scaled energy in last 20 cycles of (a) for different amplitudes of cyclic shear (c) Number of cycles required to reach a steady state τ_{rel} or a limit cycle as a function of amplitude of cyclic shear(γ_{max}) for different densities. 73

4.4 Evolution of energy per particle (U/N) within the shear cycles for : (a) a case where the system reaches an absorbing state; (b) a case where the energy per particle remain diffusive. The red curve in both the figures marks the first cycle of cyclic shear, the blue curve marks the 200^{th} cycle and the green curves show the intermediate cycles. 75

4.5 Demonstration of observed limit cycles of period two: (a) Stroboscopic evolution of re-scaled energies with cycles of cyclic shear; (b) Energy per particle (U/N) within the cycle as a function of shear strain; (γ) for one of the cases showing the two curves between which the system alternates. 75

4.6 Coarse-grained density fields at different points in the phase diagram (Figure 4.2 76

4.7 Amplitude dependence of plasticity maps at a given density 77

5.1 For $N = 10^5$ and different pinning concentrations, c, as marked: Variation with density ρ of (a) Pressure P (b) Energy per particle U/N (c) Pressure susceptibility χ_P (d) Energy susceptibility χ_U. Change in (e) average size of pressure jump ΔP, and (f) average size of energy drops ΔU, with pinning concentration. 88

5.2 Density field for different pinning concentrations, $c = 0.00$ (a), 0.01 (b), 0.02 (c), 0.05 (d), measured at $\rho = 0.982$. 89

5.3 Left panel: The ensemble averaged pressure(P) vs density (ρ) curves for different system sizes at the specified values of pinning concentrations (as marked). Right panel: Pressure susceptibility χ_p vs density ρ plots corresponding to the left panel plots 90

5.4 (a) Pressure P vs density ρ for an expansion trajectory, using $N = 2500$, corresponding to $c = 0.05$. (b) Demonstration of square-root singularity for lowest eignevalue of the Hessian, $\lambda_{\rm min}$ (appropriately scaled by fit parameter A), computed at the density points in (a) corresponding to occurrence of plastic instabilities; ρ_c is the estimate density location of the event in each case. (c) Eigenmode, (d) displacement field just before the drop and (e) displacement fields across the plastic drop, occurring at one such plastic event, near $\rho \approx 1.03277$. 92

5.5 (a)-(e) Evolution of the density field across an expansion trajectory for the points marked in Figure 5.5(a). 93

5.6 (a) Spatial decay profile of magnitude of displacements in the eigenmode before the yielding, $e(r)$, leading to the plastic events, shown for $c = 0.00, 0.01, 0.02, 0.05, 0.08$, with averaging done over 10 plastic events for each case. r is the distance from the plastic center defined by a particle undergoing maximum displacement in a mode. (b)Dependence of length scale ($\xi_{\rm fit}$) extracted from fits to $e(r)$ (see text for discussion) with pinning concentration; also shown is the behaviour of $\xi_{\rm pin}$, extracted from pinning density, with c. 95

Contents

1 Introduction **11**

1.1 What are amorphous solids? 11

1.2 How are amorphous solids formed? 13

1.3 Potential Energy Landscape (PEL) 14

1.4 Mechanical properties 17

1.4.1 Shear deformation response of amorphous solids: a brief summary 18

1.5 Cavitation 23

1.5.1 Cavitation as a route to fracture 25

1.5.2 Relevant background literature on numerical simulations of cavitation 27

1.6 Organization of the thesis 28

2 Methods **31**

2.1 Models 32

2.1.1 2D Kob-Andersen model 32

2.1.2 The 3D Kob-Andersen (3dKABLJ) 33

2.1.3 3D Wahnstorm mixture (3dWahn) 34

2.1.4 2D Lancon et al model (2dLancon) 34

2.2 Molecular dynamics simulations to generate initial states 35

2.2.1 Solving the equations of motion 35

2.2.2 Thermostat 36

2.3 Energy Minimization 38

2.3.1 Conjugate gradient minimization 39

2.4 Hessian Matrices and diagonalisation 41

2.5 Boundary conditions 42

2.5.1 Minimum Image convention for a square box 42

2.5.2 Minimum image convention for a triclinic (sheared) box 43

3 Athermal quasistatic expansion: elasto-plastic phenomenology 47

3.1 Introduction 47

3.2 Objective 49

3.3 Model & Methods 49

3.3.1 Model 49

3.3.2 Preparation of initial state 50

3.3.3 Protocol 50

3.3.4 Calculation of Hessian matrix 50

3.4 Results 52

3.4.1 Yielding 52
3.4.2 Irreversible pressure-jumps 55
3.4.3 The Yielding avalanche 57
3.4.4 Statistics of avalanches 58
3.4.5 First plastic event & pre-yield plasticity 62
3.5 Summary 62

4 Cavitation instabilities under secondary cyclic shear deformations 65

4.1 Introduction 66
4.2 Objective 67
4.3 Model & Methods 67
4.3.1 Model 67
4.3.2 Initial state preparation 67
4.3.3 Protocol for mechanical deformations 67
4.3.4 Athermal Quasistatic cyclic shear (AQCS) 68
4.3.5 Coarse-grained density field and the phase diagram 69
4.3.6 Plasticity maps 70
4.4 Results 70
4.4.1 Early cavitation 70
4.4.2 Yielding, timescales & limit cycles 72
4.4.3 Spatial ramifications 75

4.5 Summary & Discussion 78

5 Effect of pinning on cavitation in amorphous solids 81

5.1 Introduction 82

5.2 Objective 83

5.3 Model & Methods 83

5.3.1 Model 83

5.3.2 Preparation of initial states 83

5.3.3 Deformation protocol 84

5.3.4 The pinning construction 84

5.3.5 Hessian of potential energy for systems with pinning 84

5.4 Results 85

5.4.1 Yielding and spatial ramifications 85

5.4.2 System-size effects 87

5.4.3 Irreversible plastic events on the potential energy landscape . . . 87

5.4.4 Spatial decay of plastic modes & a length scale of plasticity . . . 91

5.5 Summary & Discussion 96

6 Summary, Discussion & Outlook 99

1 Introduction

1.1 What are amorphous solids?

Based on the structural order, solids are broadly classified as crystalline, poly-crystalline or amorphous. The crystalline solids have a long-range structural order, the poly-crystalline solids have medium-range structural order whereas the amorphous solids lack long-range structural order(see Figure 1.1). Amorphous solids occur in diverse forms(see Figure 1.2), ranging from silicates & metallic glasses whose constituent particles are of few nanometers in size to granular solids whose constituent particles can go up to a few centimeters, thus spanning at least seven to eight orders of magnitude in sizes of constituent units.

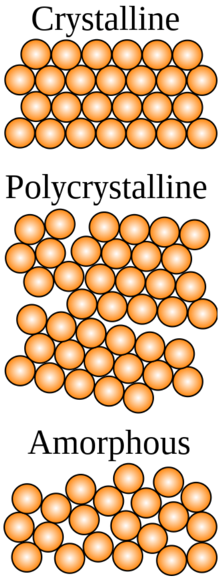

Figure 1.1. Schematic showing different types of structural order in solids; source: Ref [1]

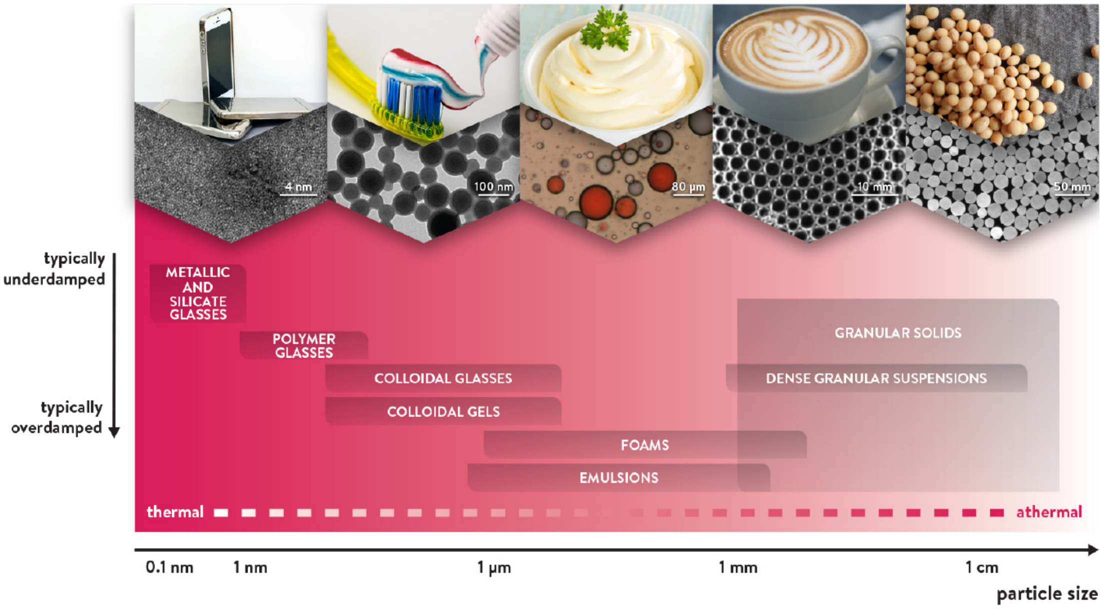
4 nm
100 nm
80 µm
10 mm
50 mm
typically underdamped
typically overdamped
METALLIC AND SILICATE GLASSES
POLYMER GLASSES
COLLOIDAL GLASSES
COLLOIDAL GELS
FOAMS
EMULSIONS
GRANULAR SOLIDS
DENSE GRANULAR SUSPENSIONS
thermal
athermal
0.1 nm
1 nm
1 µm
1 mm
1 cm
particle size

Figure 1.2. A figure from Ref [2] showing diverse amorphous solids. Their constituent particle sizes are shown on the X-axis and the Y-axis shows the dynamics of these solids.

These amorphous solids also show a great amount of variability in their properties, for example, they can be good conductors (eg. metallic glasses) or bad conductors (eg. silica-glasses) of electricity & heat, they can be soft-solids (eg: colloidal glasses) or hard-solids (eg: metallic glasses) etc. The soft-solids are typically ductile i.e. they break via necking and a large amount of plasticity where as the hard-solids are typically brittle i.e. they break suddenly and with minimal plasticity. As also shown in the Figure 1.2, depending upon the size of the constituent elements, these solids can be thermal or athermal. The solids whose constituent particles are larger are less influenced by thermal fluctuations (eg: granular solids) and vice-versa. Despite the diversity, they share many common features too. They typically undergo a glass transition upon cooling (exception: granular solids) the liquid phase leading to a disordered solid phase, such a transition is known as glass-transition. The variation of several observable properties share common-features on approach to this glass-transition upon cooling. Amorphous solids under mechanical loading beyond a threshold undergo a yielding transition which results in a transition from an elastic-solid-like phase to either a plastic flow or to material failure, depending on whether the solid is ductile or brittle. The plasticity in large variety of these solids upon mechanical loading shares many universal features.

1.2 How are amorphous solids formed?

When a high-temperature liquid is cooled to low enough-temperature, it either becomes a crystalline-solid via a first-order phase transition at the melting point T_m or turns into an amorphous solid around the glass-transition temperature T_g. Depending upon the liquid and the interactions among its constituents, it may or may-not form an amorphous solid. In most liquids, typically cooling the liquid fast-enough does result in formation of a glass-phase at $T_g < T_m$. The temperature of glass-transition is also known to depend on the cooling rate being used to make the glass [3]. As a liquid is cooled to the temperatures near T_g at an appropriate cooling rate (that avoids crystalization), as illustrated in the Figure 1.3(a) the enthalpy or the volume starts to fall continuously upto a point where it starts taking a turn. The point where it takes a turn is the glass-transition temperature for a given cooling rate as illustrated by two different cooling rate curves a & b in Figure 1.3(b). This behaviour is unlike the case of crystals where-in a sharp jump in enthalpy/volume signifies a first-order phase transition as shown in the Figure 1.3(b). On cooling the liquid towards the T_g, the relaxation times start to increase [4]. Depending upon the type of glass-forming system, the temperature dependence of the relaxation time can be different as shown in Figure1.3(b). For a class of glasses usually referred as strong glasses, the temperature dependence of the relaxation time is given by a Arrhenius law [5]:

$$\tau \sim \exp\left(\frac{E}{k_B T}\right) \tag{1.2.1}$$

E denotes the effective activation energy. For an another class of glasses like fragile-glasses, the temperature dependence of the relaxation time is still a matter of debate. The most widely used fit used to describe the timescales in fragile glasses is given by Vogel-

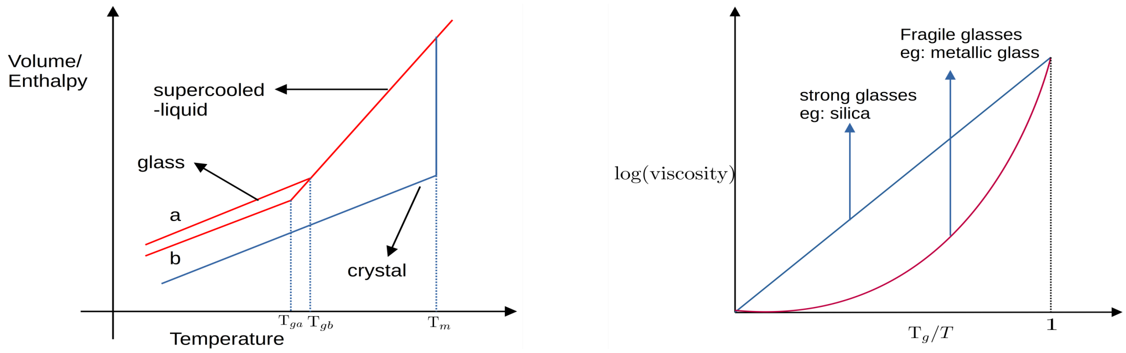

Figure 1.3. Left: Dependence of the enthalpy/volume upon temperature for crystalline and glass-forming systems [6]. Right: Dependence of relaxation timescales on temperature for different glass-forming systems [5].

Fulcher-Tamman (VFT) law:

$$\tau \sim \exp\left(\frac{D T_0}{T - T_0}\right) \tag{1.2.2}$$

T_0 here denotes the temperature at which the relaxation time diverges. The classification of glasses as strong and fragile has nothing to do with their mechanical strengths, it is just an unfortunate misnomer. The classification of amorphou solids into strong & fragile is mutually exhaustive. Due to the rapid increase in the relaxation timescales on approach to T_g, the glass-forming systems typically fall out of thermal equilibrium. And on further cooling, one just ends up tracing a branch on the Volume vs Temperature depending upon the cooling rate. The slower the cooling rate, the lower the branch. In the Figure1.3(a), the branch b is obtained by a slower cooling rate than the branch a. The cooling rate used to form an amorphous solid determines many material properties like the thermal conductivity, elastic modulii etc. The cooling of the glass-forming system below T_g results in solidification. And due to the divergence of the relaxation time-scales, the resulting amorphous solid always remains in a non-equilibrium state.

1.3 Potential Energy Landscape (PEL)

Potential energy of a material system is a multi-dimensional function that assigns a value of potential energy to a given microscopic configuration of a system. The potential energy landscape [7] refers to this energy surface that depends on its microscopic parameters. For a system of N particles in d dimensions interacting via a potential energy that depends only on the co-ordinates (and not on any of its derivatives), the potential energy is a function of $d * N$ particle co-ordinates.

$$U = U(\{x_i^\alpha\})$$

The index i runs from 1 to N and α denotes the spatial directions. A single point on the PEL thus represents a unique configuration of particles. The PEL of amorphous solids are known to contain a large number of local-minimas at different energy levels known as inherent structures / inherent states. These inherent structures stem from the large degree of frustration in the interparticle-interactions. Due to the large number of possible inherent-states, a large number of possible amorphous configurations can exist for a given system and hence the potential-energy-landscape of amorphous solids is very rugged as shown in the schematic Figure 1.4 . The amorphous solids corresponding to lower-energy states on the PEL are more stable and accessible only at lower temperature. As one would expect, the local-minimas corresponding to amorphous states are at a higher-energy than the crystalline/ordered state minimas. The lowest energy amorphous state is termed as “ideal glass". The shape of the neighbouring PEL where the system is residing is expected to significantly influence the structure and dynamics of amorphous systems. And thus, for understanding the properties of amorphous solids, potential energy landscape (PEL) has proven to be of great use. Significant progress in understanding wide-range of properties [9–11] of amorphous systems ranging from its slow-dynamics on approach to T_g [7, 12], caging-behaviour [13, 14], local-structure [15], thermodynamics [9, 16], mechanical properties [17–19], transport properties [9], rheology [20] etc. from a PEL picture has been made in last few decades and is still a domain of active research.

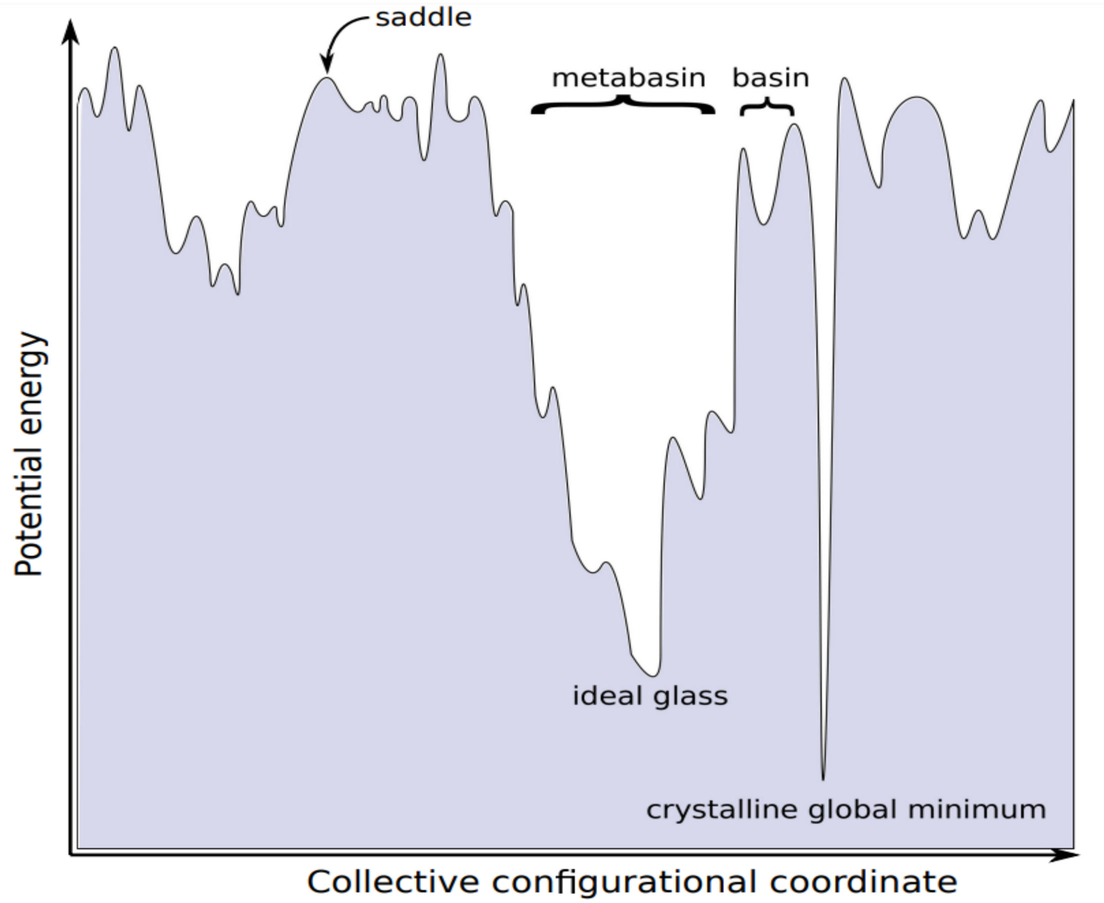
saddle
metabasin
basin
Potential energy
ideal glass
crystalline global minimum
Collective configurational coordinate

Figure 1.4. A schematic of a patch of potential energy landscape of amorphous solids from Ref [8]

1.4 Mechanical properties

The mechanical failure of amorphous solids is an important area of research because these materials are widely used in various technological applications, ranging from structural materials to electronic and optical devices. Understanding the mechanical properties and failure mechanisms of amorphous solids can help to improve the design and performance of these materials, and enable the development of new materials with enhanced properties. One of the key challenges in studying the mechanical failure of amorphous solids is the absence of a well-defined crystal structure. In crystalline materials, a regular and predictable microscopic structure naturally leads to a well-defined notion of structural defects. The defects are simply the sites which deviate locally from the global crystalline-structure. The plasticity unsurprisingly originates around these microscopic structural defects [21]. In amorphous solids due to their disordered microscopic structure, a trivial reference state does not exist as there is no clear notion of a perfect amorphous solid unlike that of a perfect crystal. Thus defining a notion of structural defects become a very challenging task. And therefore, where the plasticity stems from at a microscopic level, becomes extremely difficult to understand. Due to the lack of a amorphous reference structure, the mechanical response of amorphous solids also exhibits a strong coupling between plasticity and elasticity [22] leading to effects like strain-softening making the mechanical response highly non-linear. The lack of a reference structure in amorphous solids also makes problems like shear-banding & constant-load-response (creep) extremely complicated. In solids with structural order, the phenomena like shear banding and creep response can be understood using the notion of defects [23, 24]. But such descriptions are difficult to construct for amorphous solids without significant structural information. The mechanical response of amorphous solids also varies drastically with heterogeneity of the sample in consideration [25]. The heterogeneity in these solids is usually a result of the preparation protocol and since these are non-equilibrium solids, they retain the memory of their preparation protocols. And this heterogeneity plays a significant role in determining many aspects of mechanical response. Understanding the mechanical-response of amorphous solids is thus a very complex & challenging endeavour.

1.4.1 Shear deformation response of amorphous solids: a brief summary

In the studies of mechanical deformation of amorphous solids, a large part of the literature is devoted to understanding the plasticity in amorphous solids under shear deformation. The shear-deformation of amorphous solids has been studied using theories like Shear Transformation Zoneb (STZ) theory [26], meso-scale elasto-plastic models [27], particle-based numerical simulations [28] & of course-experiments. One of the most widely studied models of plasticity under shear is the shear-transformation-zone (STZ), it describes the plasticity under shear via localised rearrangements that occur within a STZ. A large part of the phenomenology of shear-response of amorphous solids like yielding of the solid, shear-banding, avalanches etc. is explained using this theory [29, 30]. The meso-scale elasto-plastic models aim at describing the shear-response of amorphous solids at a coarse-grained meso-scale where the plasticity occurs via stress-exchange between meso-scaled elements. These models have been successful at reproducing a large array of phenomenology of amorphous solids [27]. The particle-based microscopic models involve studying the amorphous solids as composed of particles interacting via pair-wise interactions [17, 28]. The dynamics of the particles is updated using moolecular-dynamics-like schemes. These models too, reproduce a wide-range of phenomenology of amorphous solids and have been widely used to push the boundaries of our understanding of mechanical deformation of amorphous solids at times by discovering novel phenomena. The studies of mechanical deformation of amorphous solids using numerical simulations is the main focus of this thesis and will be main discussed in detail in the next sections.

1.4.1.1 Athermal quasistatic shear (AQS): Phenomenology in numerical simulations

Protocol

In particle-based numerical simulations, one of the most widely-used techniques to study shear-response of amorphous solids is the athermal quasistatic shear (AQS) [17, 28]. The shear response of the solids can also be studied in presence of a finite driving strain rate $\dot{\gamma} \neq 0$ and in presence of thermal fluctuations $T \neq 0$. Many of the amorphous solids, are well below their glass-transition temperature T_g at room temperature. Thus, to simplify the studies, one takes the limit $T \to 0$ for AQS studies. The plasticity of the solids under shear is easier to breakdown under quasistatic-loading where in $\dot{\gamma} \to 0$. Thus in athermal quasistatic loading, one takes the limits, temperature $T \to 0$ and $\dot{\gamma} \to 0$. Under such a protocol, the plasticity occurs directly on the potential energy landscape and the shear-response can be studied as a purely-mechanical phenomena. Despite the absence of finite-strain rates and the absence of thermal fluctuations, this protocol captures the essential features of deformation when $T < T_g$ [31]. In each step of the AQS protocol (see Figure 1.5), one typically applies a constant increment of the shear strain $\delta\gamma$, which is achieved by changing setting an appropriate tilt value of the box using the relation, $\gamma = (\varDelta L)/L$ along with re-scaling the coordinates of the particles in the simulation box such that, $x' = x + \delta\gamma\, y$. The change in the coordinates of the particles in simulation box results in unbalanced forces, so to reach mechanical equilibrium, one turns on a energy-minimization dynamics using algorithms like steepest descent, conjugate gradient, FIRE etc. This ensures the limit $T \to 0$ and $\dot{\gamma} \to 0$ by taking the system to the nearest local-minimum on the potential-energy-landscape (PEL).

Stress-strain curves

As evident from the Figure 1.5, under AQS, small values of strains, the amorphous solids

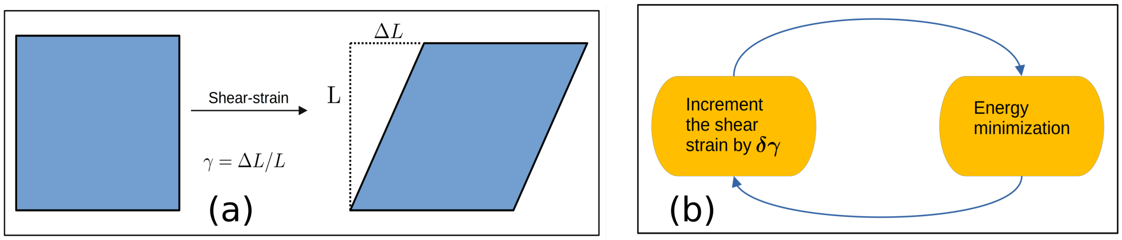

Figure 1.5. (a) A schematic of shear deformation on the simiulation box (b) Algorithm of the AQS protocol.

exhibit elastic response where-in the stress is proportional to the strain i.e. $\sigma_{xy} \propto \gamma$. But even in the elastic branches of the stress-strain curve, the response of amorphous solids is not strictly elastic due to presence of non-zero non-affine displacements [22,32]. Upon further loading, significant plasticity accompanied by stress-drops starts to occur, the size of the stress-drops corresponding to plastic events also starts to increase. On increasing the strain further, the stress saturates around a mean value and the solid is considered as yielded. The saturation of the stress around a mean value highlights the presence of a post-yield steady state. Microscopically, the plasticity of any kind occurs via irreversible rearrangement of particles within a shear-transformation-zone [26]. The irreversible particle rearrangements within an STZ creates a quadrupolar displacement field (see Figure 1.6(b)) between two successive steps of athermal quasistatic shear [33]. The successive triggering of these STZs within one step of AQS, leads to avalanches of plasticity [28,34] which are seen as large stress drops in the schematic Figure 1.6. [22,32]. Depending upon the model of solid and its preparation history, the yielding transition either corresponds to fluidisation via plastic flow or to a mechanical failure [25].

Plasticity on the potential energy landscape

The occurrence of plasticity can be tracked on the potential energy landscape via the derivatives of potential-energy for a given particle configuration. Since the system resides in an energy minimum, the first derivative of potential energy which is the force, $\frac{\partial U}{\partial x^i_{alpha}} \rightarrow$

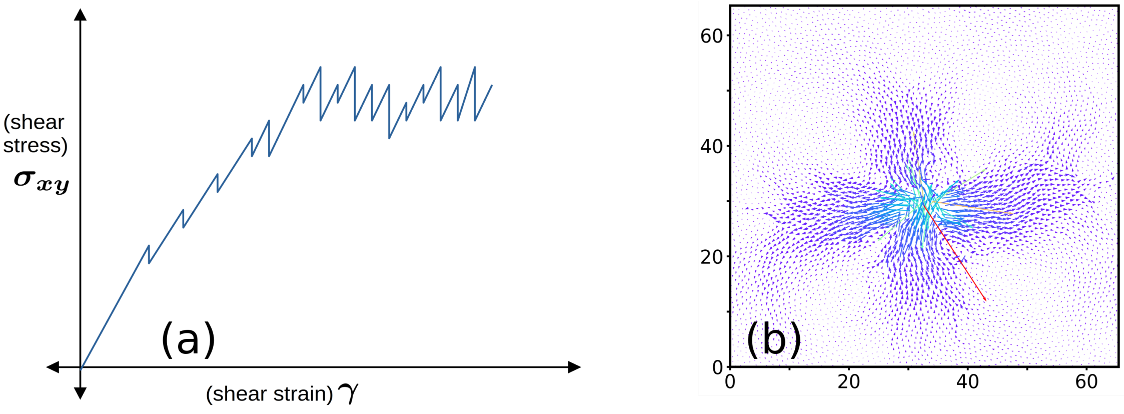

Figure 1.6. (a) A typical stress-strain curve seen under AQS. (b) A quadrupolar displacement field corresponding to irreversible particle rearrangements in AQS.

0. The crucial information is contained in the second derivative of the potential energy which indicates the curvature of different possible directions around a minimum. The matrix of second-derivatives of the potential energy also known as the Hessian is given by, $\mathcal{H} = \frac{\partial^2 U}{\partial x^i_\alpha \partial x^j_\beta}$, where the Latin indices $i, \& \ j$ represent the particle numbers and the Greek-indices $\alpha \,\&\, \beta$ represent the spatial directions $x, y \,\&\, z$. In seminal works [17, 28, 34], it was shown that on approach to a point of plasticity under shear, only the lowest non-zero eigenvalue λ_{min} of the Hessian vanishes as $\lambda_{min} \sim \sqrt{\gamma_c - \gamma}$ suggesting that the plasticity occurs only a saddle-node bifurcation on the potential energy landscape. In a saddle-node bifurcation, the local-minimum where the system resides on the potential energy landscape, becomes unstable in one direction and the system falls off to a lower energy minimum as illustrated in Figure 1.7. This saddle-node bifurcation is connected to the vanishing of elastic constants [35] & these relations can aid in predicting the value of strain at which plasticity occurs [36] and in estimating the energy barriers in vicinity of a plastic event [37]. Due to the vanishing of only one eigenvalue near a plastic event, the eigenmode of λ_{min} is known to predict the displacement fields on approach to the plastic events [28].

Avalanche-size distributions

The plasticity in AQS is known to occur via avalanches, where-in multiple irreversible particle rearrangements take place. Tracing the origin of these particle rearrangements is

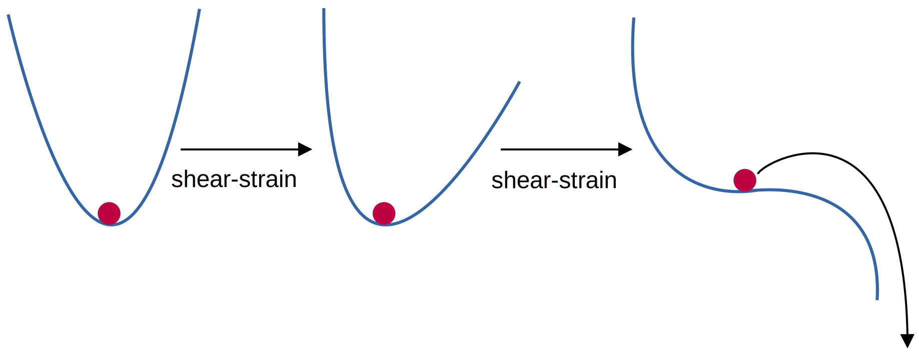

Figure 1.7. A schematic of a sadlle-node bifurcation.

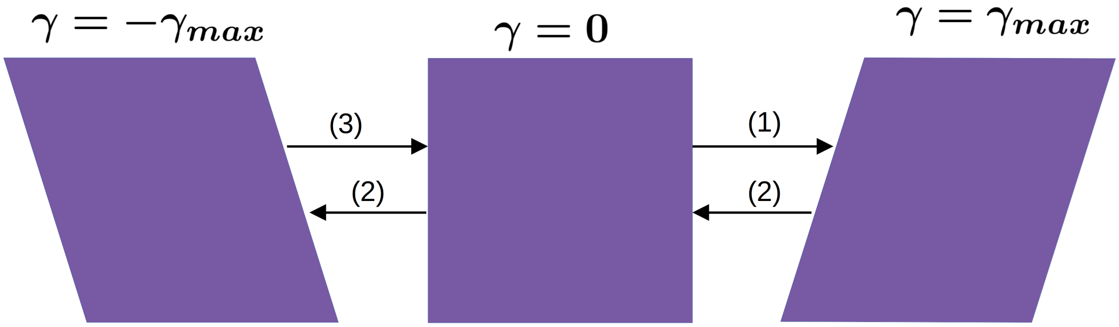

Figure 1.8. A schematic illustrating the protocol of cyclic shear.

a challenging task. The sizes of plastic events in the pre-yield and post-yield phase of the sheared solids have been studied extensively [37, 38] as these are generally accessible in acoustic experiments of mechanical loading. In the pre-yield part, the distribution of the sizes of first plastic-events is Weibullian [37] and the means of the average stress drops scale as $\langle \Delta\sigma \rangle \approx N^{\eta}$ with $\eta \approx 0.62$, thus showing sub-extensive system-size scaling. And the energy drops in the pre-yield were found to be independent of the system-size. Similarly for the post-yield, steady state avalanches, the mean stress-drops scale with the system size as $\langle \Delta\sigma \rangle \approx N^{\alpha}$ with $\alpha = 1/3$ and the mean energy-drops scale with the system size as $\langle \Delta U \rangle \approx N^{\beta}$ with $\beta = 2/3$. All the exponents *viz.* $\alpha, \beta \,\&\, \eta$ are same in both 2D and 3D. The system-size scaling of the mean size of the avalanches suggest that the plasticity is scale-free. The sizes of avalanches under other protocols of driving which involve finite strain rates is known to be different [39, 40].

1.4.1.2 Amorphous solids under cyclic-shear

Apart from the unidirectional shear, response of amorphous solids under cyclic-shear has been studied to a great extent [41–45]. In a cycle of cyclic-shear (see the schematic Figure 1.8), (i) The amorphous solid is subjected to a shear-strain upto a $\gamma = \gamma_{max}$ (ii) this is followed up by a reversal in the direction of strain upto $\gamma = -\gamma_{max}$ (iii) lastly, another reversal in the direction of shear upto a strain $\gamma = 0$. The cyclic-shear deformation can be studied in the athermal quasistatic limit or at a finite deformation rate. But here we restrict our attention to the athermal quasistatic studies. As under the cyclic shear, an amorphous solid is again loaded back to the zero-strain, the solid can exhibit rich phenomenology depending upon the amplitude of cyclic shear γ_{max} and on the annealing of the initial state. On driving the amorphous solid at an amplitude $\gamma_{max} > \gamma_{yield}$, here too, the solid yields. As shown in the Figure 1.9, for poorly annealed solids, the steady-state energies of the solid under cyclic shear decrease with increasing the driving amplitudeγ_{max}, this corresponds to mechanical-annealing. On increasing γ_{max} further, a cusp appears at $\gamma_{max} = \gamma_{yield}$. Where as for well-annealed glasses, the mechanical annealing is absent and a sharp-jump occurs at $\gamma_{max} = \gamma_{yield}$ is seen. Apart from the yielding under cyclic shear, the amorphous solids show multiple effects like memory of loading [46], relaxation to non-trivial steady-states via limit-cycles [42], fatigue-failure [47] etc. upon cyclic-shear loading.

1.5 Cavitation

Cavitation refers to formation of voids in a material. The necessary basic ingredient for cavitation to occur is the presence of attractive interactions among the constitutive elements. Thus cavitation can occur in wide range of materials like ductile metals [48], liquids [49], different types of amorphous solids etc., but here we restrict our attention to cavitation in amorphous solids. In amorphous solids, cavitation is known to occur in a variety of solids including soft solids like gels [50], wet-granular materials, disordered

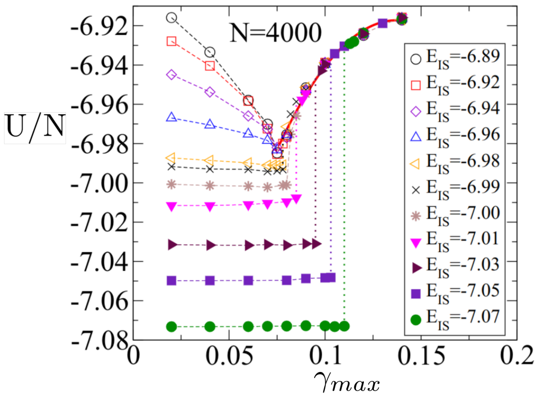

Figure 1.9. Image taken from Ref [44]. Effect of different level of annealing on the cyclic shear response of a model amorphous solid.

biological-tissues [51–53], emulsions etc. and hard-solids like metallic glasses [54–58], polymeric glasses [59, 60], silicate glasses [61, 62] etc. Due to the widespread occurrence of these materials in various contexts ranging from nano-metric scales to geological scales, the phenomena of cavitation becomes extremely important to study. In amorphous solids, cavitation can occur due to an interplay of variety of factors, such as the presence of impurities or defects in the material [63], the presence of shear bands [64–66], or the accumulation of strain [67, 68]. Cavitation can have significant effects on the failure behavior of these materials. Once cavitation occurs, the voids can reduce the material's local density and thus the mechanical strength. These cavitated sites in a solid can also act as nucleation sites for shear bands or for plasticity as stress accumulates around a free-surface of the cavity [69]. Understanding the dynamics of cavitation in amorphous solids is therefore critical for predicting and controlling their failure behavior. By studying the mechanisms that govern cavitation and its effects on material properties, one can develop new models and simulation tools for predicting the behavior of amorphous solids under different loading conditions, and for designing new materials with enhanced mechanical properties and resistance to failure.

1.5.1 Cavitation as a route to fracture

In the failure of many different types of amorphous solids, the fracture is known to occur via small voids in the solid. In numerous experiments of fracture of amorphous solids, it has been observed that upon mechanical loading, the fracture occurs via coalescence of voids [62, 70–72]. These voids are much smaller in size than the crack, for example, in metallic glasses, the sizes of these voids are of the order of a few nanometers. Under tensile loading, a material fracture that occurs via necking and deformation of the surroundings is termed as ductile where as a fracture that occurs without necking and propagates quickly through the solid is termed as brittle fracture [73]. The fracture that occurs via cavitation lies between these two regimes and as a result is sometimes termed as 'quasi-brittle' [67, 74] and these cavitation instabilities are seen as 'ductilities' within a brittle material. This quasi-brittle fracture via cavitation has been observed in wide-range of amorphous solids, even in the solids that are believed to be brittle. Thus, making a strong case for a detailed understanding of these instabilities.

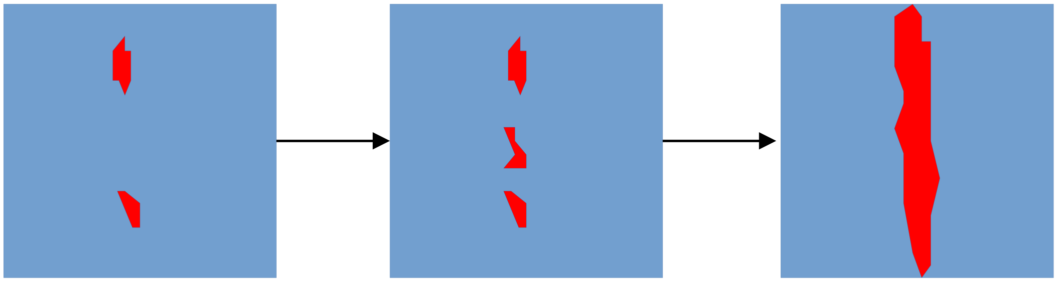

Figure 1.10. A schematic of an amorphous solids undergoing fracture via coalesence of cavities as reported in multiple experimental studies.

1.5.1.1 Thermodynamic origin of cavitation

The mechanical interpretation of cavitation instabilities is focused on stress, strain and fracture of the solids. But from a thermodynamic point of view, these cavitation instabilities can be understood as a solid-gas phase separation. As shown in the schematic of a phase diagram of an attractive glass-forming system in temperature-density plane

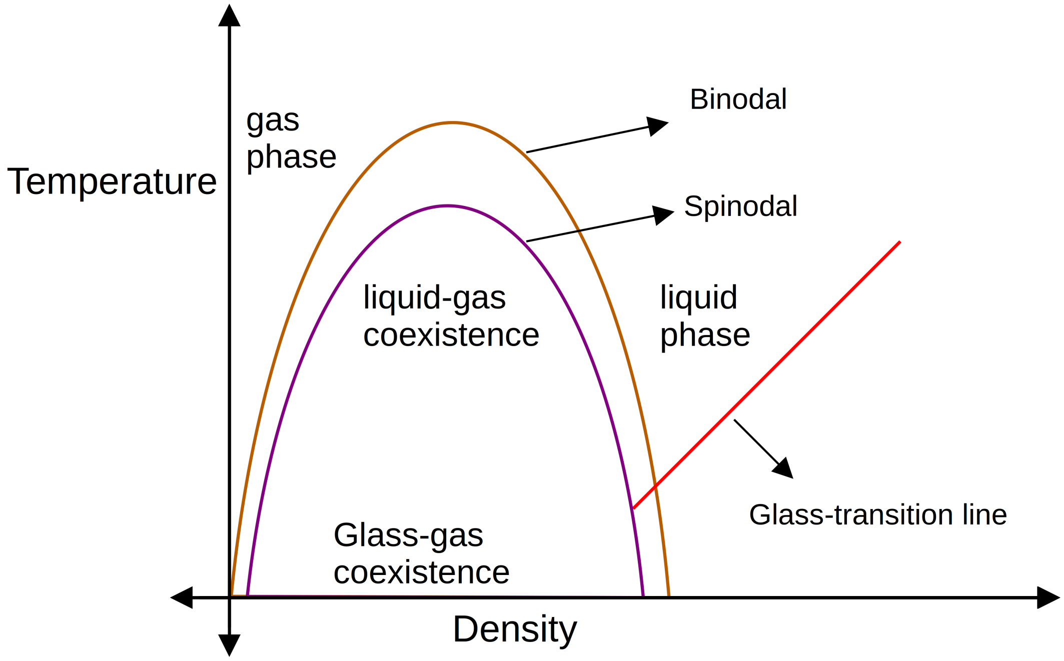

Figure 1.11. A schematic phase diagram of an attractive glass-forming system in the (temperature)$T - \rho$(density) plane.

(pressure is allowed to vary freely here) in Figure 1.11, there exist distinct liquid and gas phases at very low and very high values of densities respectively, this is made possible only due to presence of attractive interactions. For the intermediate values of densities and appropriate values of temperatures, there exists a phase-coexistence region marked by a binodal line. The binodal line marks the onset of phase separation into liquid and gas components via nucleation as the primary mechanism. In the interiors of the binodal line, there exists a spinodal line, which when crossed, results in homogeneous and spontaneous phase separation of liquid and gas components. At higher densities of the liquid phase, there exists a glass-transition line below which the liquid solidifies into a glass. In a seminal work by Sastry [75], it was shown that, the glass-transition line cuts the spinodal at finite temperatures which gives rise to a separate glass-gas coexistence in glass-forming systems where a solid would grow voids in it (manifestation of the gas phase). The manifestation of gas-glass coexistence region results in cavitation instabilities in amorphous solids.

1.5.2 Relevant background literature on numerical simulations of cavitation

There have been a large number of studies that observe cavitation in numerical simulations using specific material-models [76–81]. Here we briefly review the literature relevant to the work discussed in later chapters of this thesis.

Bouchbinder et al [82, 83], in their works have have developed a framework for the problem of circular cavity in an amorphous solids using the STZ (shear transformation zone) [26] theory. They found that these circular cavities are stable to small perturbations. They found existence of fast-cavitation modes that lead to dynamic failure. In numerical simulations, a study by Guan et al [67] showed how cavities with small radii and high curvatures have significantly lower surface energies thus making them abundant in fracture studies of amorphous solids. On short timescales, they find agreement of the cavitation rates with a modified classical nucleation theory (CNT) that accounts for the plastic-flow and curvature dependent surface energy of cavities, where as on longer time-scales, due to strain aging, CNT doesn't agree. Another study by Chaudhuri and Horbach [68], using numerical simulations, expanded the amorphous solid uniformly into the phase-coexistence region (below T_g). The solid caviates upon expansion and the density of the bulk-phase remains constant even upon expansion as one would expect. They observe long-lived cavitated states within the frozen glass. Upon unloading the solid to the starting values of density ρ, they found Bauschinger-effect [84] like hysteresis curves. The first work by Altabet et al [85], in numerical simulations, studied the inherent states of finite temperature states around the liquid-gas coexistence and the response of a quenched liquid to athermal quasistatic expansion. They demonstrate signatures of a first-order yielding like-cavitation on the energy-landscape and found that the locus of cavitation transition on the energy-landscape doesn't change much with the temperature. In their second work, Altabet et al [86] looked at the effect of different inter-particle attractive potentials and their effect on the cavitation transition. They found that the attractive potentials with very short range attractions show an absence of the first order transition where as longer-ranged attractive systems show a first-order-like cavitation transition. In the works by Karmakar et al. [73] and Paul et al. [87], the tensile failure of an amorphous solid under grip boundary conditions has been studied. The work by Karmakar et al. [73], found an existence of a ductile-to-brittle transition by just varying the attractive part of the Lennard-Jones like pairwise potential. They found existence of cavitation ahead of the crack tip in many occasions as reported in many experiments of crack propagation. In the work of Paul et al. [87], on varying the aspect-ratio of loading geometries, they found a crossover from necking dominated ductile failure to cavitation dominated failure.

Despite these advances on understanding cavitation in amorphous solids, the fundamental questions around cavitation are still unaddressed. In studies of mechanical deformation of amorphous solids, the focus has revolved around plasticity under shear deformation. Under shear deformation, numerical simulations have explored, the origin of plasticity on the energy landscape, statistics of avalanche sizes, possible ways to predict plasticity in these solids, role of annealing of the solid etc. These insights have led to development of meso-scale elasto-plastic models which have shed significant light on understanding plasticity under shear in these solids. But due to the focus on phenomena of plasticity under shear, these studies do not account for phenomena like cavitation instabilities that usually arise under tensile deformations of the solid. Here, we attempt to bridge the gap.

1.6 Organization of the thesis

As we have discussed the necessary background for the thesis in this chapter, we detail out some important methods and models that have been used in the studies in Chapter 2. To understand the cavitation instabilities in amorphous solids, we have explored three directions as summarised in Figure 1.12.

In Chapter 3, we drive an amorphous solid into this region via athermal quasistatic expansion, as the cavitation instabilties originate from gas-glass coexistence. With an aim to compare plasticity due to cavitation with the well-studied plasticity under shear, we first study the stability of the solid near occurrence of cavitation instabilities to check for scaling laws observed in the case of plasticity in amorphous solids under shear, followed by measurement of the avalanche-size distributions and its system-size scaling. We highlight multiple universal features of amorphous palsticity and the important differences between the plasticity due to cavitation and plasticity under shear.

In Chapter 4, we study the possibility of cross coupling between cyclic-shear and uniform expansion, as multiple similarities exist between plasticity due to shear and plasticity due to cavitation, leading to cavitation. We explore this direction via imposing a secondary deformation in the form of cyclic-shear on the spatially-homogenous states generated via athermal quasistatic expansion. We systematically explore the two-parameter-space of amplitude of cyclic shear and the density of the expanded state and mark a region where cross-couplings lead to cavitation at lower energy thresholds. Starting from a same-expansion trajectory, we look at the location of soft-spot that cavitates and the spatial-structure of the events that lead to cavitation under cyclic-shear. Our work thus sheds light on cross-couplings between different deformation modes that could lead to early onset of failiure in amorphous solids.

In Chapter 5, we explore the idea of micro-alloying the amorphous solid with foreign particles to increase its material strength which has gained significant popularity in recent years. In this context, we study the response of an amorphous solid with fraction of its particles pinned, to athermal quasistatic expansion. A pinned solid constitutes a minimal model of a micro-alloyed amorphous solid. Under expansion, we monitor the changes in its elasto-plastic response and the related finite-size effects due to particle pinning. We also probe the stability near cavitation events using the appropriate Hessian matrix. We

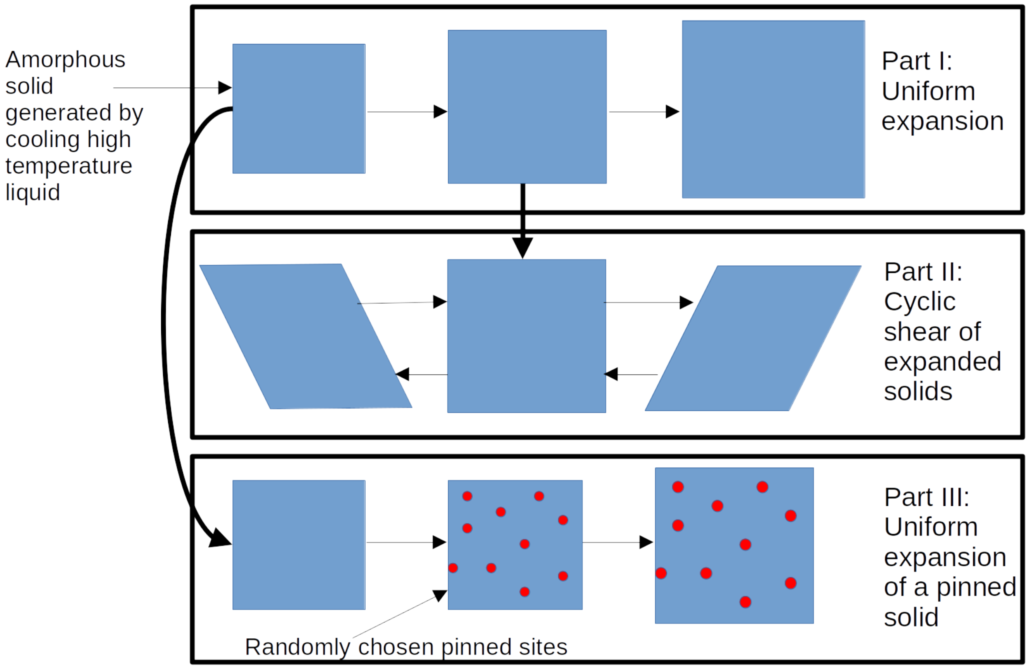
Amorphous solid generated by cooling high temperature liquid
Part I: Uniform expansion
Part II: Cyclic shear of expanded solids
Part III: Uniform expansion of a pinned solid
Randomly chosen pinned sites

Figure 1.12. A schematic summarising the directions that we explore in this thesis

also calculate the spatial-decay profile of the plastic modes leading to cavitation in pinned solids to highlight an important charactersitic of these pinned solids. Which explains its elasto-palstic response.

2 Methods

In this chapter we briefly review the numerical methods used in the later chapters of this thesis. We start by describing the particle-based models used to carry out the numerical simulations followed by the numerical schemes to carry out the particle based simulations and lastly discuss the method used to analyse the data from the simulations

To study cavitation instabilities, we use particle-based numerical simulations. In such simulations, an amorphous system is modeled a mixture of particles interacting via pairwise potentials. These simulations successfully reproduce the phenomenology of amorphous systems ranging from behaviour near the glass-transition to deformation response of amorphous solids [5, 28, 88, 89]. The particle based simulations have also aided the development of various theoretical descriptions of amorphous systems [26, 90–92]. The major advantage of these particle-based numerical simulations is the access to the microscopic particle-level data. Such data is mostly inaccessible in experiments for most amorphous systems, except for amorphous systems like colloidal glasses or dense suspensions whose constituent particles are sufficiently large. But even for those experimental systems, tracking the motion of a large number of particles is difficult. Particle based-simulations lack this limitation and as a result they provide a useful way of extracting the microscopic phenomenology of amorphous materials. Apart from the advantages of particle-based simulations, there are several limitations in these studies too. These simulations are computationally expensive and running the simulations that correspond to experimentally-accessible timescales, is difficult. Recent development of algorithms like SWAP monte-carlo [93, 94] have made significant progress on this but the dynamics accessible by these algorithms is still barely of the order of few milliseconds on experimental timescales [95]. Despite the limitations, they have been extremely useful in gaining micro-scopic insights into these systems.

The models we use in our studies, necessarily have attractive interactions between the constituent particles as opposed to the purely-repulsive models studied in the literature. This is because the stable cavities in the solid (main focus of the thesis) cannot occur without attractive interactions (discussed in Introduction). These models are described in 2.1. To update the dynamics of these model systems at finite temperatures, we use molecular dynamics in the NVT-ensemble as discussed in 2.2. For simulations of mechanical deformation in the athermal quasistatic limit, we use the conjugate gradient energy minimization method which is described in 2.3. The boundary conditions used in our studies are discussed in 2.5.

2.1 Models

2.1.1 2D Kob-Andersen model

The common numerical model that we use across all three studies is the well-characterized two-dimensional model binary Lennard-Jones mixture (2DMKA), Kob-Anderson model [96, 97] which has $65 : 35$ composition of the two species, A and B, with interaction parameters $\sigma_{AA} = 1.0$, $\sigma_{BB} = 0.88$, $\sigma_{AB} = 0.8$, $\epsilon_{AA} = 1.0$, $\epsilon_{BB} = 0.5$, $\epsilon_{AB} = 1.5$. Thus σ_{AA} and ϵ_{AA} set the units of physical quantities for this model. The glass transition temperature for this model is $T_g = 0.33$. The parameters of this model are derived from a 3D metallic glass-model for the metallic glass-alloy $Ni_{80} - P_{20}$. The composition $65 : 35$ is a better glass-former in two-dimensions than the $80 : 20$ one [97]. Since our work requires us to calculate the second-derivatives of the potential energy, we smoothen the Lennard-Jones potential up to first two derivatives by adding a bi-quadratic polynomial. This doesn't change anything qualitatively. The interaction potential between particles i and j take the following form:

$$V_{mn}(r_{ij}) = 4\epsilon_{mn}\left[\left(\frac{\sigma_{mn}}{r_{ij}}\right)^{12} - \left(\frac{\sigma_{mn}}{r_{ij}}\right)^{6}\right] + u(r_{ij}) \tag{2.1.1}$$

where,

$$u(r_{ij}) = C_0 + C_2\left(\frac{r_{ij}}{\sigma_{mn}}\right)^2 + C_4\left(\frac{r_{ij}}{\sigma_{mn}}\right)^4$$

Here, m and n would correspond to either of the labels A or B which signify the type of particles. The constants C_0, C_2 and C_4 are determined by requiring the potential and its first two derivatives to be zero at the cutoff $r_c = 2.5\sigma_{mn}$. The simulations are performed on variety of system sizes ranging from $N = 10^3$ to $N = 10^5$ particles, with periodic boundary conditions.

To probe the universality of square-root singularity for cavitation instabilities across diverse model amorphous systems, we have also studied a few other glass-forming models in $d = 2$ & $d = 3$. These models include:

2.1.2 The 3D Kob-Andersen (3dKABLJ)

This is a 3D model that was proposed to mimic a metallic glass Nickel-Phosphorous $Ni_{80} - P_{20}$ and has been studied extensively in the literature. It is a binary mixture with particles interacting via Lennard-Jones potential of the the form as described in equation 2.1.1. The two species A & B are present in a ratio of 80 : 20 [96] and the interaction parameters are $\sigma_{AA} = 1.0$, $\sigma_{BB} = 0.88$, $\sigma_{AB} = 0.8$, $\epsilon_{AA} = 1.0$, $\epsilon_{BB} = 0.5$, $\epsilon_{AB} = 1.5$. Here too the units are set by ϵ_{AA} and σ_{AA}. The interactions are cut-off at a distance $r_{\alpha\beta} = 2.5\sigma_{\alpha\beta}$, where α & β can be either A or B. The glass-transition temperature of this model is

$T_g \approx 0.46$. For our study, we first equilibrate the system at a high-temperature $T = 3.0$. The high-temperature liquid is quenched to $T = 0$ via conjugate gradient energy minimization to obtain initial states for our study of mechanical deformation.

2.1.3 3D Wahnstorm mixture (3dWahn)

It is a 50:50 binary mixture of two species A & B interacting via Lennard-Jones potential that mimicks binary alloys [98, 99] with parameters that optimise the glass-forming ability, $\epsilon_{AA} = \epsilon_{BB} = \epsilon_{AB} = \sigma_{AA} = 1.0$, $\sigma_{AB} = 1.1$ & $\sigma_{BB} = 1.2$. The interactions are cut-off at $_{\alpha\beta} = 2.5\sigma_{\alpha\beta}$ where α & β can be either A or B. . Here too the units are set by ϵ_{AA} and σ_{AA}. We add a smoothing term of the form in equation2.1.1 to smoothen out the potential energy at the cut-off of interactions. The initial states, here too were prepared by quenching high-temperature liquid at $T = 3.0$ to $T = 0.0$ via conjugate gradient energy minimization.

2.1.4 2D Lancon et al model (2dLancon)

It is another binary mixture in two-dimensions that was originally proposed as a model for a quasicrystal system [100, 101] with the composition $N_A/N_B = (1 + \sqrt{5})/4$. The particles here too interact via Lennard-Jones potential with parameters, $\sigma_{AA} = 2\ \sin(\pi/5)$, $\sigma_{BB} = 2\ \sin(\pi/10)$, $\sigma_{AB} = 1.0$, $\epsilon_{AA} = \epsilon_{BB} = 0.5$ and $\epsilon_{AB} = 1.0$. The interactions are cut-off at $r_{\alpha\beta} = 2.5\sigma_{\alpha\beta}$ where α & β can be either A or B. Here too we add smoothing terms to the Lennard-Jones potential as shown in the equation2.1.1.The initial states, here too were prepared by quenching high-temperature liquid at $T = 3.0$ to $T = 0.0$ via conjugate gradient energy minimization.

2.2 Molecular dynamics simulations to generate initial states

2.2.1 Solving the equations of motion

To generate states for our studies on mechanical deformation in the athermal limit, we sample inherent structures of the model system that we consider. The inherent structures are obtained from the liquid states of the model. For this purpose, we equilibrate the glass-forming system at the temperature $T = 1.0$, which is done using the molecular dynamics simulations.

In the molecular dynamics simulations, the motion of the particles is evolved using Newton's equations of motion, to obtain a sequence of microstates corresponding to the model. For a system of N particles, the set of $d \cdot N$ positions (d: spatial dimension) i.e $\{x_i^\alpha\}$ are evolved using the equation of motions, where the index α represents the spatial directions and i is the particle index. The equations of motion are given by:

$$m \frac{d^2 x_i^\alpha(t)}{dt^2} = \sum_{\langle j \rangle} f_{ij}^\alpha \tag{2.2.1}$$

The term $\sum_{\langle j \rangle} f_j^\alpha$ is the sum of all the forces on i^{th} particle due to its neighbours $\{j\}$. The forces are typically short-ranged and hence the calculation of forces only involves summing the forces due to neighbours $\langle j \rangle$. The forces on i^{th} particle due to j^{th} particle, i.e. f_{ij}^α are conservative and derived from a pair-wise potential like the one shown in equation (2.1.1). Thus

$$f_{ij}^\alpha = -\frac{\partial V_{ij}(r_{ij})}{\partial x_i^\alpha}$$

The summing of forces due to neighbours $\sum_{\langle j \rangle} f_j^\alpha$ is carried out using the schemes-like cell-lists or neighbour-lists.

The x_i^α are evolved via integrating/solving the differential equations(2.2.1). The integration of the equation of motion to update the particle positions is carried out using the velocity-verlet integration scheme. In the velocity-verlet integration scheme, one evolves the positions $\{x_i\}$ and its first two derivatives velocities $\{v_i\}$ and accelerations $\{a_i\}$ in a small time interval Δt. For each step of update, the scheme involves the following procedure:

1. Evaluate $x_i(t + \Delta t) = x_i(t) + v_i(t)\Delta t + \frac{1}{2}a_i(t)(\Delta t)^2$
2. Evaluate $a(t + \Delta t)$ from the expression $(\nabla V(x(t + \Delta t)))/m$
3. Update $v(t + \Delta t) = v(t) + \frac{1}{2}(a(t) + a(t + \Delta t))\Delta t$

To integrate the second-order differential equations of each degree of freedom in equations (2.2.1), one needs to specify two initial conditions: $x_i(t = 0)$ and $v_i(t = 0)$. The initial positions are usually generated by placing the particles on a ordered lattice eg: a square lattice or a FCC lattice. The ordered positions are then evolved at a high-temperature to melt the crystalline-structure using a thermostat. The details on the thermostat will be described in the next section. The initial set of velocities $\{v_i(t = 0)\}$ are drawn from Maxwell-Boltzmann distribution corresponding to a temperature T

$$f(v) = A\ \exp\left(-\frac{mv^2}{2\,k_B\,T}\right)$$

2.2.2 Thermostat

Apart from solving the equations of motion, the particle-based system is also required to be studied at different values of intensive and extensive thermodynamic variables. One of the most common choices of the thermodynamic ensembles for studies in particle based simulations is the NVT ensemble where, the number of particles N, the volume of the system V and the temperature of the system T are fixed. In our work, we achieve this via use of Nosé–Hoover thermostat.

2.2.2.1 Nosé–Hoover thermostat

The kinetic temeperature of the system is related to the momentum (and thus velocities) of the system via the following relation:

$$\sum_{i=1}^{N} \frac{p_i^2}{2m_i} = \frac{d\,N\,k_B\,T}{2} \tag{2.2.2}$$

The most obvious way to bring the system to a target temperature would be to re-scale the velocities by a factor λ corresponding to the target temperature T by using the following relations:

$$\varDelta T = \sum_{i=1}^{N} \frac{m}{d\,N\,k_B}(\lambda^2 - 1)v^2 \tag{2.2.3}$$

The major problem with this brute-force approach lies in capturing the stochastic nature of temperature fluctuations accurately, this approach has been shown to deviate from the canonical ensemble.

To overcome this, one uses a an algorithm like Nosé–Hoover thermostat [102] which mimics canonical-ensemble better. In Nosé–Hoover algorithm, degrees of freedom corresponding to the heat bath are added to the system. The variable $\tilde{s}$ plays the role of stretching the units of time i.e. $\tilde{d}t = \tilde{s}\,dt$ but the position variables remain the same, i.e. $\tilde{r} = r$. The Lagrangian for the system with degrees of freedom corresponding to the heat bath and the rescaled time paramter $d\tilde{t}$ is given by:

$$\mathcal{L} = \sum \frac{m_i}{2}\tilde{s}^2\,\tilde{r}_i^2 - U(\tilde{r}) + \frac{1}{2}\,Q\,\tilde{s}^2 - g\,k_B\,T_0\,\ln(s) \tag{2.2.4}$$

The first two terms are the correspond to the Lagrangian of a particulate system without a thermostat with a rescaled time. The other terms involving Q (the equivalent mass of the thermostat) and the degree of freedom $\tilde{s}$ correspond to the degrees of freedom of the thermostat. The parameter $g = d \cdot N$ in d dimensions. The Euler-Lagrange equations of motion corresponding to the the Lagrangian in 2.2.4 are given by,

$$\ddot{r} = \frac{\tilde{\boldsymbol{F}}_i}{m_i\,\tilde{s}^2} - 2\frac{\dot{\tilde{s}}\dot{\tilde{r}}_i}{\tilde{s}} \tag{2.2.5}$$

$$\ddot{\tilde{s}} = \frac{1}{Q\tilde{s}}\left(\sum_i m_i\tilde{s}^2\dot{\tilde{r}}^2 - gk_BT_0\right) \tag{2.2.6}$$

Solving the equations (2.2.5) & (2.2.6) numerically by using a velocity-verlet leads to simulation of a system coupled to a thermostat at temperature T_0. For effective implementation of the Nosé–Hoover thermostat, choosing the value of the parameter Q – the effective mass is very essential. Choosing a large value of Q, leads to poor thermostating, as it is easy to see that large Q limit i.e. $Q \to \infty$ effectively is just plain MD without any thermostat. Where as, a very small value of $Q \to 0$ would lead to very high-frequency oscillatory behaviour which is also unrealistic. Once an appropriate value of Q is chosen, the scheme leads to an accurate representation of evolution of system in the NVT ensemble.

In most of our simulations discussed in the later chapters, for generating the initial states for our investigations on mechanical deformation, we first use the Nosé–Hoover thermostat to equilibrate the glass-forming 2DKA mixture discussed in previous sections, at a high-temeprature $T = 1.0$ system followed by cooling it to a low temperature $T = 0.01$ at a rate $\dot{T} = 10^{-4}$ per MD timestep.

2.3 Energy Minimization

The states cooled down to $T = 0.01$ are subject to energy minimization via conjugate gradient algorithm, to obtain the inherent structures of the model system. Further, for carrying out energy-minimization during quasistatic-simulations, we use the conjugate gradient scheme [103] described below. The minimization of energy stops when the relative energy difference between two successive steps reaches the threshold i.e. $(\mathit{\Delta} E/E) < 10^{-16}$.

2.3.1 Conjugate gradient minimization

Let the multidimensional function to be minimised be approximated by, a quadratic function in the small neighbourhood around the point x using the Taylor series.

$$f(\boldsymbol{x}) \approx c - \boldsymbol{b} \cdot \boldsymbol{x} + \frac{1}{2} \boldsymbol{x}\, \boldsymbol{A}\, \boldsymbol{x}$$

To minimize a complicated function $f(x)$ by searching in various directions, one needs to move on the landscape of function $f(\boldsymbol{x})$ with smart choice of directions to minimize the computational costs. For a complicated multi-dimensional function, one usually minimizes the function along the different set of directions $\{\boldsymbol{x}_i\}$ in each step until a minimum is reached within a certain tolerance. Minimization along a particular direction x_i on the landscape of the function f is carried out using line-search algorithms. These algorithms iteratively move in the direction $\boldsymbol{x_i}$ with varying step-size until a minimum is found within the desired tolerance.

The simplest way to minimize the function would be to successively minimize the functions the gradient directions independently. To do so, one just uses Gram-Schmidt-like iterative algorithm to find orthogonal directions, such an algorithm is known as steepest-descent (SD) minimization scheme.

$$x_{i+1} = x_i - \gamma_i \nabla f|_{x_i}$$

Even though the steepest-descent algorithm works, the convergence to the minimum of function during the last-steps of the minimization is very slow. To avoid this drawback, in Conjugate Gradient (CG) algorithm, one constructs search directions x_{i+1} smartly. One usually starts by choosing a random direction $\boldsymbol{x}_0 = -\nabla_0 f$ i.e. the direction of the negative of the gradient at the starting point P_0. Minimising using a line-search algorithm in the direction of $\boldsymbol{x}_0$ leads to the point P_1. Now at P_1 instead of choosing the gradient direction again, one typically includes a history-dependent correction for the new-search direction. i.e.

$$\boldsymbol{x}_1 = \boldsymbol{x}_0 - \gamma_i(\nabla f + \boldsymbol{x}_0)$$

The correction attempts to takes into account the fact that on successive changes of directions, the minimum found by line-search in previous steps could change. Mathematically, $min(P_i)$ along the direction x_i is not necessarily the same as the $min(P_{i+1})$ along the direction x_i. The direction of ∇f is just determined by the derivative at the point P_i and there exist multiple-schemes to choose the history dependent parameters γ_i. Depending on the type of function at hand, different schemes might be useful. The most preferred one is the Polak–Ribière scheme where-in one chooses the γ_i using the following expression.

$$\gamma_i = \frac{(\nabla_{i+1} f - \nabla_i f) \cdot \nabla_{i+1} f}{\nabla_i f \cdot \nabla_i f}$$

The subscript refers to the step number in which the gradient of the function is calculated. The algorithm for carrying out energy-minimization using the Conjugate-Gradient minimization using Polak–Ribière scheme [103] could thus be summarised as follows:

1. Initialize the search direction as $\boldsymbol{x}_0 = -\nabla_0 f$
2. Using line-search, find the minimum in the direction of $\boldsymbol{x}_0$ to obtain the point P_0
3. In the loop, iterate over the loop variable i, until $f(P_{i+1}) - f(P_i) < u_{tol}$:
    (a) Using the gradient at point P_i, calculate, $\boldsymbol{x}_i = \boldsymbol{x}_{i-1} - \gamma_i(\nabla f_i + \boldsymbol{x}_{i-1})$ with $\gamma_i = \frac{(\nabla_{i+1} f - \nabla_i f) \cdot \nabla_{i+1} f}{\nabla_i f \cdot \nabla_i f}$
    (b) Line-search minimization along the direction $\boldsymbol{x}_i$ to find the next point P_{i+1}

2.4 Hessian Matrices and diagonalisation

The potential energy or for that matter any continuous & differentiable multi-variable function $U(\{x_i\})$ can be expanded in Taylor series around a point whose position vector is given by a tuple $\{x_0\}$,

$$U(\{x\}) = U(\{x_0\})+\sum_i \frac{\partial U}{\partial x_i}\cdot(x_i-x_{0\,i})+\sum_{i,j} \frac{\partial^2 U}{\partial x_i \partial x_j}(x_i-x_{0\,i})(x_j-x_{0\,j})+\mathcal{O}((x_i-x_{0\,i})^3) \quad (2.4.1)$$

If the system resides in a potential energy extremum or a force balanced state, the first-derivative $\frac{\partial U}{\partial x_i} \rightarrow 0$, thus the change in energy around the point $\{x_0\}$ is approximated by,

$$U(\{x\}) - U(\{x_0\}) = \delta U = \sum_{i,j} \frac{\partial^2 U}{\partial x_i \partial x_j}(x_i - x_{0\,i})(x_j - x_{0\,j}) + \mathcal{O}((x_i - x_{0\,i})^3) \qquad (2.4.2)$$

The matrix of second derivatives

$$\mathcal{H}_{ij}^{\alpha\beta} = \frac{\partial^2 U}{\partial x_i \partial x_j} \qquad (2.4.3)$$

is a symmetric matrix termed as the Hessian. It follows from the second derivative test for multivariable functions that, if the eigenvalues of the Hessian matrix (λ_i) are all positive i.e. $\forall i,\ \lambda_i > 0$, the force balanced state $\partial U/\partial x_i = 0$ is a stable local-minimum. If the eigenvalues of the Hessian matrix are all negative i.e, $\lambda_i < 0\, \forall\, i$, the force-balanced state is a unstable energy maximum. If the eigenvalues of the Hessian matrix have both positive and negative eigenvalues, the system resides in an unstable saddle-point.

In the context of the potential energy landscape as discussed in the Chapter 1, calculation of this Hessian matrix and the eigenvalues gives crucial information about the stability of force-balanced states for a given configuration. In the later chapters, we examine the stability of energy minima near plastic-instabilities and in this context we diagnoalize the Hessian matrices near the point of instabilities to study the nature of the bifurcation processes leading to a sudden plastic instability.

To diagonalize the Hessian matrix $\mathcal{H}_{ij}^{\alpha\beta}$, we use the dsyevr function from the LAPACKE library [104]. The dsyevr function from the LAPACK library, first reduces the Hessian matrix to a tri-diagonal form via use of similarity transformations, i.e. $\mathcal{H}_{ij}^{\alpha\beta} \rightarrow Q^T \mathcal{H}_{ij}^{\alpha\beta} Q$ by determining the matrix Q. The tri-diagonal form of the reduced Hessian matrix provides an ideal setup to use the fast dqds algorithm [105] for calculation of eigenvalue spectrum of the $\mathcal{H}_{ij}^{\alpha\beta}$. The dqds algorithm involves an iterative procedure to diagonalise the matrix. The tolerance for calculation of the eigenvalues of the Hessian matrix in our calculations is set to 10^{-13} for the use of dsyevr function from LAPACKE.

2.5 Boundary conditions

For carrying out our particle based simulations we use periodic boundary conditions. Under such boundary conditions one usually aims to explore the properties of the bulk of the system without worry about the surface-effects. Calculating the distances between any two particles is essential to calculating the forces between them and thus also essential to simulate the time evolution of the system.

2.5.1 Minimum Image convention for a square box

Under periodic boundary conditions, one visualises multiple copies/images of the system surrounding the system, as illustrated in the Figure. 2.1. The multiple images of the system are considered all equivalent. The distance between the blue particle and the red-particle corresponds to the least possible distance between blue particle and red particle among nine independent copies of the system shown in Figure 2.1. This protocol is referred to as minimum image convention. For two particles, with coordinates, $r_1 \equiv (x_1, y_1)$ and $r_2 \equiv (x_2, y_2)$, the first step to calculate the distance between them is evaluating the

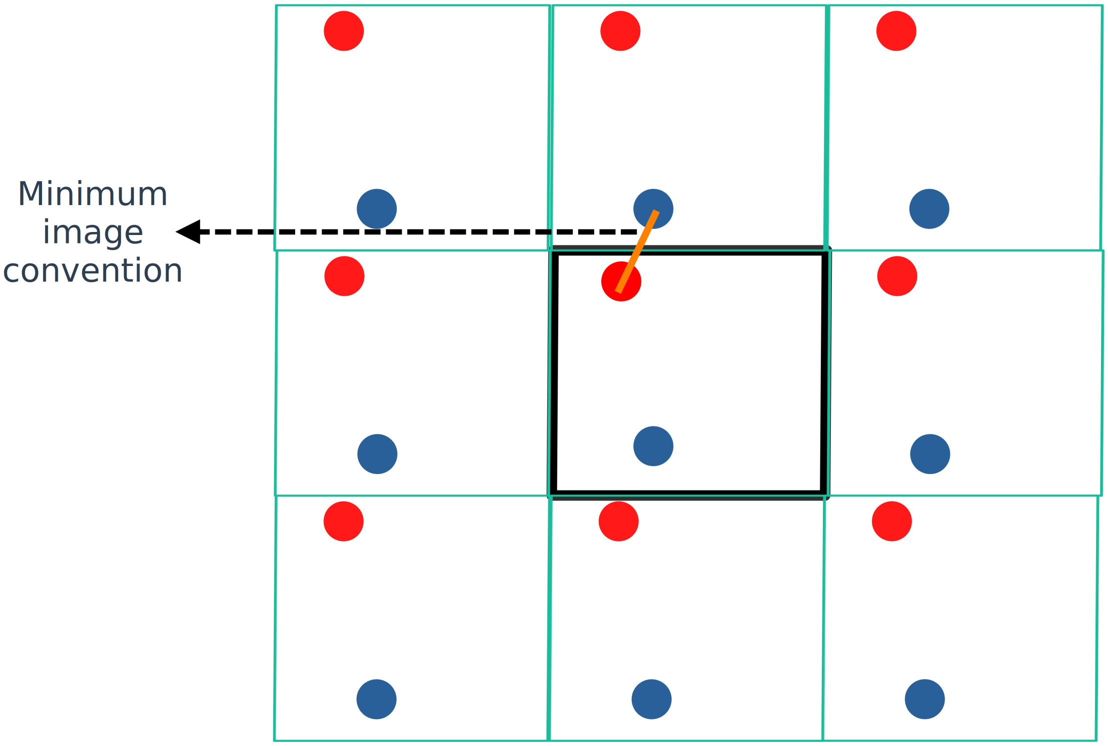

Figure 2.1. A figure illustrating distance calculation between two particles under periodic boundary conditions for a square box.

minimum difference in x i.e. Δx among all possible images and analogously minimum difference in y i.e. Δy. For a square box of length L, this is simply given by,

$$\Delta x = min(| x_2 - x_1 |, | | x_2 - x_1 | - L |) \; \& \tag{2.5.1}$$

$$\Delta y = min(| y_2 - y_1 |, | | y_2 - y_1 | - L |) \tag{2.5.2}$$

The distance between blue and the red particle is now simply given by,

$$d^2 = (\Delta x)^2 + (\Delta y)^2 \tag{2.5.3}$$

2.5.2 Minimum image convention for a triclinic (sheared) box

In the previous section, we have highlighted the enforcement of periodic boundary conditions for the square box. But when the shape of the box is changed as in the case of studies

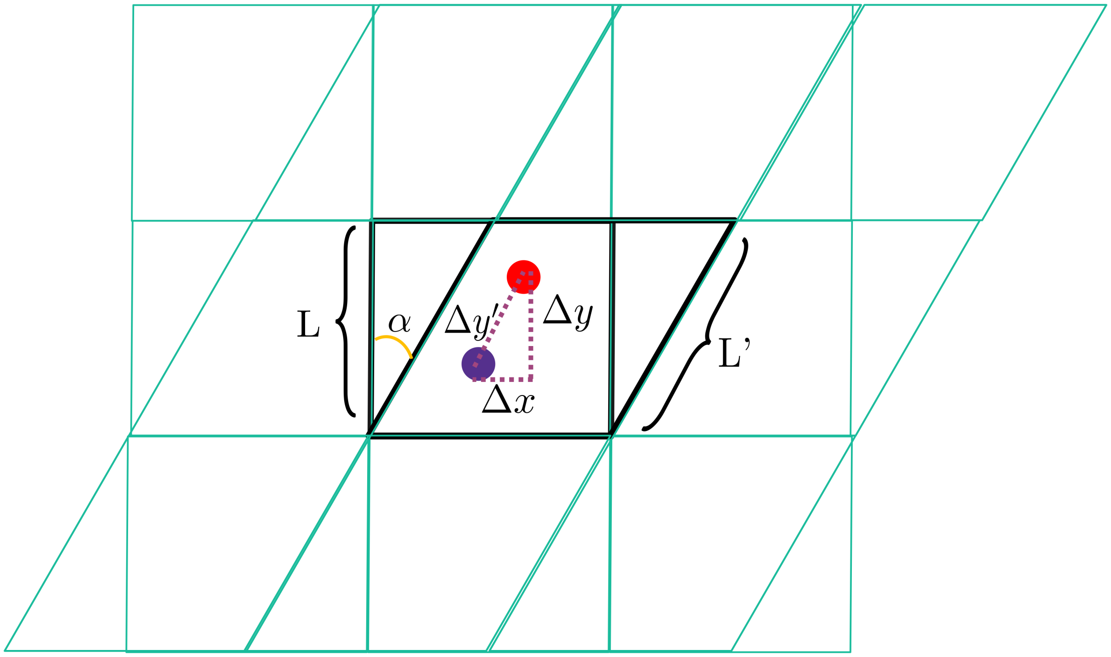

Figure 2.2. A figure illustrating distance calculation between two particles under periodic boundary conditions for a sheared triclinic box.

of shear deformation, the recipe for calculation of distances between two particles is modified due to presence of oblique axes. The distance calculation under periodic boundary conditions in a tri-clinic box, is best explained using the Figure 2.2. A square-box with PBC is tilted to a shear strain of tan(α), as one would expect, the neighbouring images are tilted too. The major change in a triclinic box from a square box is the oblique axes. Thus, wrapping of the coordinates and the wrapping of differences of coordinates are done along this oblique pair of axes X' and Y'. So one first converts the x and y coordinates of the particles to oblique coordinates using the following relations:

$$x' = x - y \cdot \tan(\alpha) \tag{2.5.4}$$

$$y' = y/\cos(\alpha) \tag{2.5.5}$$

Now in this oblique coordinates, one calculates the wrapped differences in the coordinates, i.e.

$$\Delta x' = (x'_2 - x'_1)\% L_x \tag{2.5.6}$$

$$\mathit{\Delta} y' = (y'_2 - y'_1)\% L_y \tag{2.5.7}$$

Now these differences in oblique coordinates can be used to convert to differences in orthogonal coordinates using the inverse relations of equation(2.5.4) i.e.

$$\mathit{\Delta} x = \mathit{\Delta} x' + sin(\alpha)\,\mathit{\Delta} y' \tag{2.5.8}$$

$$\mathit{\Delta} y = \cos(\alpha)\,\mathit{\Delta} y' \tag{2.5.9}$$

The distance between two particles now is thus given by,

$$d^2 = (\mathit{\Delta} x)^2 + (\mathit{\Delta} y)^2 \tag{2.5.10}$$

3 Athermal quasistatic expansion: elasto-plastic phenomenology

In this chapter, we explore the elasto-plastic phenomenology of the response of an amorphous solid to athermal quasistatic expansion starting from a homogenous high-density solid regime. We find that upon expansion, the solid undergoes a yielding-like transition accompanied by cavitation of the solid. The cavities grow and merge on further expansion, eventually resulting in a system-spanning crack. We show that all the plasticity encountered under expansion, be it in the elastic-branch or during the growth of cavities, occurs via a saddle-node bifurcation on the potential energy landscape as seen for the case of plasticity under shear. The statistics of avalanche-sizes after yielding are shown to have a sub-extensive & scale-free nature as observed for plastic events under simple shear but with different exponents. All in all, we reveal universal characteristics in the plasticity of amorphous solid under any kind of mechanical-deformation by connecting the results of athermal quasistatic expansion to that of athermal quasistatic shear.

3.1 Introduction

The underlying energy landscape of amorphous materials is complex, and analysing the material properties through the landscape's features, especially the local minima (called inherent structures (IS)) and saddles, is a domain of active research as discussed in previous chapters. In the context of the material's response to athermal quasistatic shear (AQS) [17, 28], i.e. at vanishing driving rate and in the absence of thermal noise, it has been demonstrated that, during the straining process, yielding happens via the occurrence of irreversible plastic events and each such event can be considered as a catastrophic process corresponding to a saddle node bifurcation within the energy landscape, i.e. whenever an event occurs, the smallest non-zero eigenvalue of the Hessian matrix, $\mathcal{H}_{ij}^{\alpha\beta}$ (defined later) vanishes via a square root of the difference of strain and the value of strain at which the plasticity occurs [17, 28, 35, 38]. The saddle-node bifurcation implies presence of a single unstable direction on the landscape and also leads to divergence of elastic constants near every plastic event with the same power laws [35]. These power-laws have also been used to predict the value of strain at which plastic event occurs for the case of plastic events under shear [36]. The vanishing of λ_{min} as a square-root of strain is not necessarily the same in other deformation processes across different systems, for example in a granular assembly of spheres in the presence of frictional forces, the plastic event leads to a different bifurcation process and it has been demonstrated in Ref. [18] that two real eigenvalues can merge and give rise to two imaginary eigenvalue pair instead of vanishing of the lowest eigenvalue.

Further, analyzing the statistical properties of the plastic events is also of significance. In the case of AQS steady state, it has been shown [38,106] that the mean drops in energy and stress respectively scale as $\langle \Delta U \rangle \sim N^{\alpha}$, $\langle \Delta\sigma \rangle \sim N^{\beta}$, where $\alpha = 1/3$ and $\beta = -2/3$ being universal exponents in both two and three dimensions across different model systems.

It is pertinent to ask whether other quasi-static mechanical deformations also involve similar singularities and follow similar statistics. A priori, it is not evident that spontaneous emergence of density inhomogeneities in the form of cavity formation, under expansion, would correspond to a failure via saddle of index 1. A recent study using a one-component system, which potentially crystallizes at low temperatures, seemed to show that at the instant of cavitation of the solid, a saddle-node bifurcation does occur [107]. However, the study specifically focused near the Sastry density, i.e. where IS states start to show spatial inhomogeneities [75], using states obtained through thermal quench from a high-temperature liquid state at this density and then probing its stability. The behaviour at higher or lower densities and specifically IS states sampled at low temperatures was not studied.

3.2 Objective

The main objective of this study is to understand the mechanical response of an amorphous solid to athermal quasistatic expansion where cavitation instabilties are expected to occur. It is well known that these instabilities can lead to fracture. Thus we aim to understanding mechanisms on the potential energy landscape via which cavitation instabilities occur in this study. The statistics of avalanches that lead to cavitation driven fracture serve as a good comparison between a meso-scale elasto plastic model and numerical simulations, statistics should be accessible via acoustics in experiments. As result, here we also aim to probe the statistics of drop-sizes that lead to growth of fracture via cavitation in numerical simulations.

3.3 Model & Methods

3.3.1 Model

We use the two-dimensional model binary Lennard-Jones mixture, Kob-Anderson model [96, 97] as a primary model for our study which is described in detail in the Chapter 2. We also use the 3D Kob-Andersen model, 3D-Wahnstorm mixture and 2D Lancon et al. model to check the universality of the saddle-node bifurcation. The details of these models too have been described in Chapter 2.

3.3.2 Preparation of initial state

The initial states are prepared via cooling a high temperature liquid at temperature $T = 1.0$ to a temperature $T = 0.01$ at a cooling rate of 10^{-4} temperature units per MD timestep [108] for the 2D Kob-Andersen model. For the other models, initial states were prepared directly by quenching the high-temperature liquid to $T = 0$.

3.3.3 Protocol

To subject the solid to uniform expansion, first the size of the square box is expanded $L' = L(1+\epsilon)$ followed by rescaling of the particle coordinates such that the scaled coordinates remain the same. The values of ϵ vary from 5×10^{-4} to 10^{-9}. This imposes a volume strain on the system. The expanded simulation box is then allowed to relax its energy via conjugate gradient (CG) [103] energy minimization. The energy minimization corresponds to taking the limit, temperature $T \rightarrow 0$ & time $t \rightarrow \infty$. As a result, the volume strain rate $\dot{\gamma} \rightarrow 0$. We thus term this is athermal quasistatic expansion (AQE) to draw the analogy with the well-studied athermal quasistatic shear (AQS) [28]. This procedure of straining the box followed by energy minimization is continued in a loop. A similar protocol in the the context of exploring the cavitation transition in the energy landscape of cohesive liquids was employed by Altabet et al [85, 86]. The simulations are performed using LAMMPS [109].

3.3.4 Calculation of Hessian matrix

For a pairwise interaction potential between the particles ϕ_{ij}, the potential energy of the system is given by,

$$U(r) = \frac{1}{2}\left[\sum_{i,j=1;i\neq j}^{N} \phi_{ij}\right] \tag{3.3.1}$$

The Hessian matrix is defined as,

$$H^{ij}_{\alpha\beta} = \frac{\partial^2 U}{\partial x^i_\alpha \partial x^j_\beta} \tag{3.3.2}$$

Substituting, (3.3.2) in (3.3.1) gives,

$$H^{ij}_{\alpha\beta} = \frac{\partial^2 U}{\partial x^i_\alpha \partial x^j_\beta} = \frac{1}{2}\frac{\partial}{\partial x^j_\beta} \sum_{k,l;k\neq l} \frac{\partial \phi(r_{kl})}{\partial r^{kl}} \frac{\partial r^{kl}}{\partial x^i_\alpha} = \frac{1}{2}\frac{\partial}{\partial x^j_\beta} \sum_{k,l;k\neq l} \frac{\phi_r \, r^{kl}_\alpha}{r^{kl}} (\delta^{il} - \delta^{ik})$$

$$= \frac{1}{2}\frac{\partial}{\partial x^j_\beta}\left[\left(\sum_{k,i;k\neq i} \phi_r \frac{r^{ki}_\alpha}{r^{ki}}\right) - \left(\sum_{i,l;i\neq l} \phi_r \frac{r^{il}_\alpha}{r^{il}}\right)\right] = \frac{1}{2}\frac{\partial}{\partial x^j_\beta}\left[\left(\sum_{k,i;k\neq i} \phi_r \frac{r^{ki}_\alpha}{r^{ki}}\right) + \left(\sum_{l,i;l\neq i} \phi_r \frac{r^{li}_\alpha}{r^{li}}\right)\right]$$

$$= \frac{\partial}{\partial x^j_\beta}\left(\sum_{k,i;k\neq i} \phi_r \frac{r^{ki}_\alpha}{r^{ki}}\right) = \sum_{k,i;k\neq i}\left[\frac{r^{ki}_\alpha}{r^{ki}} \frac{\partial \phi_r}{\partial x^j_\beta} + \phi_r \, r^{ki}_\alpha \frac{\partial}{\partial x^j_\beta}\left(\frac{1}{r^{ki}}\right) + \frac{\phi_r}{r^{ki}} \frac{\partial r^{ki}_\alpha}{\partial x^j_\beta}\right]$$

$$= \sum_{k,i;k\neq i}\left[\frac{r^{ki}_\alpha}{r^{ki}} \frac{\partial \phi_r}{\partial r^{ki}} \frac{\partial r^{ki}}{\partial x^j_\beta} - \frac{\phi_r \, r^{ik}_\alpha}{(r^{ik})^2} \frac{\partial r^{ik}}{\partial x^j_\beta} + \delta_{\alpha\beta}(\delta^{ji} - \delta^{jk}) \frac{\phi_r}{r^{ki}}\right]$$

$$= \sum_{k,i;k\neq i}\left[\phi_{rr} \frac{r^{ki}_\alpha}{r^{ki}} \frac{r^{ki}_\beta}{r^{ki}} (\delta^{ji} - \delta^{jk}) - \frac{\phi_r \, r^{ik}_\alpha}{(r^{ik})^2} \frac{r^{ik}_\beta}{r^{ik}} (\delta^{ji} - \delta^{jk}) + \delta_{\alpha\beta}(\delta^{ji} - \delta^{jk}) \frac{\phi_r}{r^{ki}}\right]$$

$$\boxed{H^{ij}_{\alpha\beta} = -\sum_{k,i;k\neq i}\left[\left(\frac{\phi_r}{(r^{ik})^3} - \frac{\phi_{rr}}{(r^{ki})^2}\right) r^{ki}_\alpha r^{ki}_\beta - \delta_{\alpha\beta} \frac{\phi_r}{r^{ki}}\right] (\delta^{ji} - \delta^{jk})} \tag{3.3.3}$$

Here $\phi_r = \partial \phi(r_{ij})/\partial r^{ij}$ and $\phi_{rr} = \partial^2 \phi(r_{ij})/\partial (r^{ij})^2$. For off-diagonal terms, $i \neq j$ implies $\delta^{ij} = 0$,

$$\boxed{H^{ij}_{\alpha\beta} = -\sum_{i,j;i\neq j}\left[\left(\frac{\phi_r}{(r^{ij})^3} - \frac{\phi_{rr}}{(r^{ij})^2}\right) r^{ij}_\alpha r^{ij}_\beta - \delta_{\alpha\beta} \frac{\phi_r}{r^{ij}}\right]} \tag{3.3.4}$$

For diagonal terms, $i = j$ together with condition in the sum of (3.3.3), $k \neq i$ implies,

$(\delta^{ji} - \delta^{jk})$ simplifies to δ^{ii}. Therefore the hessian becomes,

$$H^{ii}_{\alpha\beta} = \sum_{j \neq i} H^{ij}_{\alpha\beta} \tag{3.3.5}$$

Using the simplified expression in (3.3.4) and the relation (3.3.5), we calculate the Hessian matrix for a given configuration. The Hessian matrix is then diagonalised using LAPACKE [104].

3.4 Results

3.4.1 Yielding

We track the hydrostatic pressure P and energy per particle of the the solid U/N as a function of ρ as the solid is expanded. Upon expansion, the pressure of the solid decreases and at some point, the pressure even becomes negative as shown in the ensemble averaged data for different system sizes 3.1(a) and for an individual trajectory for $N = 10^5$ in 3.2(b). The negative pressure implies expansive tension in the solid. The point at which the pressure crosses the $P = 0$ line, the energy of the solid goes through a minimum in the U/N *vs* ρ plane 3.1(b). After a certain point, under expansion, the system releases the built-up tension via a large pressure jump (see 3.2(a)) which is accompanied by cavitation of the solid (3.2(c)). The ensemble averaged $P - \rho$ & $U/N - \rho$ curves in 3.1(a) & 3.1(b) too show signs of a large pressure-jump and energy drop. On continuing the expansion, more such pressure-jumps and energy-drops are encountered. These pressure jumps and energy drops correspond to either growth of the earlier cavity in the system or formation of the new cavities in the system. These cavities eventually merge or grow leading to a system-spanning fracture of the solid. Figure 3.2 (b)-(g) shows the snapshots of the solid

We characterize the pressure fluctuations over the ensemble for the expanding solid as

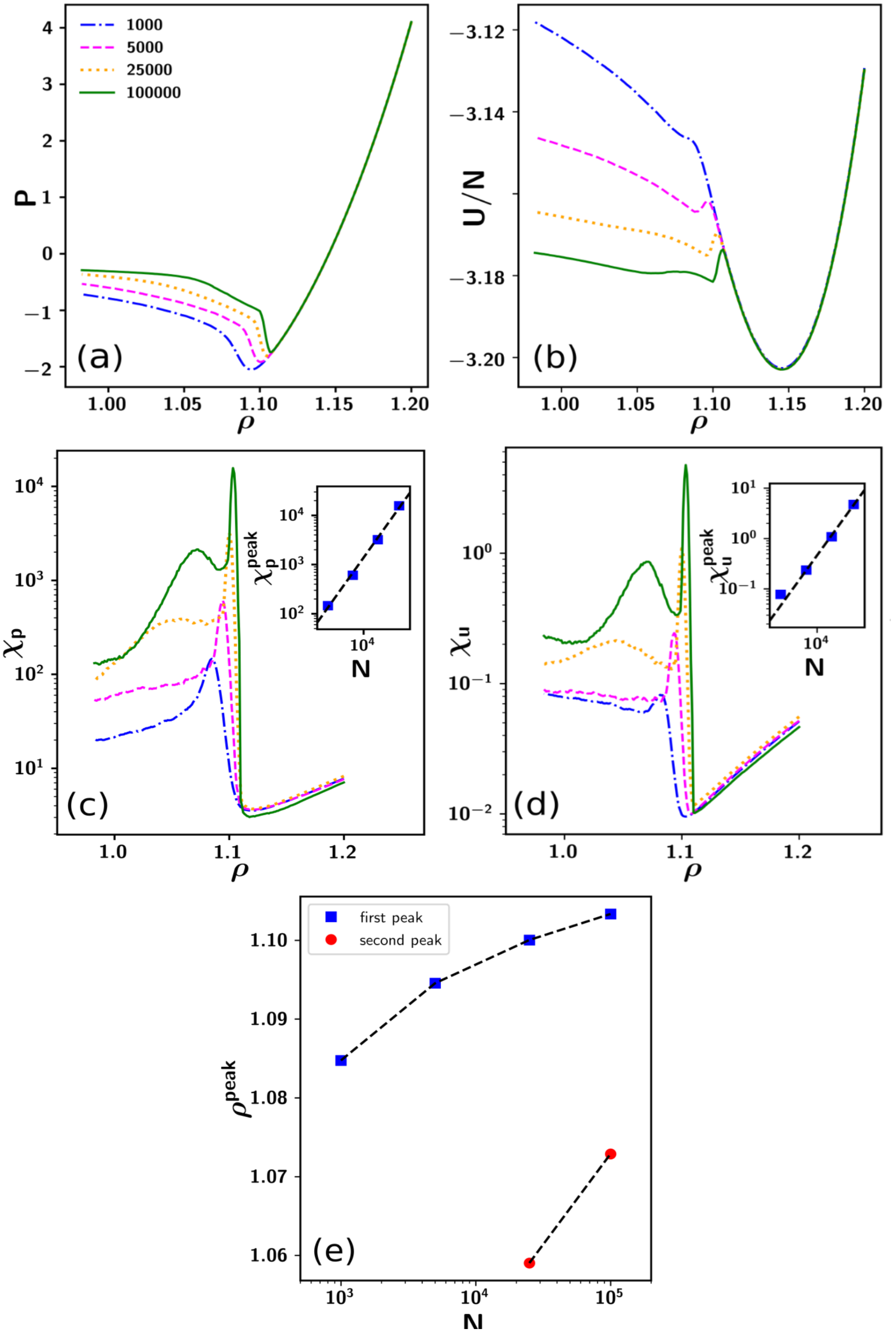

Figure 3.1. For different system sizes and averaged over ensembles, (a) Pressure P vs Density ρ curve (b) Energy per particle U/N vs Density ρ (c) Pressure susceptibility, inset: system-size scaling of the pressure susceptibility peak, $\chi_p^{peak} \sim N$ (d) Energy susceptibility, inset: system-size scaling of the energy susceptibility peak, $\chi_u^{peak} \sim N$ (e) Density dependence of the first and second peaks in the susceptibility.

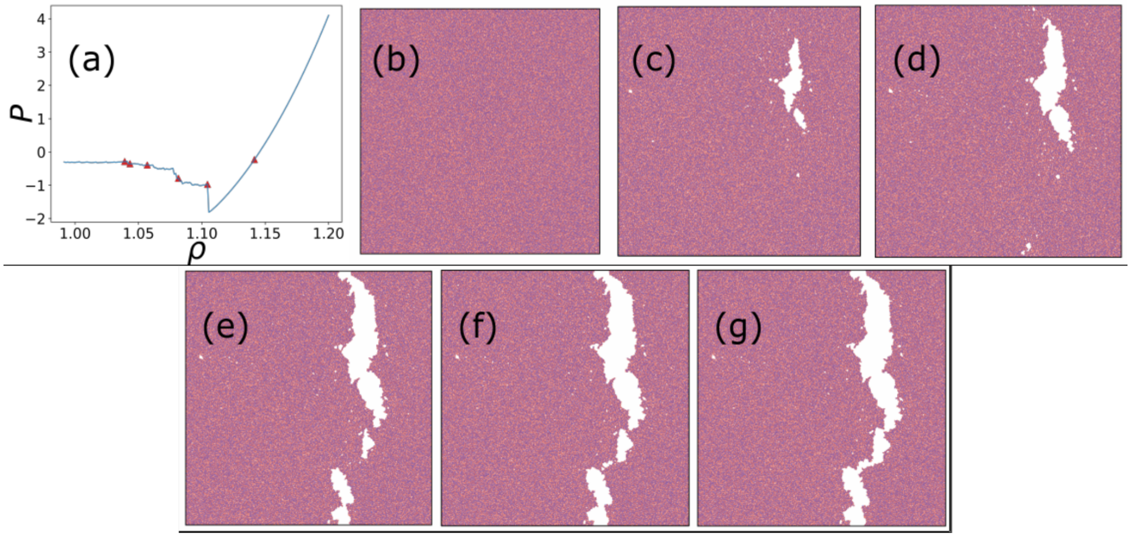

Figure 3.2. For a trajectory of $N = 10^5$, (a) The pressure jumps marked in red on the $P - \rho$ curve (b)-(g) Snapshots of the solid at the points marked in (a).

a function of density, using a susceptibility defined [25] as, $\chi_p(\rho) = N\left(\langle P^2(\rho)\rangle - \langle P(\rho)\rangle^2\right)$ and analogously the fluctuations in energy as $\chi_u(\rho) = (1/N)\left(\langle U^2(\rho)\rangle - \langle U(\rho)\rangle^2\right)$. The angular brackets $\langle . \rangle$ denote averages across the independent copies of the system that constitute the ensemble. We find that the susceptibilities as a function of density ρ shows a peak at the first big jump in pressure and the point of big drop in energy. This peak becomes sharper with increasing system size and the peak height for both the susceptibilities scales as $\chi^{peak} \sim N$ (see insets of 3.1(c) & 3.1(d)). The extensive scaling of the susceptibility suggests a macroscopic stress drop [110] as seen in the context brittle-like yielding under shear in the athermal quasistatic limit [25]. For larger system sizes, a secondary peak in the susceptibilities is also visible, which corresponds to large pressure-jumps due to merging of cavities or complete fracture of the solid. The second peak also occurs for smaller system sizes too but at lower values of density. The variation of density of first peaks and the second peaks with density is shown in the 3.1(e). The first and the second peaks seem to move closer to each other with increasing system size. Whether the two peaks intersect in the thermodynamic limit $N \to \infty$ or not, remains an open question. The location of the peaks might also vary with annealing of the initial state at the starting of expansion. More light will be shed on this in our future work which is beyond the scope of this thesis.

3.4.2 Irreversible pressure-jumps

The pressure-jumps and energy-drops correspond to irreversible rearrangements of particles in the simulations. By irreversibility here, we mean, the system doesn't relax to the same initial microstate when driven to the previous value of strain. We refer to this irreversibility as plasticity and the corresponding events as plastic events. Thus cavitation too is an example of plasticity. To probe this plasticity on the potential energy landscape, we diagonalize the Hessian of potential energy $H_{ij}^{\alpha\beta} = \partial^2 U/\partial x_i^\alpha \partial x_j^\beta$, where i & j run over particle indices where as α & β represent the axes x and y. In the context of shear, the lowest non-zero eigenvalue of the hessian λ_{min} is known to go to zero as a function of difference of strain from the point of plastic event [17, 28] i.e, $\lambda_{min} \sim \sqrt{\gamma_c - \gamma}$ and this corresponds to a saddle-node bifurcation (see 3.4) [28] on the potential energy landscape at the point of plasticity. In our case, we too find that λ_{min} goes to zero near each irreversible plastic event as shown in 3.3(a) & 3.3(b). On plotting λ_{min} as a function of $(\rho - \rho_c)/\rho_c$ where ρ_c is the density at which the plastic instability occurs, we find that $\lambda_{min} \sim \sqrt{\rho - \rho_c}$ near each plastic event, see 3.3(c). The different curves in 3.3(c), represent the square-root power laws for different models (details in caption) of amorphous solids in both 2D and 3D. For each plastic instability, the λ_{min} is scaled appropriately to organise the data on single line for a given model. It can be shown that $\rho - \rho_c \propto \delta\gamma_{vol}$, where $\delta\gamma_{vol}$ is the volume strain difference. The other eigenvalues remain non-zero until the point of plasticity. The fact that only one eigenvalue $\lambda_{min} \to 0$ implies that the displacement fields $\vec{d}$ between consecutive steps of athermal quasistatic expansion on approach on approach to the point of plasticity is predicted by the eigenvector in the previous step, $\vec{e}$, i.e. $\hat{e} \cdot \hat{d} \to 1$ on approach to the point of plasticity. This is demonstrated in 3.3, where the column (d) shows the spatial map of eigenvector of λ_{min} near instabilities and the corresponding spatial map of displacement field is shown in column (e). Analogous to the plastic events

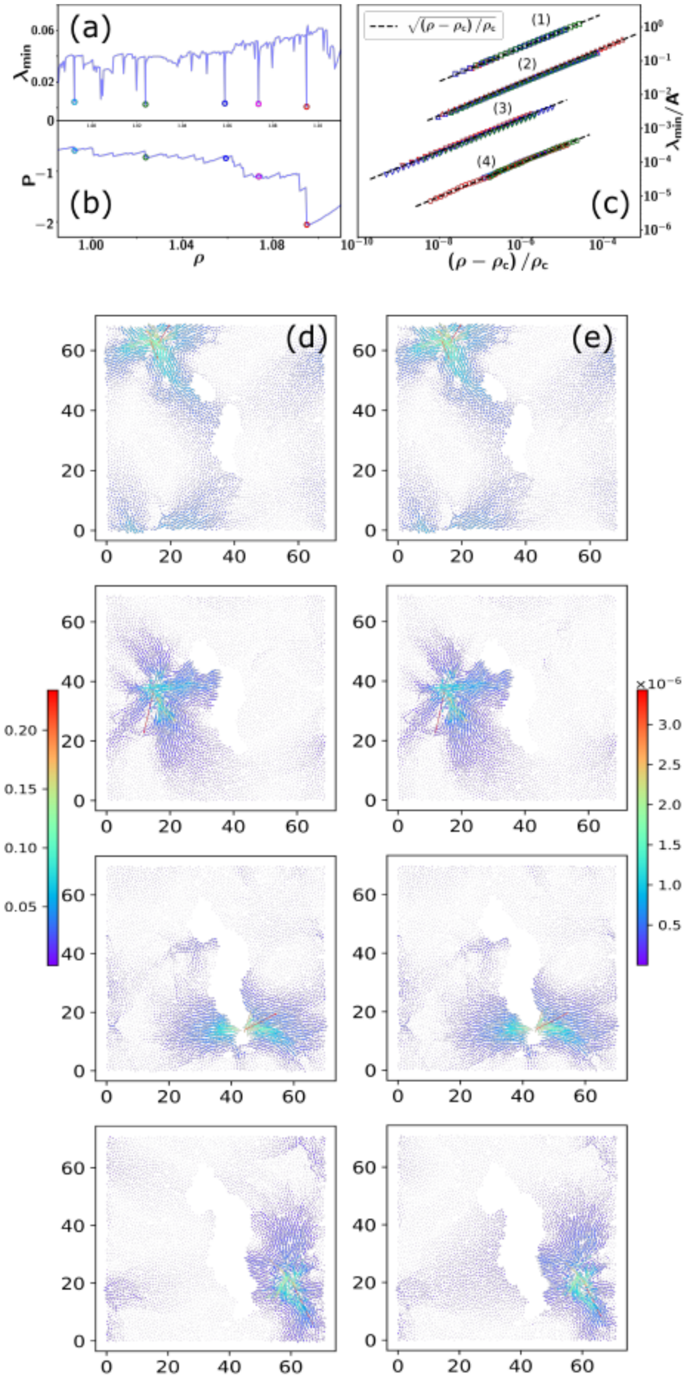

Figure 3.3. (a) The lowest non-zero eigenvalue of the Hessian of potential energy λ_{min} vs density ρ (b) The corresponding patch of P-ρ trajectory (c) Near the pressure-jumps marked in (a), λ_{min} as a function of $(\rho-\rho_c)/\rho_c$ for different models of amorphous solids (1) 2D Kob-Andersen model(shown in (a) & (b)) (2) Model from Lancon et al. (3)3D Kob-Andersen (4) Wahnstorm mixture in 3D. Columns (d) & (e) show the spatial maps of eigenvectors of λ_{min} and the corresponding displacement map on approach to a plastic jumps marked jumps in (a).

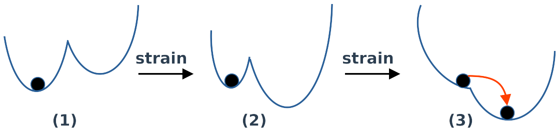

Figure 3.4. A schematic illustrating the mechanism of saddle-node-bifurcation on the potential energy landscape.

under shear [17,28], vanishing of only λ_{min} near a plastic instability implies the existence of a saddle-node bifurcation on the potential energy landscape near each plastic instability. In such a scenario of saddle-node bifurcation, the strain destabilises the energy minimum where the system is residing on the potential energy landscape and makes it a saddle with only one unstable direction as illustrated in the schematic 3.4.

3.4.3 The Yielding avalanche

In the previous section, we showed how the eigenmode of λ_{min} predicts the displacement field on approach to a plastic instability. Henceforth, we also track the displacement field across the plastic instability and compare it with the spatial map of eigenvector of λ_{min}. The displacement fields do not necessarily share a high overlap with the eigenvector just before the drop as shown in Figure.3.5. This suggests that on the potential energy landscape, there are multiple direction changes that occur before the system settles into an another energy minimum. This is also known as a cascade or an avalanche of plasticity. These avalanches are observed for amorphous plasticity under shear too [28, 106] and hence the approaches to predicting plasticity from the structural [111] information in amorphous solids are important.

3.4.4 Statistics of avalanches

Post the main cavitation/yielding event, the pressure does not reach a steady state unlike the case of shear stress under shear deformation. The fluctuations of pressure (and energy) captured by χ_p (&χ_u), do not reach a constant value after the yielding event. Despite that, just to get an idea of the scale of pressure-drops and energy drops that should be accessible via acoustic analysis of fracture of such a solid, we look at the distributions of the pressure jumps ΔP and energy drops ΔU after the first main cavitation event for different system sizes. We find that the distributions have a weibull-like shape but they do not fit perfectly with weibull-functions, see Figure 3.6(a) & Figure 3.6(b). It is not immediately obvious why pressure jumps and energy drops in the post-yield should show extreme value statistics which is expected for the first plastic drop as shown before for AQS studies [106]. Moreover, the distributions themselves show nice power-law behaviour at small arguments as $P(\Delta P) \sim \Delta P^{\eta}$ and $P(\Delta U) \sim \Delta U^{\theta}$, with $\eta \simeq 0.91$ and $\theta \simeq 0.93$ as shown in Figure 3.6 (c) & Figure 3.6 (d) by the solid lines. However, the distributions for different system sizes in our case, collapse on scaling the argument by $N^{-0.34}$ for ΔP distributions and by $N^{0.53}$ for ΔU distributions as shown in Figure 3.6(c) & Figure 3.6(d). The means of the distributions for different system-sizes too scale with the same exponents(see the insets in Figure 3.6(c) & Figure 3.6(d)). The values of exponents for the collapse of pressure distributions and the energy distributions are different from those seen for post-yield plastic events under athermal quasistatic shear. But it needs to be noted that there is no post-yield steady state corresponding to flow here and also the volume is not constant. To summarise, the statistics of post-yield pressure-jumps and energy-drops suggest a scale-free nature of the plasticity as the distributions just depend on the system size but understanding why the distributions have a weibull-like shape warrants further studies.

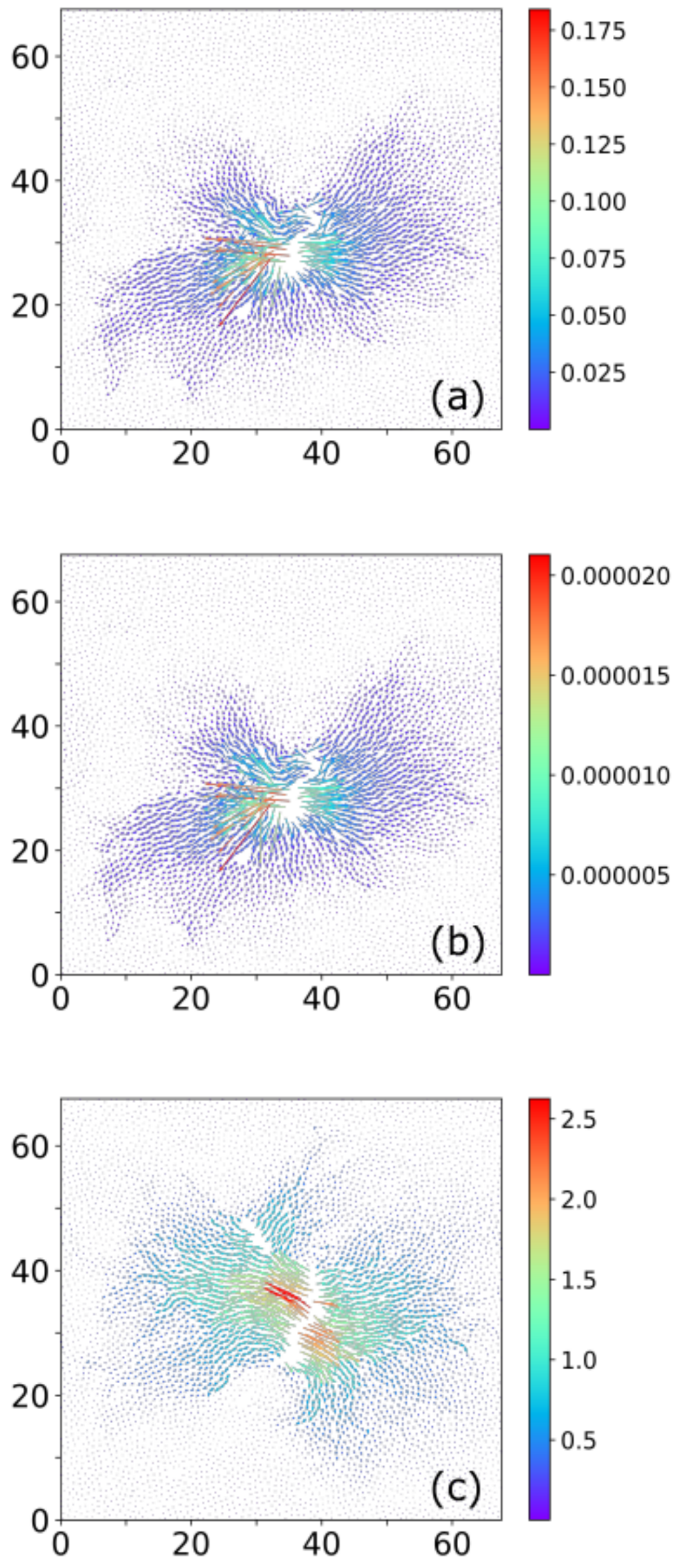

Figure 3.5. For the yielding avalanche: (a) Spatial map of the eigenvector on approach to the yielding pressure jump (b) Displacement fields on approach to the yielding pressure jump (c) Displacement fields across the yielding pressure jump.

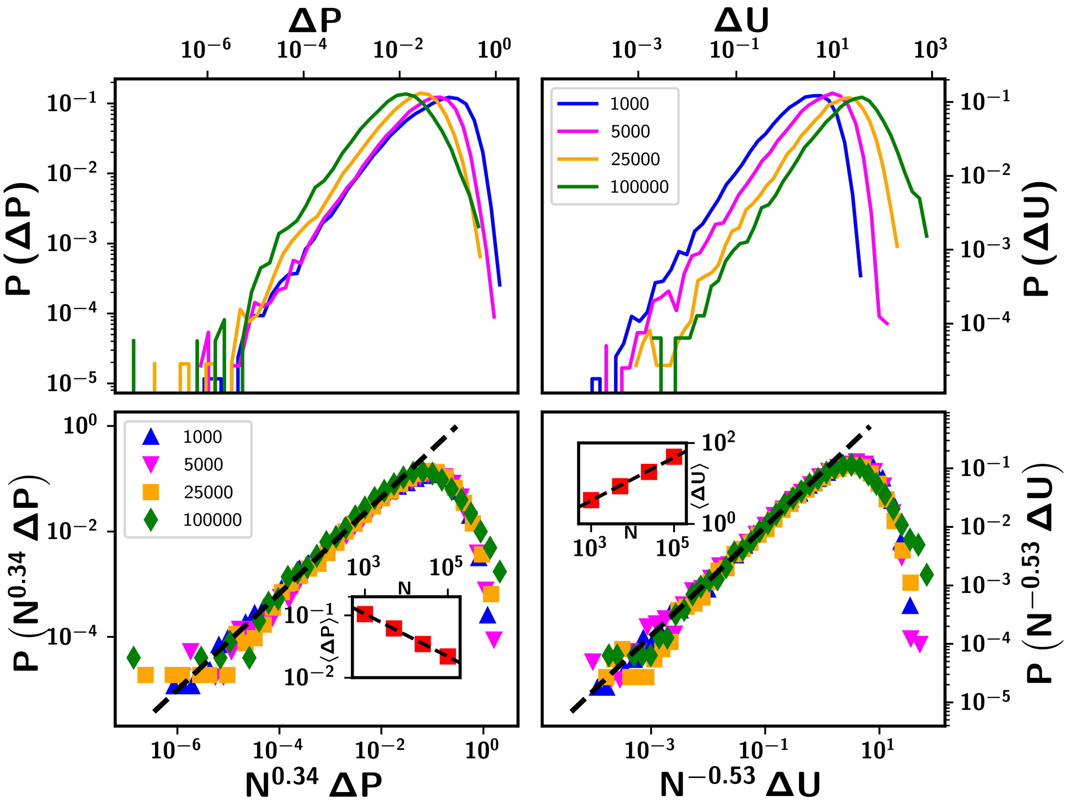

Figure 3.6. For different system-sizes: (a) Distributions of pressure jumps ΔP in the post-yield regime; (b) Distributions of energy drops ΔU in the post-yield regime; (c) Collapse of the pressure distributions on scaling the pressure drops with a factor $N^{0.53}$, the small-strain values of the pressure-distribution obey a power law, $P(\Delta P) \sim (\Delta P)^{0.91}$; (d) Collapse of the pressure distributions on scaling the pressure drops with a factor $N^{0.53}$, the small-strain values of the energy-distribution obey a power law, $P(\Delta U) \sim (\Delta U)^{0.93}$.

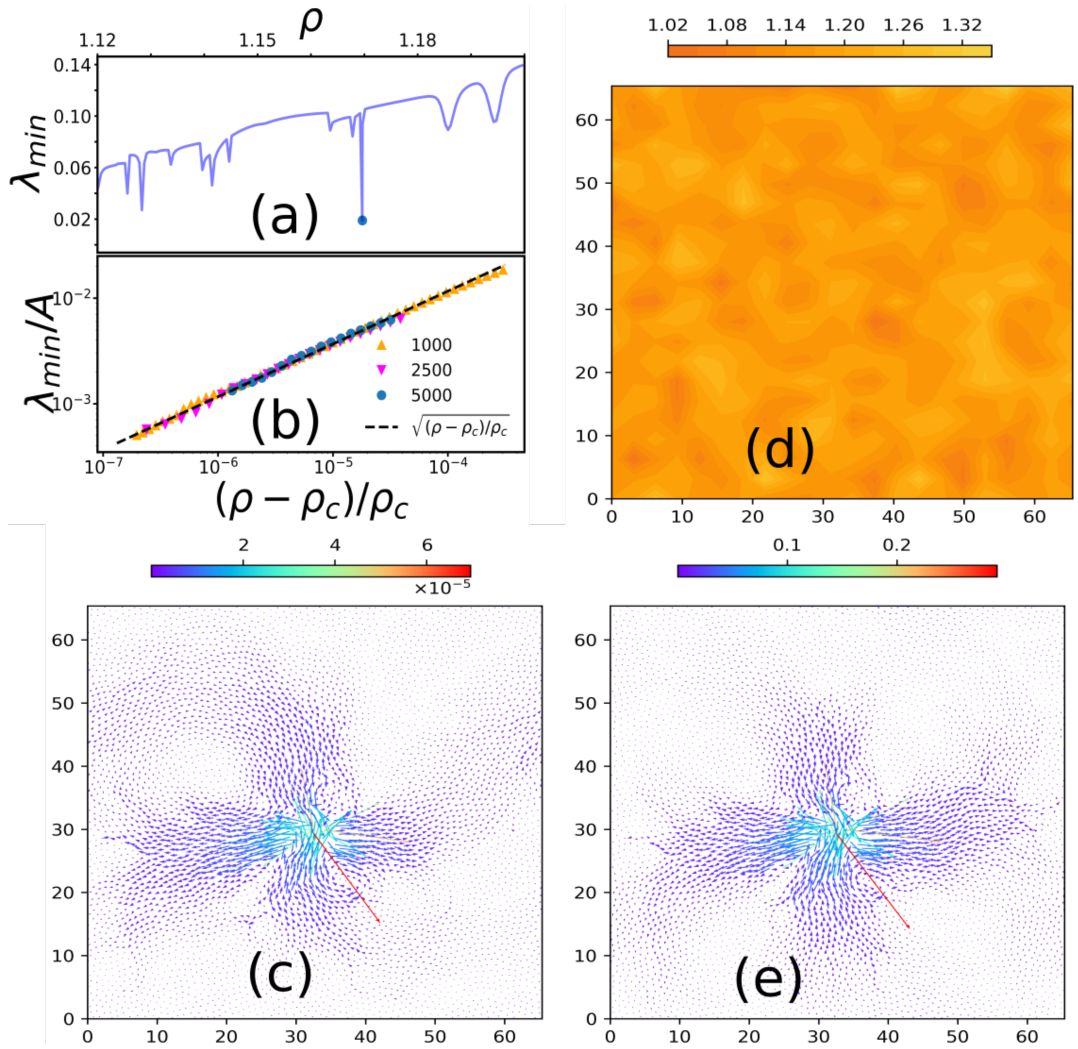

Figure 3.7. For the plastic events in the pre-yield branch of $P-\rho$: (a) The lowest non-zero eigenvalue of the Hessian of potential energy, λ_{min} as a function of density; (b) Vanishing of the eigenvalue as a square-root near a plastic event for different system sizes; (c) Eigenmode on approach to the plastic event; (d) Displacement field on approach to plastic event; (d) Coarse-grained density field of the solid after the event showing no density-inhomogenieties.

3.4.5 First plastic event & pre-yield plasticity

For amorphous solids under quasistatic shear deformation, even the elastic branch has been found to be substantially plastic [112, 113]. Similarly, a slight curvature in the pre-yield branch of pressure-density curves in Figure 3.1 under athermal quasistatic expansion suggests presence of some undetected plasticity. By tracking the lowest non-zero eigenvalue of the Hessian λ_{min}, we find that even in the pre-yield branch, λ_{min} goes to zero multiple times without a noticeable jump in pressure. We find that these instabilities occurs at a fairly large density, much before cavitation; see Figure 3.7(a). for a single trajectory of a $N = 5000$ system. By sampling such first plastic events from several trajectories, we show in Figure 3.7(b) that here too $\lambda_{min} \sim \sqrt{(\rho - \rho_c)/\rho_c}$, underlying that all the pre-yeild instabilities have a similar origin, viz, a saddle-node bifurcation in the underlying energy landscape. The spatial map of the eigenfunction at the brink of the first plastic instability illustrated in Figure 3.7(a) is shown in Figure 3.7(c). Again it matches well with the non-affine displacement undergone on the approach to the instability (see Figure 3.7(d)), a quadrupolar Eshelby-like shape [28, 114]. The presence of quadrupolar-like displacement fields suggest relaxation of frozen-in/residual stress in the initial state due to the increase in free volume [101] from expansion.

3.5 Summary

To summarise, we have studied how a spatially homogeneous amorphous solid responds to quasi-static isotropic expansion. As expected, the release of built-up internal stresses leads to yielding-like transition via cavitation, which then acts as precursor to eventual failure via system-spanning fracture. Both the yielding density as well as the location of complete fracture can be identified via susceptibility measurements. The system-size scaling of χ_p is exactly the same as that observed for applied shear. Our main focus is in examining the stability of the local minima that the system visits during the expansion process, by monitoring the smallest eigenvalue of the corresponding Hessian matrix. We demonstrate, using several model amorphous solids, both in $d = 2$ and 3, that whenever the eigenvalue goes through zero, all throughout the expansion trajectory, be it for the first event in the high density phase or around and after the yielding via cavitation, it vanishes as a square root singularity, which is characteristic of a saddle-node bifurcation within the underlying energy landscape. Thus, the point of yielding, where such instability was reported for a mono-component system [107], is nothing special vis-a-vis how the eigenvalue vanishes. Rather, these irreversible processes, which lead to non-affine displacements, seem universal characteristic to plastic events whenever an amorphous solid responds to large mechanical deformations, be it via shear or expansion. However, we note that unlike yielding via shear which can occur in amorphous materials of all kinds, cavitation has a thermodynamic underpinning vis-a-vis the existence of gas-solid coexistence in the phase diagram of attractive glass-formers.

4 Cavitation instabilities under secondary cyclic shear deformations

In this chapter, we explore the cyclic-shear response of spatially-homogenous states sampled from the trajectory of athermal quasistatic expansion. We find that, under cyclic shear, cavitation occurs at higher densities in these expanded states due to the lower energy barriers to cavitation under cyclic shear. The dependence of cavitation on the parameters, density (ρ) and amplitude of cyclic shear (γ_{max}) is marked in a two-parameter phase plane. In these expanded states, the cavitation occurs both below and above the thresholds for irreversible yielding under cyclic shear, provided there is ambient tension in the form of pressure being negative. We also observe that (i) spatial location of cavities in the expanded solid for different phase points in the $\gamma_{max} - \rho$ plane, starting from the same expansion trajectory, are not the same, and (ii) cavitation events occur via spatially-localised structures for smaller values of γ_{max} and via system-spanning avalanche-like structures for γ_{max} close to the yielding thresholds under cyclic shear, thus implying abundance and diversity of such cavitation modes in an expanded solid. To summarise, our work thus establishes how cavitation instabilities can arise more easily under coupling of cyclic-shear with uniform expansion also paves the way for future studies of coupling of multiple deformation modes.

4.1 Introduction

In the previous chapter, we have probed the elasto-plastic response of amorphous solids under athermal quasistatic expansion, and analyzed the cavitation instabilities that arise during this process. We have also found how occurrence of plasticity due to cavitation has many parallels with the plasticity under shear. The results suggest a unified picture of failure of amorphous solids on the energy landscape under various deformation protocols. The results also point to a possibility of cross-coupling between these deformation modes. Till now, much of the focus has been on shear response of dense glasses [28, 37, 115], where significant progress has been made to characterize the detailed elasto-plastic response of the material including development of mesoscale elasto-plastic models to understand yielding under shear on a mesoscopic length scale [2]. In most-practical scenarios, the loading process in a material certainly involves nearly all deformation paths like shear, volumetric expansion [68, 85, 86], uni-axial tension [69, 87] etc. instead of a single deformation mode which is the focus of most studies. And ramifications of these cross couplings can be detrimental to the stability of the materials under mechanical loading. Thus understanding the mechanical response under combinations of multiple deformations is also of great practical significance. Under uniform expansion discussed in Chapter 3, on the pathway to cavitation, in the pre-yield regime, we have also seen instances of shear-relaxation via eshelby-like quadrupolar events under expansion which suggests that these shear relaxation-like events precede cavitation. And thus, hinting a possibility of coupling of cavitation instabilities with shear deformation. In this work, we thus turn our attention to explore the response of an expanded amorphous solid to cyclic shear deformations.

4.2 Objective

The parallels between mechanisms of plasticity under expansion and shear (discussed in the previous chapter), shear-relaxation-like events in the elastic-branch under athermal quasistatic expansion, all point to the possibilities of cross-coupling of different deformation modes. Here, we systematically explore the response of an amorphous-solid under combination of expansion and cyclic-shear with aim to find out if such instabilities can arise early or at lower thresholds under combinations of such deformations

4.3 Model & Methods

4.3.1 Model

We use the well-characterized two-dimensional model binary Lennard-Jones mixture (KABLJ) which has been described in Chapter 2.

4.3.2 Initial state preparation

To prepare initial athermal amorphous states for our study, we first equilibriate the system at $T = 1.0$ (in LJ units), which is in the high temperature liquid regime, followed by cooling at a constant rate of $\dot{T} \approx 10^{-4}$ per MD timestep to $T = 0.01$, followed by a quench to $T = 0$ via conjugate gradient energy minimization.

4.3.3 Protocol for mechanical deformations

In Figure 4.1, we illustrate a schematic of the simulation protocol that we follow, in our study, for studying the mechanical response. An amorphous solid having attractive interactions is expanded under athermal quasistatic expansion (AQE), which acts as a primary deformation protocol (discussed in the previous chapter and below). A sample pressure (P) vs density (ρ) trajectory of expansion of such a solid is shown in the schematic diagram Figure 4.1 (in green). The secondary deformation protocol is then imposed on states generated along this P vs ρ trajectory. The secondary perturbation in the form of a quasistatic cyclic shear [116] (discussed below) having a certain strain amplitude (γ_{max}) which becomes a control parameter of our study along with the density ρ at which a configuration is sampled from the AQE trajectory. So thus, states sampled from different densities of AQE trajectory are subjected to AQCS.

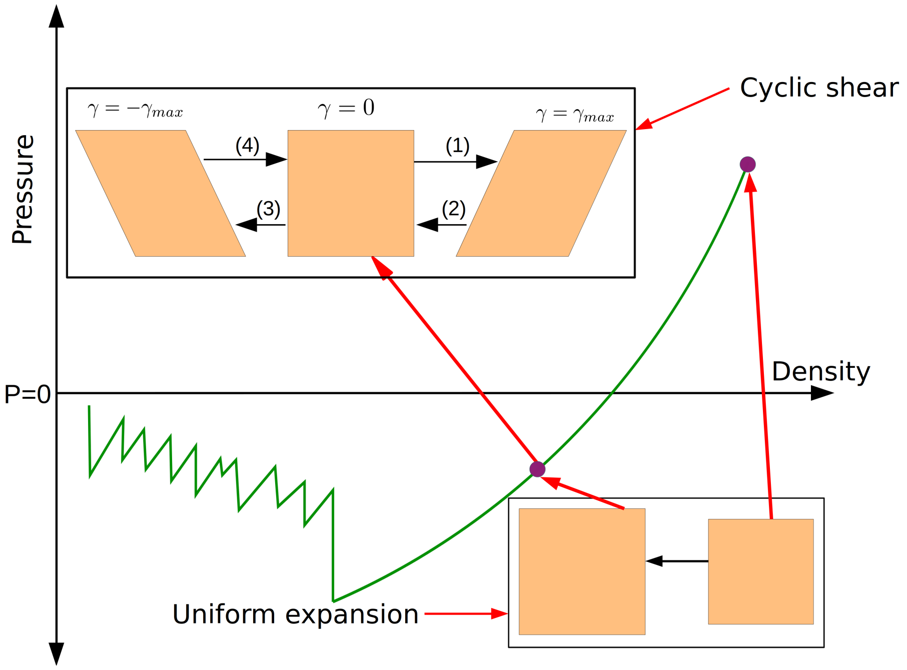

Figure 4.1. A schematic diagram of the protocol followed in our study: states generated during the expansion from a dense spatially homogeneous amorphous solid are subjected to secondary deformations in the form of a cyclic shear.

4.3.4 Athermal Quasistatic cyclic shear (AQCS)

In recent times, the response of amorphous solids to such a cyclic shear protocol has been studied in detail [43, 116] and has also bee described in 1.4.1.2. In this protocol, starting from states sampled from the trajectories of athermal quasistatic expansion, we apply in each step a shear strain of magnitude $\delta\gamma \approx 10^{-4}$ by deforming the simulation box and remapping the particle coordinates. The system is then allowed to relax via energy minimization using conjugate gradient (CG) algorithm. One cycle of AQCS consists of the following steps: (a) Driving of the system to a shear strain $\gamma = \gamma_{max}$ (b) Reversal of direction of applied shear strain upto a strain of $\gamma = -\gamma_{max}$ (c) Another reversal in direction of the applied strain until the strain reaches $\gamma = 0$. All the steps (a), (b) & (c) are performed in simulations using athermal quasistatic shear steps of magnitude $\delta\gamma$. Several such cycles are conducted and the response of the system is studied. The simulations are carried out using LAMMPS [109].

4.3.5 Coarse-grained density field and the phase diagram

To analyse the spatial features of the observed response, we construct a coarse-grained density field by using the method described in Ref. [117]. For the configuration whose density field is to be evaluated, we spatially discretize it using a square lattice, of lattice constant $a \approx 1$. In the neighbourhood of radius of $r = 1.5\sigma$ around each lattice point, we determine the local density. These local densities make up a rough density-field so we smoothen out the field using the following expression:

$$\tilde{\rho}_{i,j} = \frac{1}{6}(2 \cdot \rho_{i,j} + \rho_{i+1,j} + \rho_{i-1,j} + \rho_{i,j+1} + \rho_{i,j-1})$$

The $\tilde{\rho}_{i,j}$ is the resulting coarse-grained density field. A region of density $\rho < 0.5$ is considered as a cavity for marking the points in the phase diagram. The phase diagram was obtained using the 10 independent realizations and if at a given phase point, more than 50% of the samples cavitate within 200 cycles of cyclic shear, the point is marked as green.

4.3.6 Plasticity maps

To get spatial information about the extent of displacements at the local scale due to the imposed secondary deformation, we construct mobility maps. For each particle within the system, we compute the squared distance travelled upto time t (or cycle number) relative to the initial state ($t = 0$), i.e the time at which secondary deformation is imposed on a state sampled from the expansion trajectory,

$$\Delta_i^2(t) = \mid \vec{r}_i(t) - \vec{r}_i(0) \mid^2$$

The map is constructed by using the co-ordinates of the particles at $t = 0$ and coloring each one of them as per the magnitude of $\Delta_i^2(t)$.

4.4 Results

4.4.1 Early cavitation

We subject the spatially-homogeneous amorphous states from the trajectory of AQE to AQCS. As these expanded amorphous states from the region $P < 0$ are subject to cyclic-shear, we find that they cavitate as shown for an example trajectory in Figure 4.2(b) and 4.2(c) where the line segments connecting filled symbols mark the instances of pressure-jumps and energy-drops due to cavitation at an amplitude $\gamma_{max} = 0.06$. The variation of pressure (P) and energy (U/N) with cycles of cyclic shear, when cavitation occurs, is shown in the insets of Figure 4.2(b) and Figure 4.2(c) respectively. The feasibility of cavitation to occur depends intricately on the two control parameters, *viz.* the density at which the state is sampled from the AQE trajectory ρ and the amplitude of cyclic shear γ_{max}. We therefore summarise this parameter dependence in a two-parameter phase diagram in Figure 4.2(a), where the green color marks the region where cavitation is observed and the red

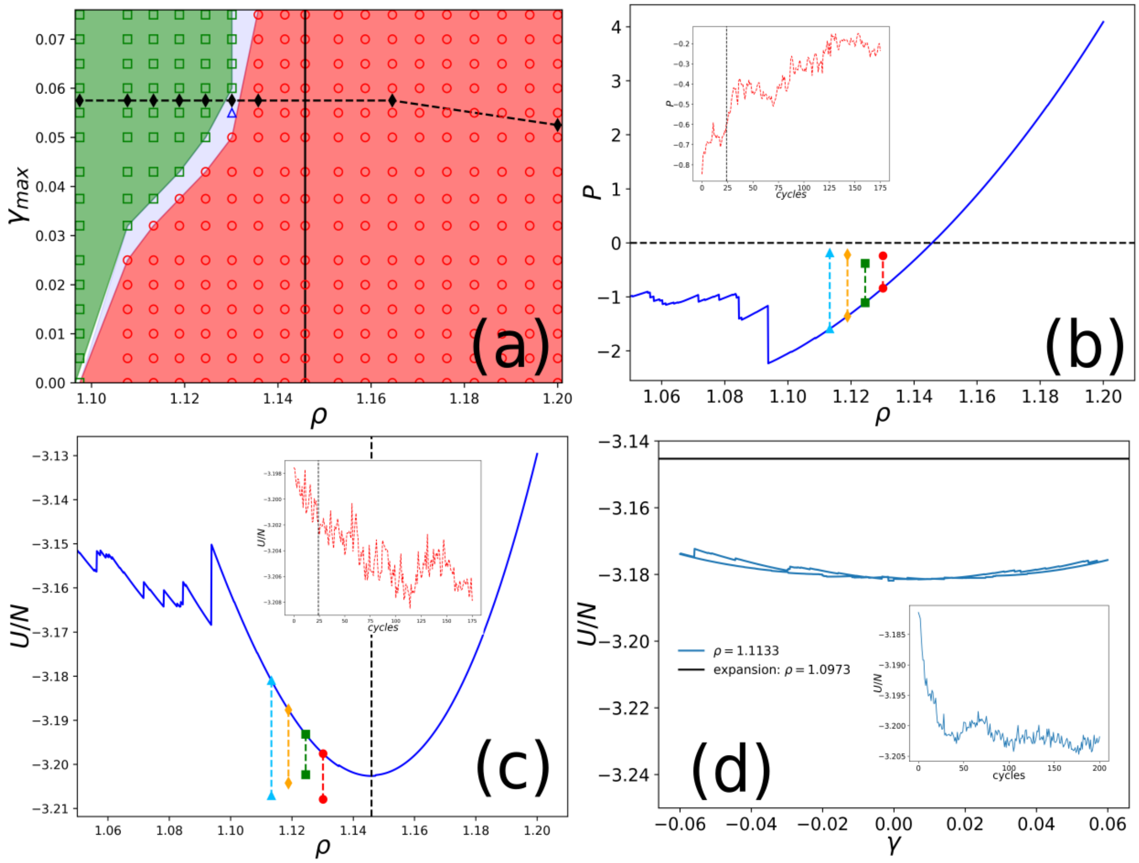

Figure 4.2. Early onset of cavitation: (a) Phase diagram showing the region where cavitation (marked in green) occurs under cyclic shear in the γ_{max}-ρ plane. (b) For $\gamma_{max} = 0.06$, pressure jumps corresponding to a cavitation under cyclic shear at higher densities marked on the uniform expansion trajectory in the pressure (P) vs density (ρ) plane. The inset shows the evolution of pressure with the cycles of cyclic shear (c) The energy drops corresponding to the pressure jumps in (b) are marked on the uniform expansion trajectory in the energy per particle (U/N) vs density (ρ) plane (d) Energy per particle (U/N) as a function of shear strain within the first cycle of cyclic shear. The black horizontal line on the top marks the energy at which cavitation occurs under expansion and the evolution of the energy per particle U/N with cycles is shown in the inset.

color denotes the region where cavitation is not observed. As shown in the Figure 4.2(a), for the higher amplitudes of cyclic shear (γ_{max}), the cavitation occurs at higher values of density and vice-versa. This is because higher amplitudes of cyclic shear pump in higher amounts of energy into the system, thus enabling the system to surmount the necessary energy barriers for cavitation to occur at higher densities. The vertical black line in the Figure 4.2(a) marks the zero pressure line under athermal quasistatic expansion (primary deformation) and it is to be noted that, the cavitation instabilities seem to occur only in the $P < 0$ region suggesting that internal tension is necessary for cavitation. To understand energy thresholds under cyclic shear, we look at the energies per particle (U/N) within the cycle of shear when cavitation occurs and compare it with the energies at which cavitation occurs under uniform expansion in Figure 4.2(d). We see that the energies accessed by cyclic shear within the first shear cycle (see blue curve in Figure 4.2(d)) are much lower than the energies at which cavitation occurs under expansion (black horizontal line in Figure 4.2(d)). Even for the subsequent cycles of the shear, the energy decreases further on the path to cavitation as shown in the inset of Figure 4.2(d) demonstrating annealing of the solid due to the formation of cavity. This implies that starting from expanded $P < 0$ state, it is easier (energetically-favourable) to cavitate the solid using cyclic shear than uniform expansion. Therefore, one can conclude that from the potential energy landscape picture, the barriers to cavitation for these expanded $P < 0$ states are much lower in the direction of cyclic shear than in the direction of uniform expansion.

4.4.2 Yielding, timescales & limit cycles

A pertinent question to ask is whether the cavitation induced by the secondary mechanical perturbation results in large scale plasticity due to yielding of the solid or not, as has been observed in dense glassy systems for similar cyclic shear protocol [43]. As already evidenced in Figure 4.2(d) for example trajectories, the energy decreases after cavitation, implying that the system is annealing after the cavity has appeared, which seems contrary to the yielding scenario. On the other hand, this prompts us to check across all accessed state points whether the system reaches an arrested state or not, via annealing.

We probe this by monitoring, across many cycles of the applied shear, the stroboscopically measured ensemble averaged normalized energy defined as $\langle |u - u_0|/|u_0| \rangle$, where u_0 is the energy at the start of first cycle. A typical scenario, at an example density ($\rho = 1.1133$), is shown in Figure 4.3(a) & Figure 4.4. When the cyclic shear is imposed, the energy of the system starts to decrease with cycles. For the right combinations of densities and amplitudes as summarised in the phase diagram, this decrease of energy is accompanied

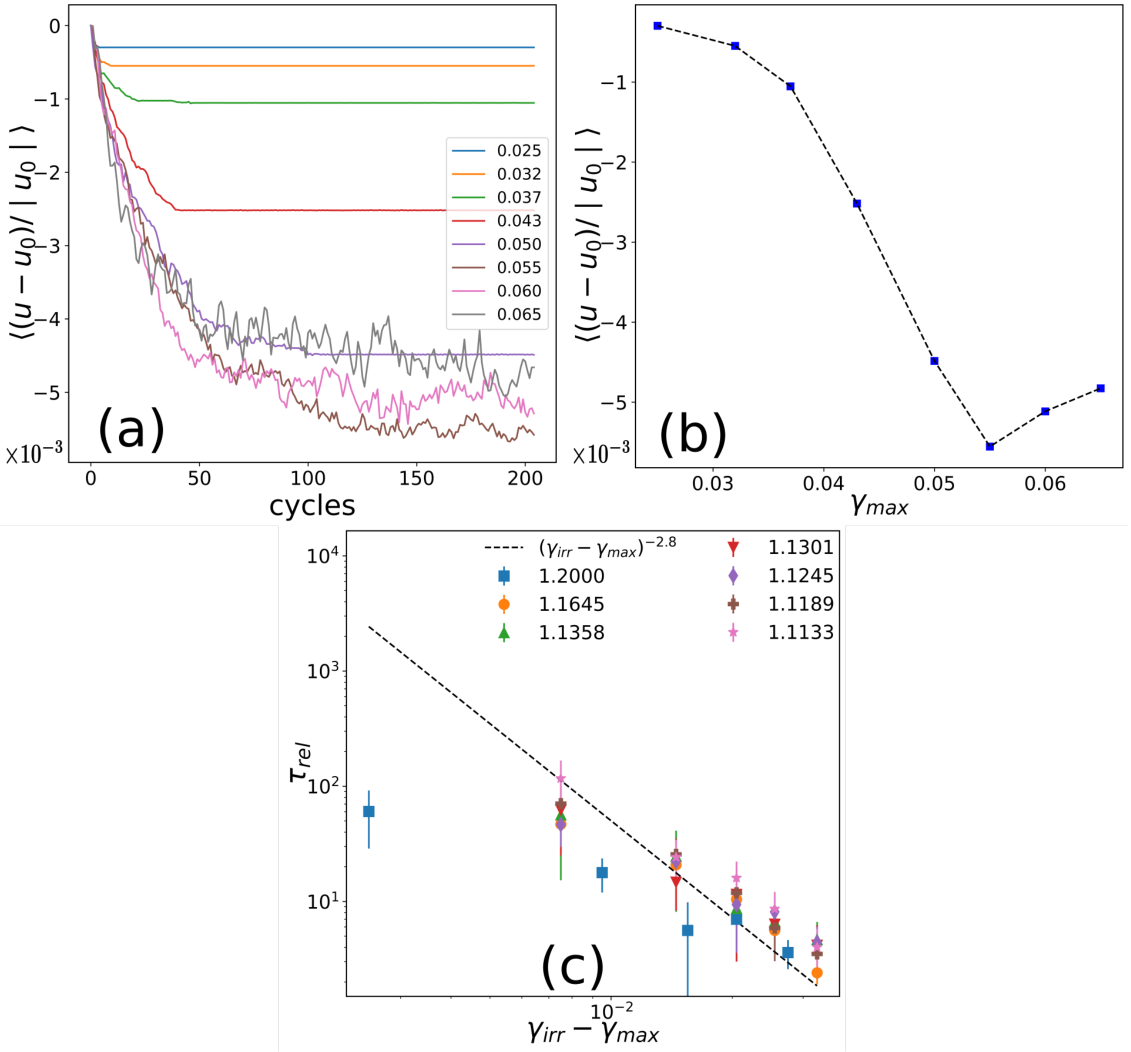

Figure 4.3. (a) Stroboscopic evolution of scaled energy (defined in the text) with cycles of cyclic shear (b) Mean values of scaled energy in last 20 cycles of (a) for different amplitudes of cyclic shear (c) Number of cycles required to reach a steady state τ_{rel} or a limit cycle as a function of amplitude of cyclic shear(γ_{max}) for different densities.

by formation of a cavity. The decrease could happen due to lack of initial annealing, as previously reported in studies involving high density glassy systems [44]. And/or, it can be due to the formation of a cavity. The normalized energy after a certain number of cycles either reaches a absorbing state/limit cycle (discussed in the next paragraph) or it diffuses around an average value (also seen in [43, 118–120]). The averaged value in the steady state or the last 20 cycles in the diffusive state are plotted for different amplitudes in the Figure 4.3(b). The cusp in the curve marks the yielding point under cyclic shear [44]. The yield points under cyclic shear for different densities are also marked in Figure 4.2(a) with diamonds connected by a dotted black line. The yield thresholds across different densities remains more or less constant within the range of amplitudes studied except for the initial state of athermal quasistatic expansion. This perhaps occurs because some shear-relaxation in the elastic branch (discussed in the previous chapter) of expansion which ends up stabilizing the solid. It needs to be noted that the the shape of the curve in Figure 4.3(b) depends on the annealing of the initial state, for very well stabilised glasses, the annealing in the regime $\gamma < \gamma_{max}$ is absent [44, 90]. A similar study using well-annealed glasses is an ongoing work beyond the scope of this thesis.

In the previous studies on cyclic shear at higher densities, it was observed that the timescale to reach a limit cycle or absorbing state diverges as the threshold of the reversible-irreversible transition (in terms of straining amplitude) is approached [118, 120]. We have measured this timescale (τ_{rel}) and in in the Figure 4.3(c), it is plotted as a function of the difference between driving amplitude (γ_{max}) and the yield amplitude γ_{irr}, where γ_{irr} is the yield amplitude obtained from the location of the cusp in the annealing data, as seen in Figure 4.3(b). The power law reported for cyclic shear of high-density solids [118, 120] with an exponent -2.8 here too, serves as a good guide to the eye. The exponent values have been reported to be between -2.5 [118] and -2.7 [120]. To accurately determine the exponent, γ_{irr} has to be determined with sufficient precision for all the densities as evident from the data at lower values of $(\gamma_{irr} - \gamma_{max})$. Determining this exponent accurately is a computationally intensive task as one needs to average over a large number of ensembles to determine the yield amplitude and thus it is beyond the scope of our thesis.

For smaller amplitudes of driving under cyclic shear, the high-density solid has been observed to reach an absorbing state or a limit cycle wherein the system alternates between a certain number of states [19, 118, 119]. The number of states that a system alternates between, defines the period of limit cycle. These limit cycles are an example of return point memory in amorphous solids [121]. We observe similar trend as shown in the Figure 4.3(a) & Figure 4.4. As evident from the Figure 4.3(a), for smaller amplitudes, the solid usually reaches an absorbing state under cyclic shear but for a few rare cases, a limit cycle of period 2 is observed as shown in the stroboscopic plots and within-cycle plots in the Figure 4.5(a) & Figure 4.5(b) respectively.

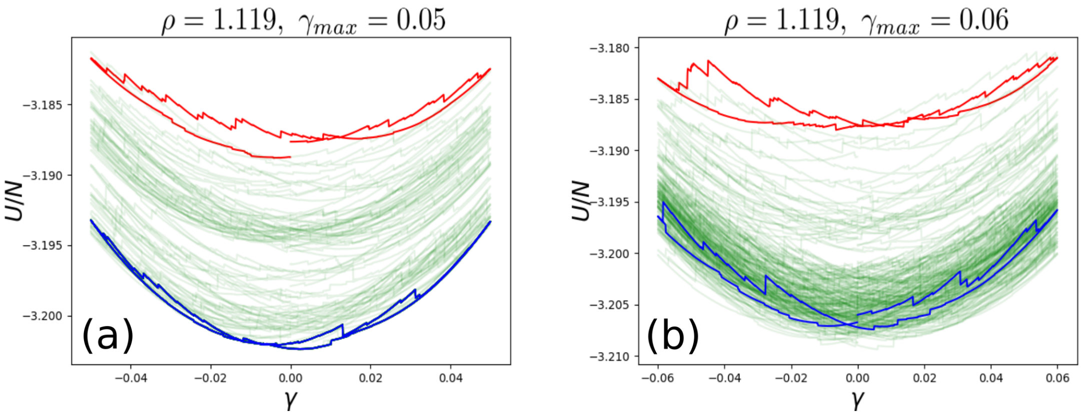

Figure 4.4. Evolution of energy per particle (U/N) within the shear cycles for : (a) a case where the system reaches an absorbing state; (b) a case where the energy per particle remain diffusive. The red curve in both the figures marks the first cycle of cyclic shear, the blue curve marks the 200^{th} cycle and the green curves show the intermediate cycles.

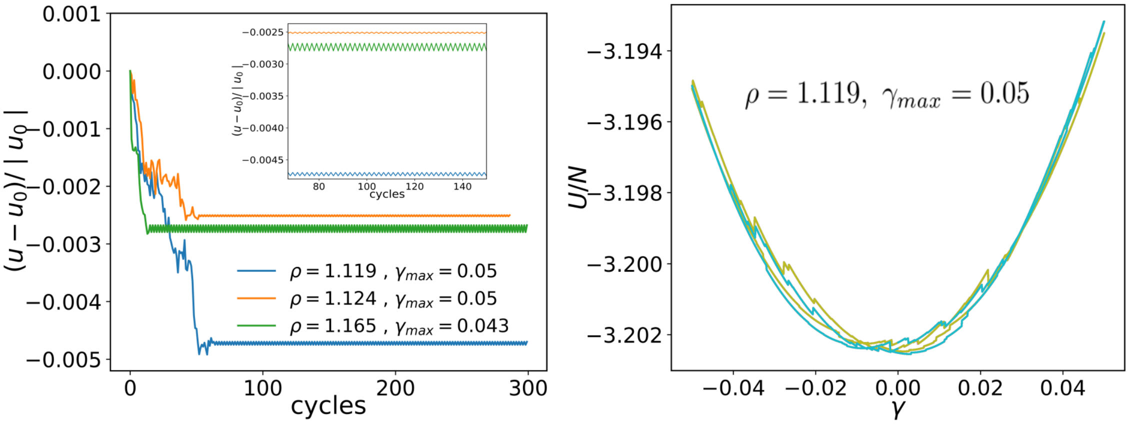

Figure 4.5. Demonstration of observed limit cycles of period two: (a) Stroboscopic evolution of re-scaled energies with cycles of cyclic shear; (b) Energy per particle (U/N) within the cycle as a function of shear strain; (γ) for one of the cases showing the two curves between which the system alternates.

4.4.3 Spatial ramifications

Finally, we examine the spatial structures emerging via cavitation induced by cyclic shear. We construct maps of the coarse-grained density field [117] (discussed in the methods

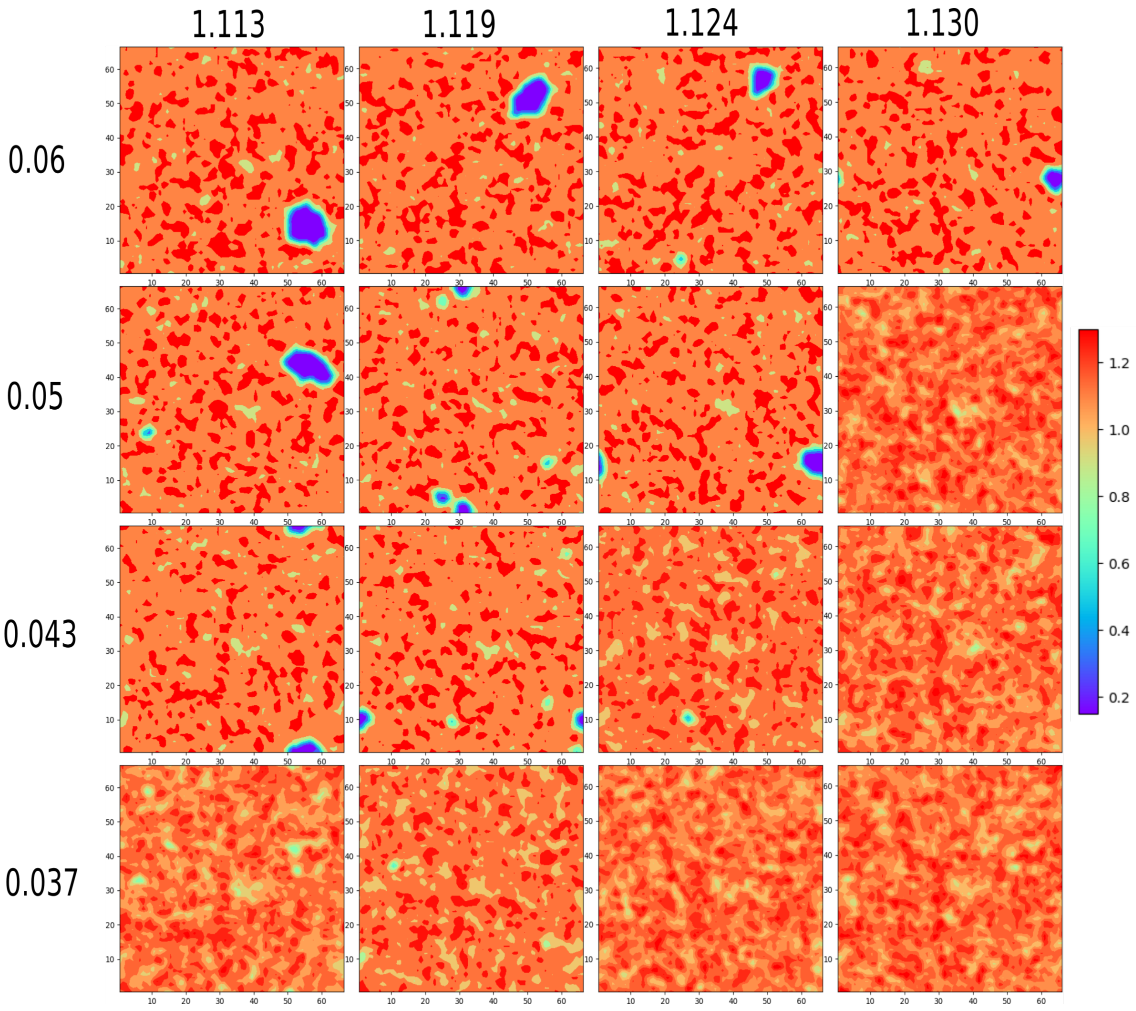

Figure 4.6. Coarse-grained density fields at different points in the phase diagram (Figure 4.2 (a)), starting from different densities of the same expansion trajectory.

section). In Figure 4.6, we show these density maps, after cavitation has occurred under cyclic shear, for different values of amplitudes and different values of densities, sampling initial states from the same quasistatic expansion trajectory at different densities. The topmost row corresponding to the driving amplitude $\gamma_{max} = 0.06$ shows the snapshots of the cavitation events under cyclic shear marked in the Figure 4.2(b) & (c). The location of cavity in the solid is different at different points in the phase diagram (see Figure 4.2(a)). For a given density, despite the same starting state for cyclic shear, depending upon the amplitude of cyclic shear (γ_{max}), the location of the cavity can be different. This suggests abundance of potential cavitation sites present throughout the solid. From the point of view of potential energy landscape, one can also conclude existence of multiple possible

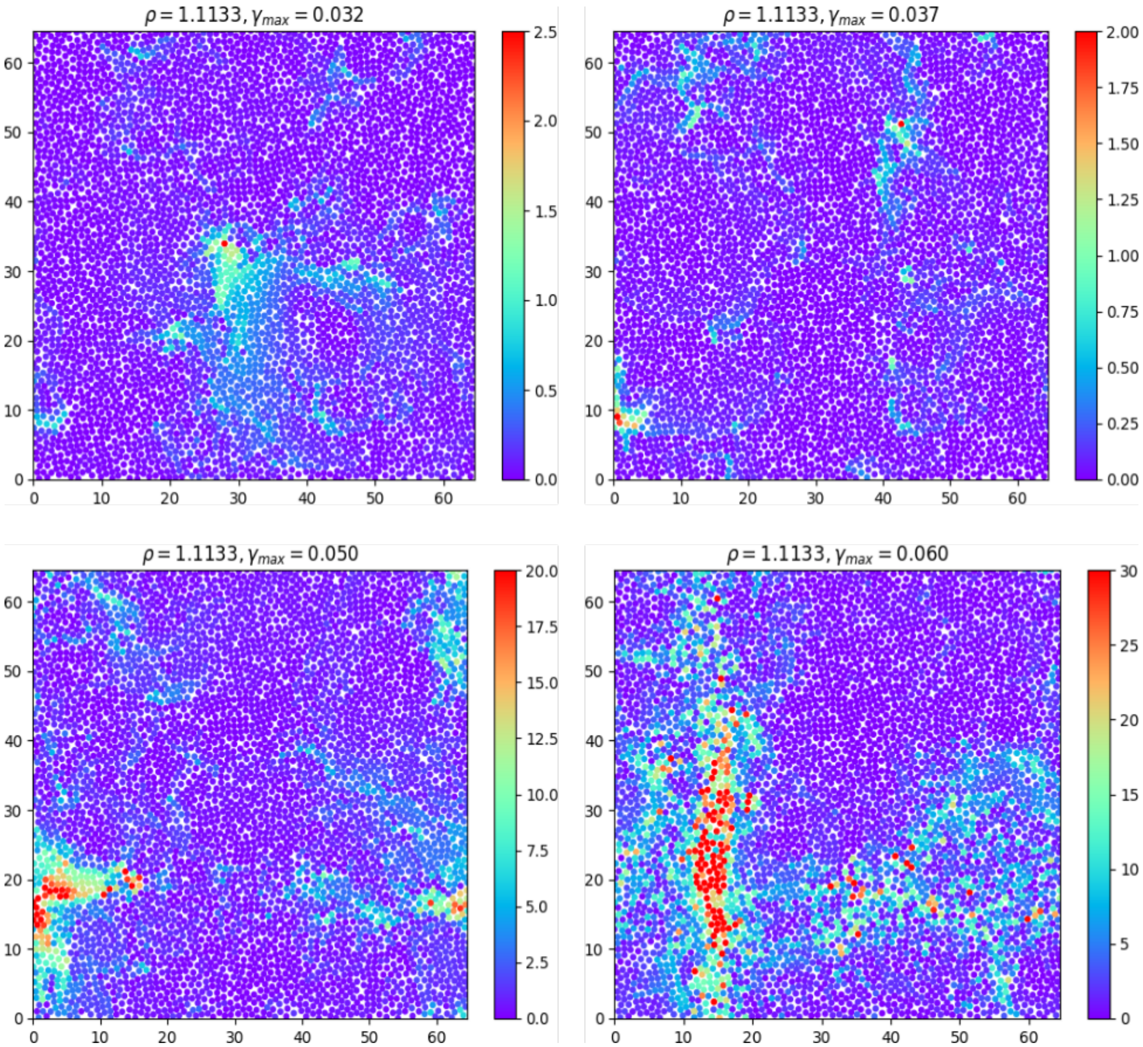

Figure 4.7. Amplitude dependence of plasticity maps at a given density

pathways on the energy landscape for the cavitation to occur from any given point on the energy landscape in the $P < 0$ region. The matrix of snapshots of cavitation also reflects the shape of the cavitation region in the phase diagram (Figure 4.2(a)) as one would expect.

Further, to characterize the extent of deformation undergone between the spatially homogeneous state sampled from the expansion trajectory and the cavitated state under cyclic shear, we make spatial maps of squared displacements (See Methods). In Figure 4.7, we show the squared displacement maps for a low density solid for different straining amplitudes. For smaller values of γ_{max}, the squared displacements are fairly localised in space, despite forming a cavity whereas for large γ_{max}, we see extended spatial structures formed by the regions undergoing large displacements. These structure are more localised around the location cavity. Thus, as γ_{irr} is approached, the spatial scale of plasticity gets more expanded and one expects these to observe system-spanning avalanche-like structures around yield. Thus, both spatially localised and spatially extensive pathways to cavitation are possible in $P < 0$ states.

4.5 Summary & Discussion

In summary, using numerical simulations, we have provided a demonstration that in comparison to a case of pure axial expansion, cavitation can occur at smaller densities when the amorphous solid, expanded from a high density state, is subjected to secondary mechanical deformation; the key requirement is the existence of an ambient tension (i.e. $P < 0$). We have shown this phenomenon for two examples of secondary deformation, viz. cyclic shear and active dynamics (not discussed here but reported in a same manuscript) [122]. Our work marks qualitative boundaries in the parameter space of density (or volume strains) and maximum shear strain (γ_{max}) where one would observe cavitation, thereby highlighting the possibility of early failure in amorphous solids under combinations of loading due to lower energy barriers to cavitation. These insights are also important from the point of view of designing stronger amorphous solids. We have also shown how such an expanded solid has abundant pathways to cavitation and such cavitation can proceed via both, localised and avalanche-like means. The failure in amorphous solids is known to also depend on the geometries of loading as shown in recent works [69, 87]. In this context, our work makes it clear that cavitation occurs only in presence of an axial tension. The loading geometries employed in most numerical studies of shear deformation of amorphous solids, do not allow changes in density and hence do not observe cavitation under shear.

In recent times, significant progress has been made towards the development of simple meso-scale models that use coarse-grained variables like stress and strain to provide insight into the physical processes during mechanical loading in amorphous solids. Not only have these models been successful in reproducing the phenomenology [27] but also have been able to bridge towards microscopic models [123]. However, most of the modelling has so far focused on the response to applied shear and that too in the dense limit where systems are spatially homogeneous. Our work on the coupling of various deformation modes and its consequence to failure via cavitation should now motivate further development of these models towards more complex loading scenarios.

Even though our work has marked a cavitation region, the precise boundaries are expected to depend on annealing of the initial state used for athermal quasisitatic expansion and on system sizes used in numerical simulations. Further light will be shed on these aspects in future studies.

5 Effect of pinning on cavitation in amorphous solids

In this chapter, we explore the elasto-plastic response of an amorphous solid under athermal quasistatic expansion with a small fraction of its particles pinned. These pinned sites present a minimal model of micro-alloyed inclusions, that are typically embedded for building a tougher glass. We find that, even in presence of a very small concentration of pinned particles, cavitation becomes more spatially homogeneous and the location of cavitation instability shifts to lower densities and lower pressures, implying a higher load-bearing capacity of the pinned solid. The sharp brittle-yielding-like transition seen in solids without such inclusions becomes more rounded with drastically smaller avalanche-sizes and exhibits little to no system size dependence. On tracking the eigenvalues of the Hessian near these instabilities, we find that cavitation occurs via a saddle-node bifurcation on the potential energy landscape and the average spatial decay of displacements in the plastic eigenmodes from the plastic center reveal a length-scale in pinned solids that parallels the length-scale set by average distance between two pinned sites. The presence of a length-scale explains the absence of system-size effects and the drastic decrease in the mean avalanche-sizes. Our findings thus reveal how micro-alloyed inclusions can suppress the cavitation and how the presence of a length-scale of plasticity controls the deformation response of such a pinned solid.

5.1 Introduction

The role of cavitation instabilities in fracture of amorphous solids has been discussed extensively in the previous chapters. Also, we have explored the elasto-plastic response of an amorphous solids to uniform expansion & the combinations of various deformations that lead to cavitation instabilities. These results suggest that in a natural deformation process in which various forms of deformations will be coupled together, the material can show unpredictable failure behavior, which will be difficult to control. Thus, a systematic study of how such a cavitation-dominated failure process in an amorphous solid is of great interest from the point of view of making stronger glasses. For making glasses with higher fracture-toughness, the seeding of the amorphous solids with micro-alloyed inclusions has gained a lot of popularity in the last few years [108, 124–128]. In the numerical simulations, a minimal-model of these micro-alloyed inclusions describes these inclusions as pinned/frozen particles that only move affinely; during the relaxation these pinned particles are not allowed to move. In this context, systematic studies investigating the response of a pinned amorphous solid to a shear-deformation have explored the microscopic theories [126], yielding mechanisms [108], suppression of shear-banding [127], development of length-scales [108, 128] etc. The yielding transition under shear is significantly smoothed under pinning of a small fraction of particle but in scenarios where fracture occurs via cavitation, it still remains to be understood how pinning a small fraction of particles affects the fracture via cavitation. To bridge this gap, in this work, we examine, the response of a pinned amorphous solid under uniform athermal quasistatic expansion.

5.2 Objective

Recently, in the context of creating stronger amorphous solids, the idea of micro-alloying via inclusions has gained significant popularity. Typically, in numerical modeling, inclusions have been considered as pinned/frozen particles within the amorphous solid. Here we systematically explore the response of a pinned amorphous solid to athermal quasistatic expansion and study its effect on cavitation instabiltiies.

5.3 Model & Methods

5.3.1 Model

We use the well-characterized two-dimensional model binary Lennard-Jones mixture (KABLJ) which has been described in Chapter 2.

5.3.2 Preparation of initial states

To prepare initial states for our study, we first equilibriate the system at $T = 1.0$ (in LJ units), which is in the liquid regime, followed by cooling at a constant rate of 10^{-4} per MD timestep to a final temperature of $T = 0.01$ [108], which is in the glassy regime. The corresponding glass transition temperature of the model system is at $T = 0.44$ [97]. The athermal states used in our study are generated by obtaining inherent structure states corresponding to the glassy configurations at $T = 0.01$, via conjugate gradient (CG) minimization [103].

5.3.3 Deformation protocol

We use the same deformation protocol as discussed in Chapter 3. Starting from a spatially homogeneous high density state ($\rho = 1.2$ for KABLJ), we study the athermal quasi-static response. In each expansion step, a volume strain is applied on the system by re-scaling the length of the box by a factor $(1+\epsilon)$ along with affine transformation of particle coordinates, followed by minimization of the energy of this strained configuration using the conjugate gradient algorithm [103]. The values of ϵ are varied from $\epsilon = 10^{-4}$ to $\epsilon = 10^{-9}$. The AQE simulations are done using LAMMPS [109].

5.3.4 The pinning construction

We choose a small fraction of particles $c = 0.01$ to $c = 0.05$ in the generated solid and freeze their motion. The particles are chosen randomly as long as no two pinned particles lie within the cut off of the interaction between them [108]. This helps avoiding the scenario where two close-by pinned sites increase the energy of the system. The pinned particles only move affinely when the strain is applied. During the energy minimization, these pinned particles are not allowed to move.

5.3.5 Hessian of potential energy for systems with pinning

LAPACKE [104] is used for doing the stability analysis of the local minima states, by computing eigenvalues and eigenvectors of the Hessian matrix $\mathcal{H}_{ij}^{\alpha\beta}$, which is defined as

$$\mathcal{H}_{ij}^{\alpha\beta} = \frac{\partial^2 U\left(\{\mathbf{r}_i\}\right)}{\partial r_i^{\alpha} \partial r_j^{\beta}}, \tag{5.3.1}$$

Consider a system of N particles, where particle numbers, $i = 1, \cdots, m$ are free and particle numbers $i = m+1, \cdots, N$ are pinned. The potential energy of the system can be written as

$$U(r) = \frac{1}{2}\left[\sum_{i,j=1;i\neq j}^{m} \phi_{ij} + 2\cdot\sum_{i=1}^{m}\sum_{j=m+1}^{N}\phi_{ij}\right] \tag{5.3.2}$$

The first term comes from the interactions between unpinned particles, the second term comes due to the interactions between the pinned and the unpinned particles. Note that the term due to interactions between pinned sites is set to zero because of our pinning protocol

By substituting the equation (5.3.2) in equation (5.3.1) , it can be shown that the first term in the sum of equation (5.3.2) gives a contribution,

$$H^{ij}_{\alpha\beta} = -\sum_{k,i;k\neq i}\left[\left(\frac{\phi_r}{(r^{ik})^3} - \frac{\phi_{rr}}{(r^{ki})^2}\right) r^{ki}_{\alpha} r^{ki}_{\beta} - \delta_{\alpha\beta}\frac{\phi_r}{r^{ki}}\right](\delta^{ji} - \delta^{jk}) \tag{5.3.3}$$

the second term of the sum in equation (5.3.2) gives,

$$H^{ij}_{\alpha\beta} = -2\sum_{k=0}^{m}\sum_{l=m+1}^{N}\left[\frac{\phi_r\, r^{kl}_{\alpha}\, r^{kl}_{\beta}}{(r^{kl})^3} - \frac{\phi_{rr}\, r^{kl}_{\alpha}\, r^{kl}_{\beta}}{(r^{kl})^2} - \delta_{\alpha\beta}\frac{\phi_r}{r^{kl}}\right]\delta^{ij} \tag{5.3.4}$$

ϕ_r and ϕ_{rr} are first and second derivatives of the pair-potential respectively

5.4 Results

5.4.1 Yielding and spatial ramifications

Upon expanding the amorphous solid isotropically under quasistatic loading, as discussed in previous works [85, 129] , the pressure of the solid decreases and reaches negative values. After a certain threshold, a sharp jump in the pressure accompanies cavitation of the solid. Upon further expansion, the cavities grow and merge leading to system-spanning fracture of the solid [129]. We expand the same amorphous solid isotropically but with a small fraction of particles pinned (frozen) and compare it with the case without pinning [85, 129]. As shown in Figure. 5.1(a), compared to the unpinned solid, the pinned solid on average, does not show a large pressure jump that is seen around the first cavitation event. The location of the yield point which is usually marked by a turn in the pressure-density curves, shifts to lower and lower densities with increasing c, demonstrating an increase in load-bearing capacity of pinned solids. In the pinned solids ($c \neq 0$), the turning of the curve occurs due to small pressure jumps that occur gradually, leading to a smooth curve in the ensemble-averaged pressure P vs density ρ planes as opposed to the ensemble-averaged trajectories of an unpinned solid ($c = 0.00$), which show an abrupt jump. A similar trend reflects in the energy per particle (U/N) vs density (ρ) plots in Figure. 5.1(b) i.e. no large energy drop shows up in the pinned solid unlike the case of unpinned solid and in fact, the energy per particle of the pinned solid keeps increasing with increasing pinning concentration. The fluctuations of pressure and energy at a given value of density across ensembles are characterized by susceptibilities [129], $\chi_p(\rho) = N\left(\langle P^2(\rho)\rangle - \langle P(\rho)\rangle^2\right)$ and $\chi_u(\rho) = (1/N)\left(\langle U^2(\rho)\rangle - \langle U(\rho)\rangle^2\right)$ shown in Figure. 5.1(c) & (d) respectively. A sharp susceptibility peak around the big pressure jump / energy drop seen in the unpinned solid [129] is tamed down due to pinning. For higher pinning concentrations, a clear peak around the yielding is not seen implying that the yielding of the solid is more localised and gradual. The gradual nature of cavitation in pinned solids is also echoed in the average size of pressure jumps $\langle \Delta P\rangle$ and energy drops $\langle \Delta U\rangle$ encountered during expansion (see 5.1(e) & (f)) for different pinning concentrations c. The average size of avalanches, $\langle \Delta P\rangle$ & $\langle \Delta U\rangle$ decreases drastically with increasing values of c implying suppression of large pressure jumps and energy drops.

To probe the spatial-nature of cavitation in pinned solids, we look at the coarse-grained spatial density maps for different values of c at a same value of density (shown in Figure.5.2). They suggest that the cavitation occurs at multiple sites in the solid gradually over the course of expansion for $c \neq 0$ instead of a heterogeneous cavitation starting with a big cavity for $c = 0$. The creation of a large number of cavities in the system also explains the increase in energy with expansion seen in Figure 5.1(b) as presence of a large number of particles on the surfaces is expected to increase the energy of pinned solids. So, to summarise, pinning smooths out the sharp yielding-like cavitation transition seen in amorphous solids and causes less heterogeneous cavitation. This scenario is consistent with a previous study on effect of pinning on yielding transition under simple shear [108] where pinning made the yielding more spatially homogeneous.

5.4.2 System-size effects

In our previous work decribed in Chapter 1. [129], we had encountered significant system size effects in the pressure (P) vs density (ρ) curves & the susceptibilities χ_p for athermal quasistatic expansion of amorphous solid, hence we probe the dependence on system sizes for pinned solids here. The pressure (P) vs density (ρ) plots and χ_p vs density ρ plots for different system sizes across the pinning concentrations studied, are reported in the Figure 5.3 left panels and right panels respectively. Unlike the case of unpinned solids, the $P - \rho$ and $\chi_p - \rho$ curves for pinned solids show little to no dependence on the system-size. This occurs due to presence of a length scale of plasticity $\xi << L$ which is discussed in the next few sections.

5.4.3 Irreversible plastic events on the potential energy landscape

Under athermal quasistatic shear, near a plastic instability, the lowest non-zero eigenvalue (apart from the two zero-modes in 2D) of the hessian of the potential energy eq. 5.3.1, is known to vanish as a square root of strain difference from the point of instability [17,28]. i.e. $\lambda_{min} \sim \sqrt{\gamma_c - \gamma}$. This occurs due to a saddle node bifurcation on the the potential energy landscape where the local minima in which the system resides in, becomes unstable in one direction. One of the possible ways to arrive at such a square-root power law has been discussed in Ref [35], where it has been shown that how the nature of non-affine displacements in amorphous solids near a plastic instability with only $\lambda_{min} \to 0$ gives rise

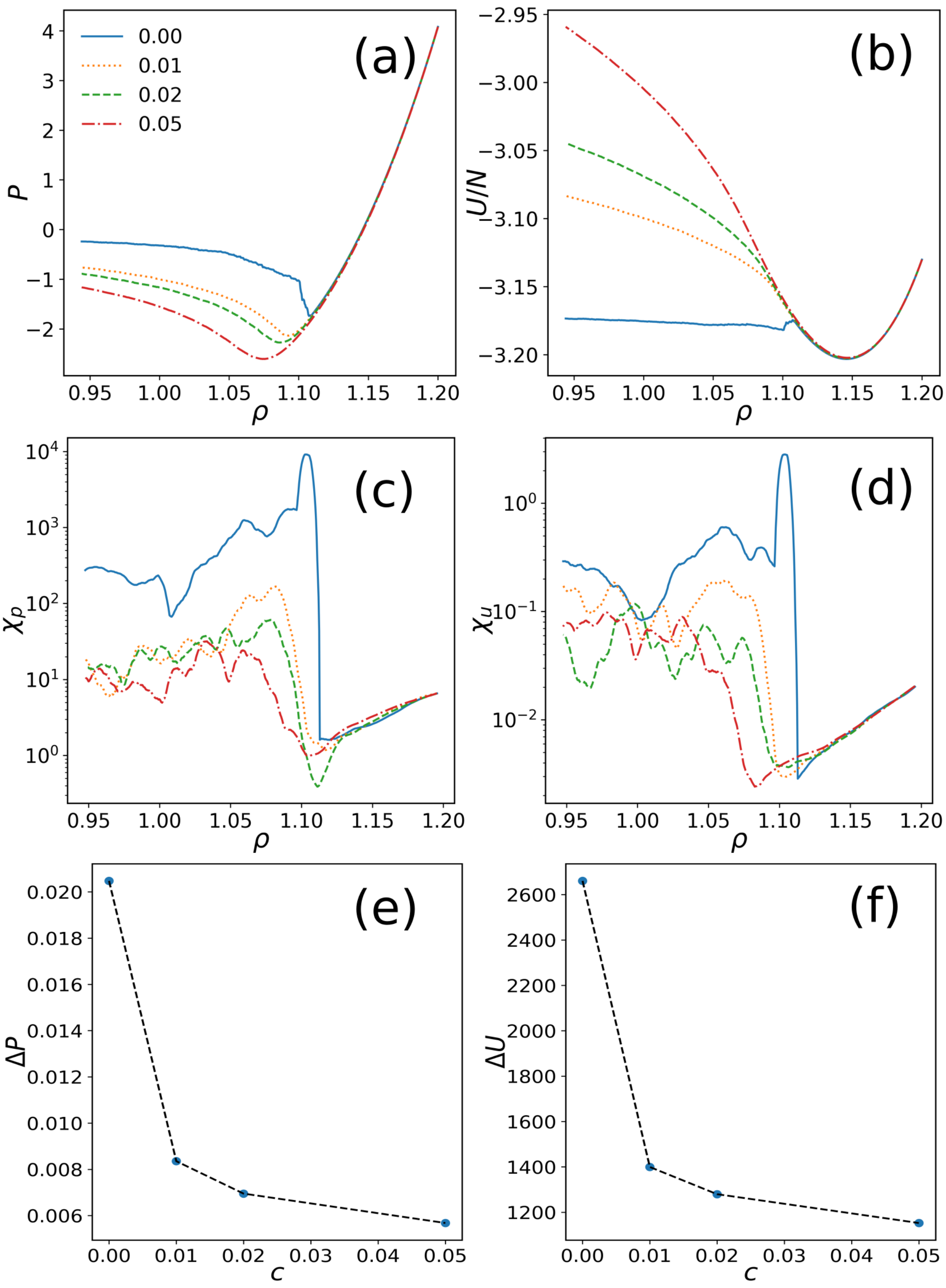

Figure 5.1. For $N = 10^5$ and different pinning concentrations, c, as marked: Variation with density ρ of (a) Pressure P (b) Energy per particle U/N (c) Pressure susceptibility χ_P (d) Energy susceptibility χ_U. Change in (e) average size of pressure jump ΔP, and (f) average size of energy drops ΔU, with pinning concentration.

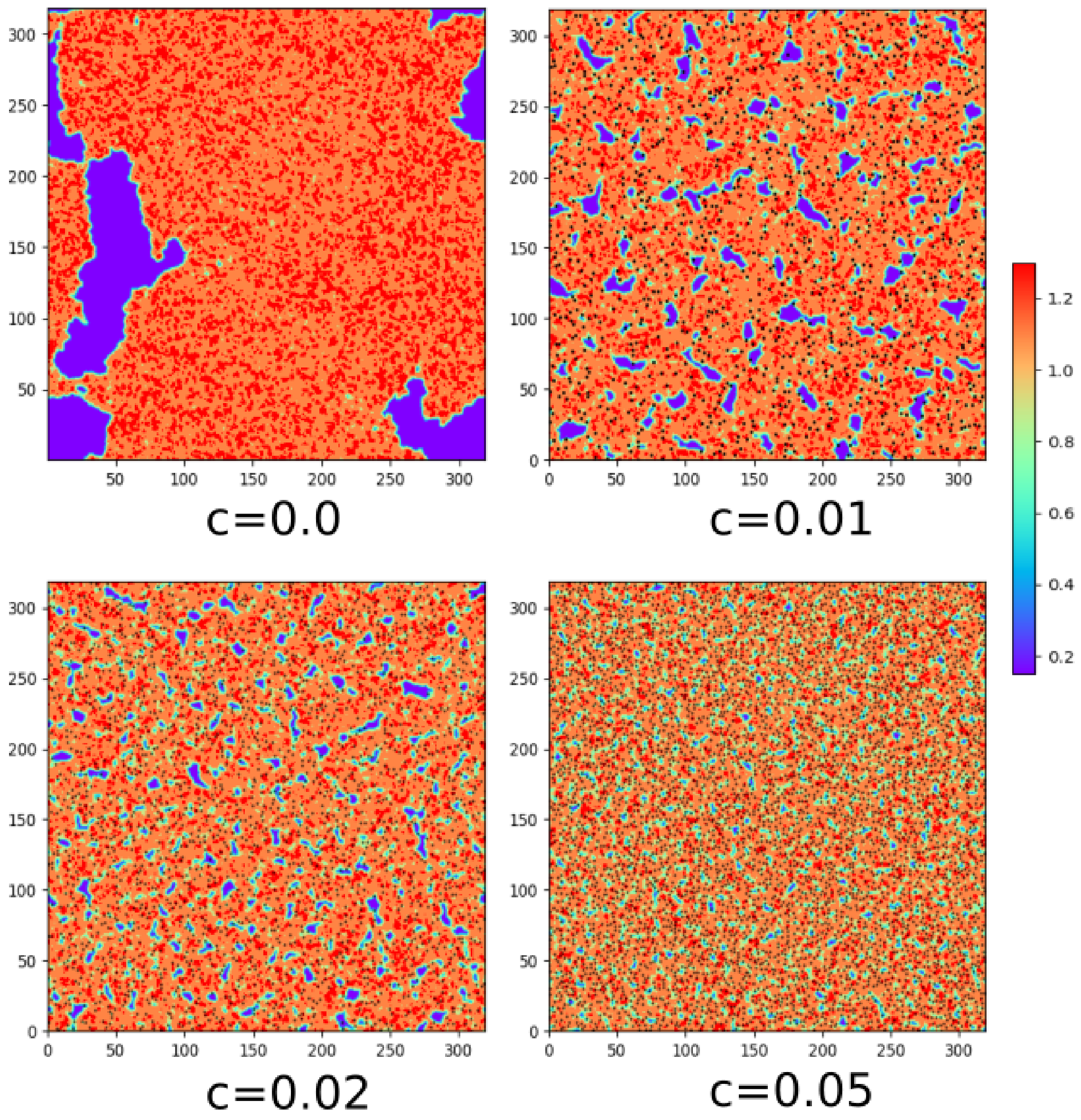

Figure 5.2. Density field for different pinning concentrations, $c = 0.00$ (a), 0.01 (b), 0.02 (c), 0.05 (d), measured at $\rho = 0.982$.

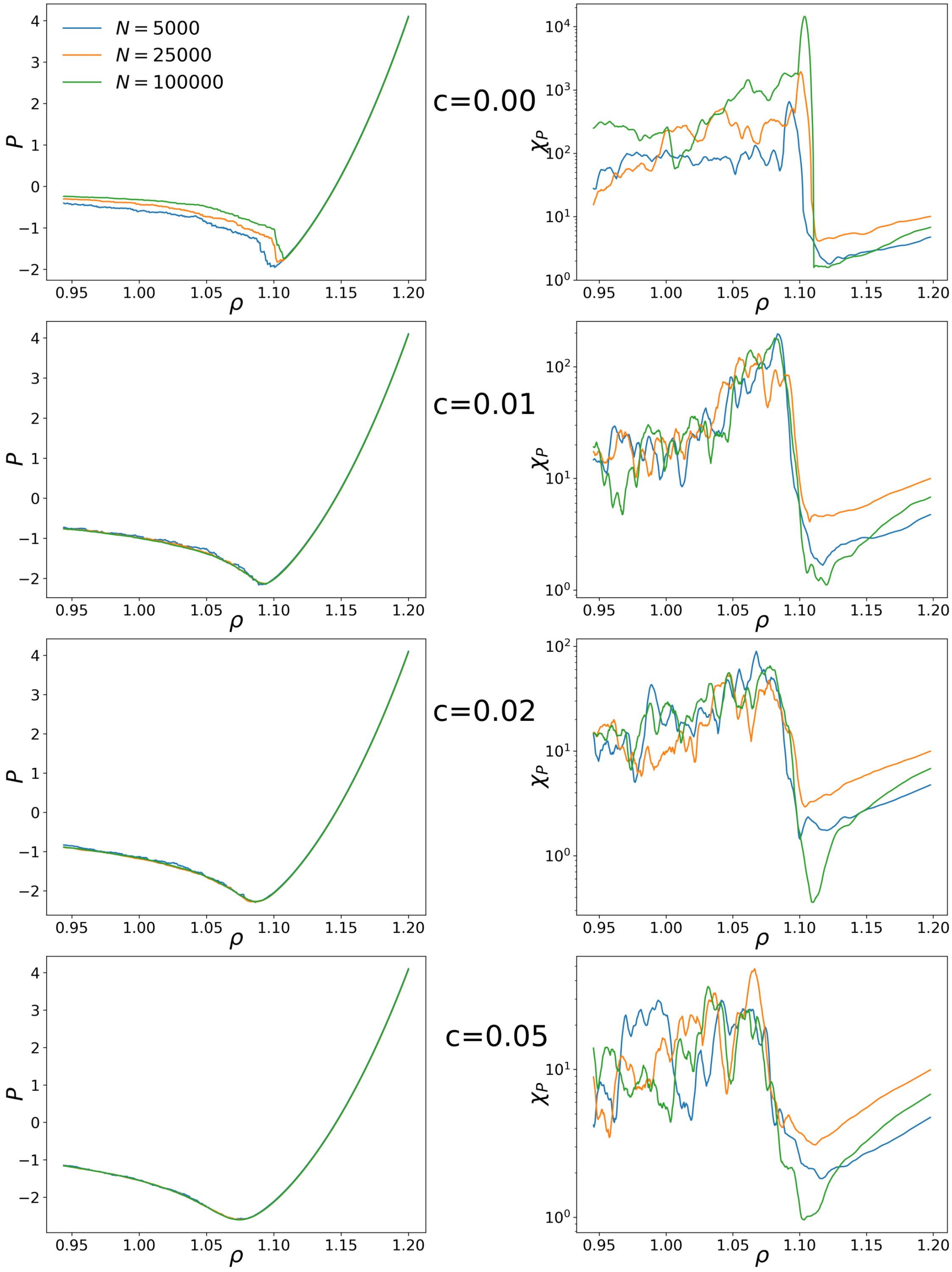

Figure 5.3. Left panel: The ensemble averaged pressure(P) vs density (ρ) curves for different system sizes at the specified values of pinning concentrations (as marked). Right panel: Pressure susceptibility χ_p vs density ρ plots corresponding to the left panel plots

to the square-root singularity. Vanishing of only the lowest non-zero eigenvalue near the plastic instability ensures that the spatial map of eigenmode corresponding to vanishing eigenvalue predicts the displacement field on approach to such a plastic instability [28]. The same scenario of a square-root singularity with only one vanishing eigenvalue was shown to hold under athermal quasistatic expansion on approach to cavitation instabilities and all other plastic events in our previous work [129].

In the current context of athermal quasistatic expansion of pinned solids, we find that the same square-root singularity scenario holds. In Figure 5.5(a) we show one such trajectory corresponding to $c = 0.05$ & N=2500, where for the pressure-jumps marked in black, Figure 5.5(b) shows the square root singularity where the lowest-eigenvalue of the Hessian vanishes as $\lambda_{min} \sim \sqrt{(\rho - \rho_c)/\rho_c}$ on approach to the plastic instabilities at the points marked in Figure 5.5(a), where ρ_c is the point at which the plastic instability occurs. The Figure 5.5(d)-(e) show an eigenmode on approach to the plastic instability, displacement field on approach to the plastic instability and the displacement field across the pressure drop respectively for one of the pressure-jumps in Figure 5.5(a)& (b). As evident from the vector-field maps, the displacement fields on approach to an instability are predicted by the eigenvector of λ_{min} but the displacement fields across the pressure-jump, do not have a high overlap with the eigenmode on approach to the instability. This occurs because of the cascade/avalanche nature of the plastic jump. These avalanches are also more localised spatially due to pinning unlike the avalanches seen in unpinned solids which can be system spanning [129–131]. All in all, mechanism of plasticity on PEL being analogous to unpinned solids does not come as a surprise because pinning only blocks certain pathways of relaxation on the PEL of unpinned solids [132].

5.4.4 Spatial decay of plastic modes & a length scale of plasticity

The plasticity under shear deformation is known to occur via localised rearrangements of particles in a shear transformation zone [26, 133, 134]. These localised rearrange-

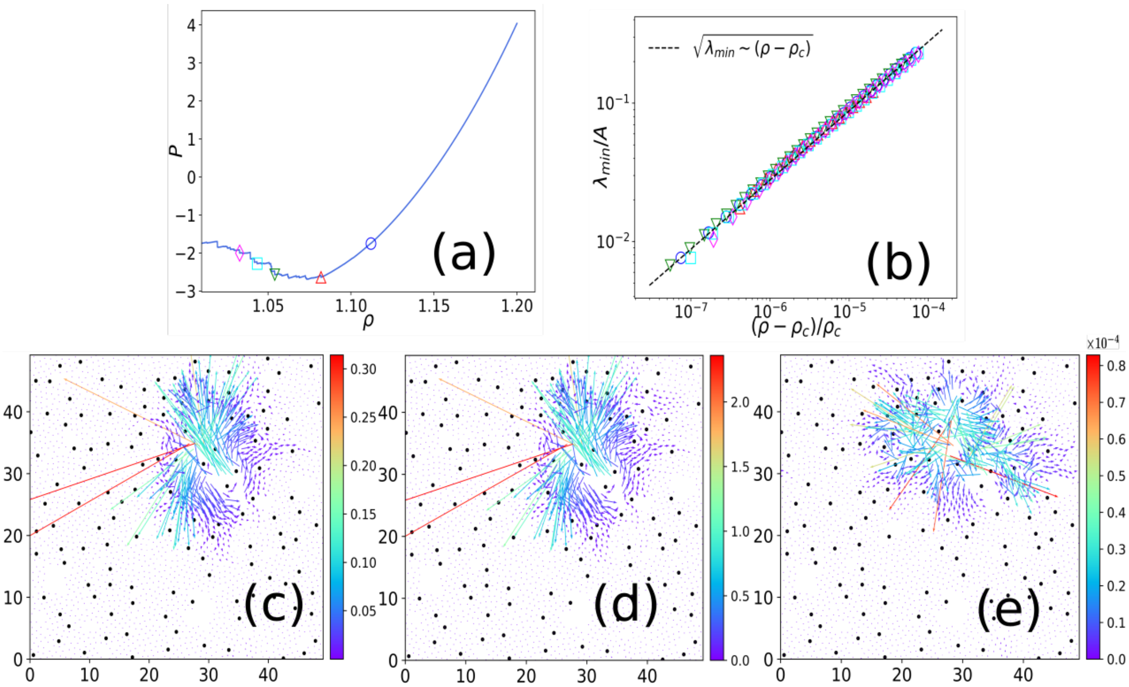

Figure 5.4. (a) Pressure P vs density ρ for an expansion trajectory, using $N = 2500$, corresponding to $c = 0.05$. (b) Demonstration of square-root singularity for lowest eignevalue of the Hessian, λ_{min} (appropriately scaled by fit parameter A), computed at the density points in (a) corresponding to occurrence of plastic instabilities; ρ_c is the estimate density location of the event in each case. (c) Eigenmode, (d) displacement field just before the drop and (e) displacement fields across the plastic drop, occurring at one such plastic event, near $\rho \approx 1.03277$.

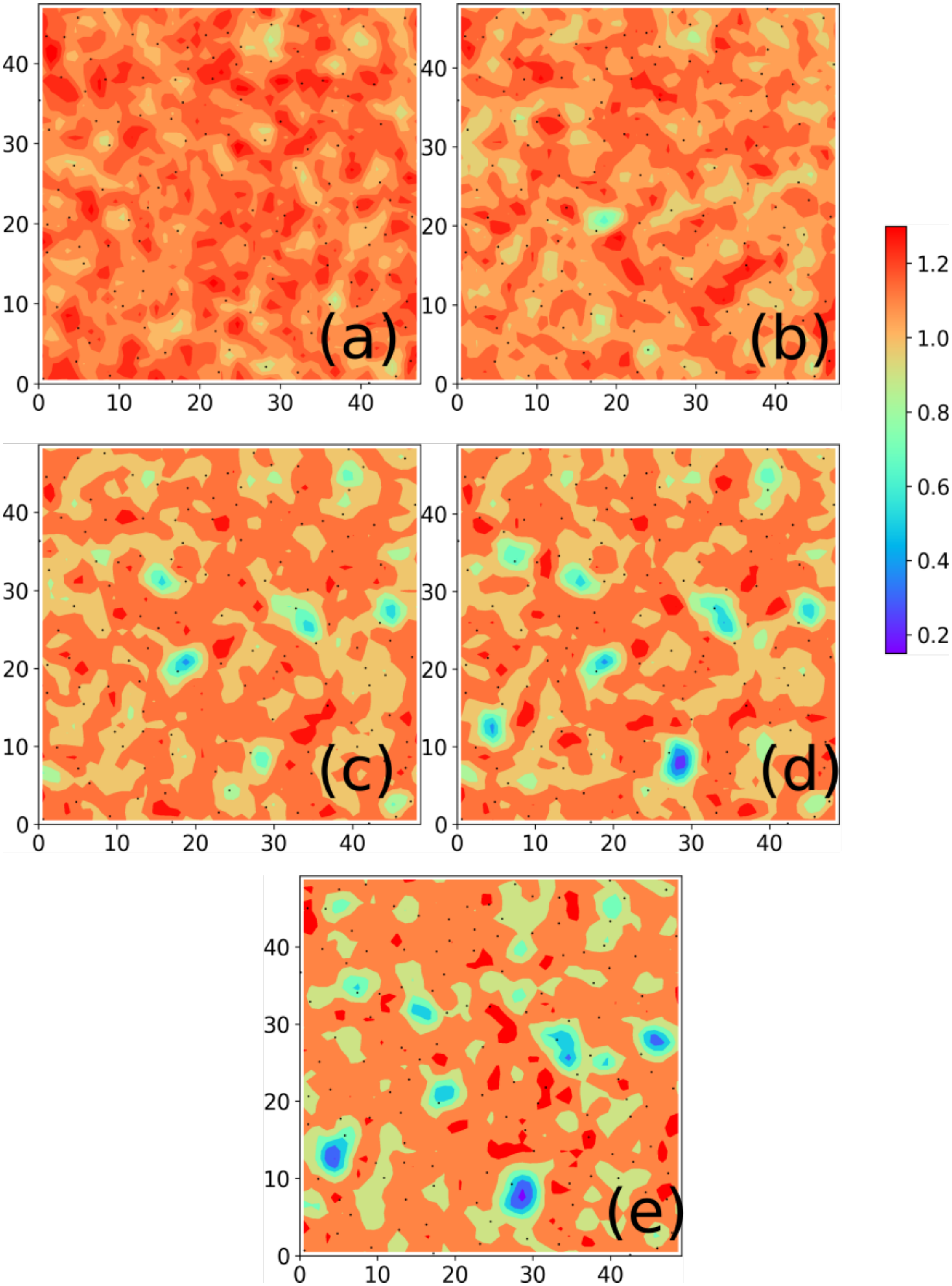

Figure 5.5. (a)-(e) Evolution of the density field across an expansion trajectory for the points marked in Figure 5.5(a).

ments (and their eigenmode) have a quadrupolar shape [33,135] and the radial part of the displacements of the medium decay as $r^{-(d-1)}$; where r is the distance from the center of rearrangement, and d is the spatial dimensions. Even though the rearrangements are local, the displacement fields have a long-range character, i.e., in 2d, they decay as $1/r$ from the center. The eigenmodes, $\vec{e}$, corresponding to the vanishing eigenvalue λ_{min} are known to decide the direction of failure on the PEL for both shear and expansion [28,129,136,137].

In the context of pinning, we, too, look at the radial decay profile of displacements from the plastic center [1] of the eigenmode $\vec{e}$, just before the plastic event, i.e., at a distance of $\delta\rho \approx 10^{-7}$, in the pre-yield regime. We choose to study the spatial profiles in the pre-yield regime, where density inhomogeneities (which can interfere with the profile shapes) are largely absent. The decay profiles averaged over 10 plastic events for each pinning concentration are shown in Figure 5.6(a). For the unpinned case, as one would expect, the decay profile $e(r) \sim 1/r$. For the pinned solids, interestingly, we find two regimes. For the smaller pinning concentrations, *viz.* $c = 0.01$, $c = 0.02$ and $c = 0.05$, we see that the decay profile fits a screened power-law function $e(r) \sim \exp(-r/\xi)/r^{\eta}$ with $\eta \approx 0.42$ for $c = 0.01$ and $c = 0.02$ whereas $\eta = 0.13$ for $c = 0.05$. For larger pinning concentration, *viz.* $c = 0.08$, we find that the decay profile is well-fitted by an exponential form $e(r) \sim \exp(-r/\xi)$ suggesting a crossover from a screening-like decay to a purely exponential decay. The scale-dependent exponential part of the decay profile allows us to extract a length scale ξ from the fit parameters. The values of ξ_{fit} for different pinning concentrations are shown using red color in Figure 5.6(b).

For a fixed pinning concentration c, one naturally obtains a length scale $\xi_{pin} = \sqrt{1/(c \cdot \rho)}$, which denotes an average distance between any two pinned sites. But, since the eigenmode decay profiles shown in Figure 5.6(a) are sampled at different densities from the expansion trajectory, the blue curve showing $\xi_{pin} = \sqrt{1/(c \cdot \rho)}$ for the sampled densities in Figure 5.6(b). The length scale extracted from the fits in Figure 5.6(a) thus shows reasonable parallels with the length scale introduced by pinning as seen in Figure 5.6(b). The

---

[1] defined as particle undergoing highest displacement in an eigenmode

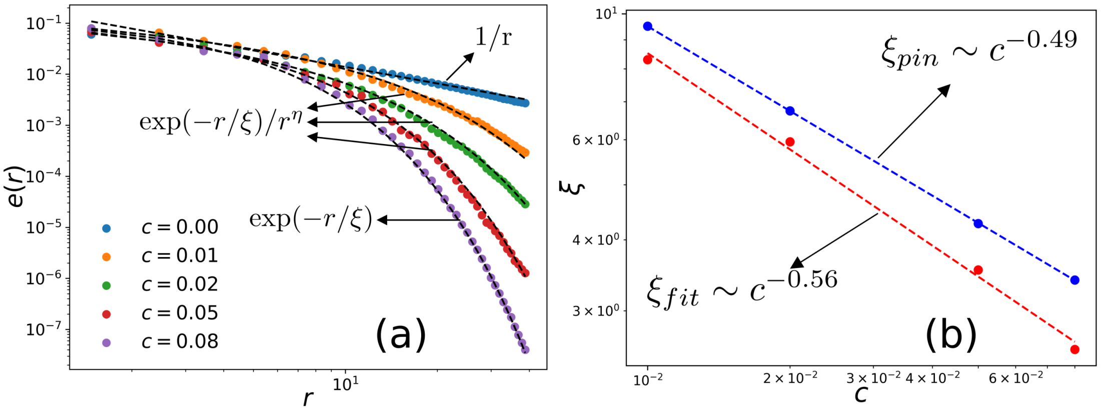

Figure 5.6. (a) Spatial decay profile of magnitude of displacements in the eigenmode before the yielding, $e(r)$, leading to the plastic events, shown for $c = 0.00, 0.01, 0.02, 0.05, 0.08$, with averaging done over 10 plastic events for each case. r is the distance from the plastic center defined by a particle undergoing maximum displacement in a mode. (b)Dependence of length scale (ξ_{fit}) extracted from fits to $e(r)$ (see text for discussion) with pinning concentration; also shown is the behaviour of ξ_{pin}, extracted from pinning density, with c.

decay exponents of length scales with pinning concentrations for ξ_{pin} is slightly different from exponent 0.5 primarily due to the changes in density where these decay profiles are obtained for each pinning concentration.

The exponential nature of the decay profiles and the extracted length scales thus suggest that, with increasing pinning concentrations, the displacements in the eigenmode become more and more localized. This implies that the consequence of plastic events in a pinned solid has reduced spatial effects, unlike the unpinned solid, which has a non-local power-law character. Hence, this will restrict the size of cascades/avalanches, which are caused due to triggering of multiple such plastic modes at different spatial locations [138]. This is also consistent with the data in Figure 5.1(e) & (f), where the magnitude of the drops in pressure/energy decrease with an increase in pinning concentration. The presence of a plasticity length scale in pinned solids also explains why there are negligible system size effects in the data shown in Figure 5.3 as long as $\xi << L$, which is the case for the system sizes that we report. As the length-scale ξ prevents the system from acting as a whole beyond the lengths $l > \xi$.

5.5 Summary & Discussion

Our work [139] thus demonstrates, how an amorphous solid with a small concentration of micro-alloyed inclusions intended to make the solid stronger can delay the cavitation and increase the tensile strength. The resulting glass obtained from micro-alloying inclusions is thus a stronger glass less susceptible to fracture via cavitation. From a thermodynamic point of view, the delay in cavitation and thus the increase in tensile-strength is likely a result of change in the densities of coexisting solid and gas phases in the temperature-density [75, 117] phase diagram of the amorphous solid. A sharp yielding-like cavitation transition observed in amorphous solids [85, 129] accompanied by an extensive peak in the pressure fluctuations characterized via a susceptibility χ_p is suppressed by particle-pinning. Particle pinning not only increases the tensile strength but also decreases the size of avalanches that lead to cavitation in amorphous solids by restricting them spatially, as a result, the cavitation occurs more homogeneously in this pinned solid. The expansion-response of a pinned solid is somewhat analogous to the shear response of a ductile solid as the sharp macroscopic drop leading to yielding is absent. But the analogy with a ductile-solid doesn't hold completely as the yielding via cavitation is delayed in pinned solids and in a ductile solids, the yielding under shear would occur at lower strains [90]. Also with increasing system sizes, the ductile solid is known to show brittle behaviour under shear via shear-banding like events in a recent work [140]. In our range of probing, the finite size effects in the pressure P vs ρ curves and in the pressure fluctuation χ_p vs ρ curves do not show such a brittle like character for the large system-sizes. The absence of finite-size effects in the $P-\rho$ and $\chi_p-\rho$ curves along with decreasing sizes of avalanches, is explained using a length-scale extracted from the spatial decay of displacements in plastic-eigenmodes.

We have modeled these micro-alloyed inclusions using particle pinning but it stands merely as a simplifying approximation, future studies can perhaps cook up more realistic models of inclusions [141] in amorphous solids and study their deformation response.

6 Summary, Discussion & Outlook

Our work has explored different directions in understanding the cavitation instabilities in amorphous solids. As discussed in the introduction, cavitation is known to play a crucial role in fracture of large varieties of amorphous solids. Thus, we have first explored the elasto-plastic response of an amorphous solid under uniform expansion where cavitation of the amorphous solid is expected to occur as the system is driven into glass-gas coexistence region of the $T - \rho$ phase diagram. The cavitation occurs via irreversible particle-rearrangements in the solid. We have attempted to understand this plasticity due to cavitation under expansion using the framework of plasticity under shear deformation of amorphous solids which has been studied extensively at all the scales. Our work firstly demonstrates how the mechanism of irreversible-particle rearrangements on the potential energy landscape is universal via a saddle-node bifurcation. In the studies of plastic deformation under shear, the saddle-node bifurcation has been shown as equivalent to vanishing of athermal elastic constants near a plastic instability via universal power-laws [35]. And these relations have been used in calculating the barrier of plasticity in the vicinity of plastic events [106], and to predict the plastic strains at which cavitation occurs [36]. Detailed studies along these directions will be undertaken in future. Our work also finds weibull-like distributions of pressure-jumps $P(\Delta P)$ and energy-drops $P(\Delta U)$ due to propagation of fracture via cavitation and finds sub-extensive system-size scalings. These scalings and exponents provide a valuable test for meso-scale elasto-plastic models encompassing cavitation driven failure of amorphous solids in future. We have also shown relaxation via eshelby-like events in the elastic-branch under expansion which has been reported for amorphous solids under shear deformation too. Thus our work on amorphous solids under expansion, by and large, establishes multiple parallels with the well-studied plasticity under shear.

The first part of our work suggests a possibility of coupling between shear-response of amorphous solid and expansion response of amorphous solids. This motivated us to explore the response of amorphous solids to combinations of expansion and cyclic-shear deformations. We have found instances of cavitation instabilities at lower energy thresholds and higher densities under combinations of expansion and cyclic-shear. This suggests how multiple deformation modes could couple in an amorphous solids to create cavities in it and reduce its mechanical strength. The occurrence of cavitation depends on the amplitude of cyclic-shear driving γ_{max} and the density at which the expanded state is sampled from i.e ρ. Our work marks a region in the $\gamma_{max} - \rho$ phase plane where one observed cavitation under cyclic shear. The studies of amorphous solids under shear deformation in numerical simulations did not involve cavitation as the studies focused on the region where cavitation is not expected to occur. Our work, thus sheds more light on this by marking the region where one can expect to observe cavitation and paves the way for future studies where it should be possible to study mechanical response of amorphous solids under combination of various deformation modes. We have also demonstrated abundance of soft-spots and abundance of cavitation modes by showing the sensitivity to the control parameters γ and ρ that occur both below and above the yielding thresholds under cyclic-shear. This could be one of the possible reasons why a large variety of amorphous solids underog failure via cavitation [62]. Overall, our explorations establish how multiple deformation modes can couple to give rise to early mechanical failure, which can be detrimental to mechanical-stability of amorphous solids.

Our first two studies have explored variety of settings where cavitation instabilities occur, i.e under uniform expansion and under combination of uniform expansion and cyclic-shear. In the third work, from a point of view of making stronger amorphous solids, we have looked at the effect of pinning a few particles (a model for glasses micro-alloyed with inclusions [108, 124, 127]) on cavitation under uniform expansion. We have demonstrated that the micro-alloyed amorphous solids have a higher-tensile strength and show more spatially-homogeneous and gradual cavitation via formation of a large number of cavities. Our work finds no significant system size effects in pinned solids unlike the case with uniform expansion of amorphous solids. To a fair extent, the expansion-response becomes more ductile-like due to particle pinning. These results are consistent with the studies on yielding under shear in micro-alloyed amorphous solids, where in, spatially-homogeneous yielding was observed. The plastic-events leading to cavitation too occur via a saddle-node bifurcation on the landscape which is expected. The spatial-decay profile of the eigenmodes of the Hessian matrix leading to cavitation events, follow screened-like exponential decay, i.e. $e(r) \sim \exp(-r/\xi)/r^{\eta}$ unlike the case of unpinned solids, where the decay profiles are long-ranged $e(r) \sim 1/r$. This implies a drastic change in the decay profile-due to pinning and the length-scale extracted from the screened-exponential fits, parallels the length-scale set by average distance between two pinned-sites. The presence of this length-scale also explains the negligible system-size effects in pinned amorphous solid. All-in all our work investigates a possible direction to make amorphous solids more resistant to mechanical failure via cavitation.

The work in this thesis opens up myriad of questions and directions related to understanding cavitation instabilities in amorphous solids. A major one of them being, identification of soft-spots susceptible to cavitation. For the studies of plasticity under shear, a variety of ways to predict the location of soft-spots susceptible to irreversible rearrangements have been identified with reasonable success [111]. Whether these indicators work well in predicting cavitation or not remains to be understood. Since a large number of cavitation modes have been shown to exist in Chapter 3, the predictors of soft-spots for these cavitation must take into account the dependence of the soft-spot on the deformation mode and the parameters of driving.

For the studies of plasticity under shear, a large amount of effort has been dedicated to constructing meso-scale elasto-plastic models [27] which reproduce the phenomenology of shear deformation of amorphous solids. These models provide key physical insights into the physics at intermediate length-scales. Constructing such models involving cavitation-instabilities could be a very useful and interesting direction of future research. As cavitation instabilities involve significantly more density fluctuations than yielding under shear, incorporating the density fluctuations and resulting stress re-distributions would constitute first major steps in this direction.

To conclude, research work discussed in this thesis has taken significant leaps in understanding the cavitation instabilities in amorphous solids. The work also opens new avenues for studies of mechanical deformation in amorphous solids under deformation protocols involving cavitation instabilities.

Bibliography

[1] W. Commons, *Glass*, 2007. https://en.wikipedia.org/wiki/Glass.

[2] A. Nicolas, E. E. Ferrero, K. Martens, and J.-L. Barrat, *Deformation and flow of amorphous solids: Insights from elastoplastic models*, Reviews of Modern Physics **90** no. 4, (2018) 045006.

[3] C. T. Moynihan, A. J. Easteal, J. Wilder, and J. Tucker, *Dependence of the glass transition temperature on heating and cooling rate*, The journal of physical chemistry **78** no. 26, (1974) 2673–2677.

[4] W. Gotze and L. Sjogren, *Relaxation processes in supercooled liquids*, Reports on progress in Physics **55** no. 3, (1992) 241.

[5] C. A. Angell, *Formation of glasses from liquids and biopolymers*, Science **267** no. 5206, (1995) 1924–1935.

[6] P. G. Debenedetti and F. H. Stillinger, *Supercooled liquids and the glass transition*, Nature **410** no. 6825, (2001) 259–267.

[7] S. Sastry, P. G. Debenedetti, and F. H. Stillinger, *Signatures of distinct dynamical regimes in the energy landscape of a glass-forming liquid*, Nature **393** no. 6685, (1998) 554–557.

[8] Z. Raza, B. Alling, and I. A. Abrikosov, *Computer simulations of glasses: the potential energy landscape*, Journal of Physics: Condensed Matter **27** no. 29, (2015) 293201.

[9] A. Heuer, *Exploring the potential energy landscape of glass-forming systems: from inherent structures via metabasins to macroscopic transport*, Journal of Physics: Condensed Matter **20** no. 37, (2008) 373101.

[10] D. J. Wales, M. A. Miller, and T. R. Walsh, *Archetypal energy landscapes*, Nature **394** no. 6695, (1998) 758–760.

[11] D. J. Wales, *The energy landscape as a unifying theme in molecular science*, Philosophical Transactions of the Royal Society A: Mathematical, Physical and Engineering Sciences **363** no. 1827, (2005) 357–377.

[12] T. B. Schrøder, S. Sastry, J. C. Dyre, and S. C. Glotzer, *Crossover to potential energy landscape dominated dynamics in a model glass-forming liquid*, The Journal of Chemical Physics **112** no. 22, (2000) 9834–9840.

[13] V. K. de Souza and D. J. Wales, *Energy landscapes for diffusion: Analysis of cage-breaking processes*, The Journal of chemical physics **129** no. 16, (2008) 164507.

[14] V. K. de Souza and D. J. Wales, *Connectivity in the potential energy landscape for binary lennard-jones systems*, The Journal of chemical physics **130** no. 19, (2009) 194508.

[15] J. P. Doye, M. A. Miller, and D. J. Wales, *The double-funnel energy landscape of the 38-atom lennard-jones cluster*, The Journal of Chemical Physics **110** no. 14, (1999) 6896–6906.

[16] S. Sastry, *Inherent structure approach to the study of glass-forming liquids*, Phase Transitions **75** no. 4-5, (2002) 507–517.

[17] D. L. Malandro and D. J. Lacks, *Relationships of shear-induced changes in the potential energy landscape to the mechanical properties of ductile glasses*, The Journal of Chemical Physics **110** no. 9, (1999) 4593–4601, `https://doi.org/10.1063/1.478340`. `https://doi.org/10.1063/1.478340`.

[18] J. Chattoraj, O. Gendelman, M. P. Ciamarra, and I. Procaccia, *Oscillatory instabilities in frictional granular matter*, Physical review letters **123** no. 9, (2019) 098003.

[19] I. Regev, I. Attia, K. Dahmen, S. Sastry, and M. Mungan, *Topology of the energy landscape of sheared amorphous solids and the irreversibility transition*, Physical Review E **103** no. 6, (2021) 062614.

[20] N. Oyama, H. Mizuno, and A. Ikeda, *Instantaneous normal modes reveal structural signatures for the herschel-bulkley rheology in sheared glasses*, Physical Review Letters **127** no. 10, (2021) 108003.

[21] P. M. Anderson, J. P. Hirth, and J. Lothe, Theory of dislocations. Cambridge University Press, 2017.

[22] H. Hentschel, S. Karmakar, E. Lerner, and I. Procaccia, *Do athermal amorphous solids exist?*, Physical Review E **83** no. 6, (2011) 061101.

[23] J. Wang, Y. Wang, W. Cai, J. Li, Z. Zhang, and S. X. Mao, *Discrete shear band plasticity through dislocation activities in body-centered cubic tungsten nanowires*, Scientific reports **8** no. 1, (2018) 4574.

[24] S. Kiselev, *Dislocation structure of shear bands in single crystals*, Journal of applied mechanics and technical physics **47** (2006) 857–866.

[25] M. Ozawa, L. Berthier, G. Biroli, A. Rosso, and G. Tarjus, *Random critical point separates brittle and ductile yielding transitions in amorphous materials*,

Proceedings of the National Academy of Sciences **115** no. 26, (2018) 6656–6661, `https://www.pnas.org/doi/pdf/10.1073/pnas.1806156115`. `https://www.pnas.org/doi/abs/10.1073/pnas.1806156115`.

[26] M. L. Falk and J. S. Langer, *Dynamics of viscoplastic deformation in amorphous solids*, Phys. Rev. E **57** (Jun, 1998) 7192–7205. `https://link.aps.org/doi/10.1103/PhysRevE.57.7192`.

[27] A. Nicolas, E. E. Ferrero, K. Martens, and J.-L. Barrat, *Deformation and flow of amorphous solids: Insights from elastoplastic models*, Reviews of Modern Physics **90** no. 4, (2018) 045006.

[28] C. E. Maloney and A. Lemaître, *Amorphous systems in athermal, quasistatic shear*, Phys. Rev. E **74** (Jul, 2006) 016118. `https://link.aps.org/doi/10.1103/PhysRevE.74.016118`.

[29] M. L. Manning, J. S. Langer, and J. Carlson, *Strain localization in a shear transformation zone model for amorphous solids*, Physical review E **76** no. 5, (2007) 056106.

[30] M. Manning, E. Daub, J. Langer, and J. Carlson, *Rate-dependent shear bands in a shear-transformation-zone model of amorphous solids*, Physical Review E **79** no. 1, (2009) 016110.

[31] S. Karmakar, E. Lerner, I. Procaccia, and J. Zylberg, *Statistical physics of elastoplastic steady states in amorphous solids: Finite temperatures and strain rates*, Physical Review E **82** no. 3, (2010) 031301.

[32] E. Lerner, I. Procaccia, C. Rainone, and M. Singh, *Protocol dependence of plasticity in ultrastable amorphous solids*, Physical Review E **98** no. 6, (2018) 063001.

[33] J. D. Eshelby, *The determination of the elastic field of an ellipsoidal inclusion, and related problems*, Proceedings of the royal society of London. Series A. Mathematical and physical sciences **241** no. 1226, (1957) 376–396.

[34] C. Maloney and A. Lemaître, *Universal breakdown of elasticity at the onset of material failure*, Phys. Rev. Lett. **93** (Nov, 2004) 195501. `https://link.aps.org/doi/10.1103/PhysRevLett.93.195501`.

[35] S. Karmakar, E. Lerner, and I. Procaccia, *Athermal nonlinear elastic constants of amorphous solids*, Phys. Rev. E **82** (Aug, 2010) 026105.

[36] S. Karmakar, A. Lemaître, E. Lerner, and I. Procaccia, *Predicting plastic flow events in athermal shear-strained amorphous solids*, Phys. Rev. Lett. **104** (May, 2010) 215502. `https://link.aps.org/doi/10.1103/PhysRevLett.104.215502`.

[37] S. Karmakar, E. Lerner, and I. Procaccia, *Statistical physics of the yielding transition in amorphous solids*, Physical Review E **82** no. 5, (2010) 055103.

[38] C. Maloney and A. Lemaitre, *Subextensive scaling in the athermal, quasistatic limit of amorphous matter in plastic shear flow*, Physical review letters **93** no. 1, (2004) 016001.

[39] A. Lemaître and C. Caroli, *Rate-dependent avalanche size in athermally sheared amorphous solids*, Physical review letters **103** no. 6, (2009) 065501.

[40] C. Liu, E. E. Ferrero, F. Puosi, J.-L. Barrat, and K. Martens, *Driving rate dependence of avalanche statistics and shapes at the yielding transition*, Physical review letters **116** no. 6, (2016) 065501.

[41] D. Fiocco, G. Foffi, and S. Sastry, *Oscillatory athermal quasistatic deformation of a model glass*, Physical Review E **88** no. 2, (2013) 020301.

[42] I. Regev, T. Lookman, and C. Reichhardt, *Onset of irreversibility and chaos in amorphous solids under periodic shear*, Physical Review E **88** no. 6, (2013) 062401.

[43] P. Leishangthem, A. D. Parmar, and S. Sastry, *The yielding transition in amorphous solids under oscillatory shear deformation*, Nature communications **8** no. 1, (2017) 1–8.

[44] H. Bhaumik, G. Foffi, and S. Sastry, *The role of annealing in determining the yielding behavior of glasses under cyclic shear deformation*, Proceedings of the National Academy of Sciences **118** no. 16, (2021) e2100227118, `https://www.pnas.org/doi/pdf/10.1073/pnas.2100227118`. `https://www.pnas.org/doi/abs/10.1073/pnas.2100227118`.

[45] K. Khirallah, B. Tyukodi, D. Vandembroucq, and C. E. Maloney, *Yielding in an integer automaton model for amorphous solids under cyclic shear*, Physical Review Letters **126** no. 21, (2021) 218005.

[46] M. Mungan, S. Sastry, K. Dahmen, and I. Regev, *Networks and hierarchies: How amorphous materials learn to remember*, Physical review letters **123** no. 17, (2019) 178002.

[47] N. V. Priezjev, *Fatigue failure of amorphous alloys under cyclic shear deformation*, arXiv preprint arXiv:2301.07857 (2023) .

[48] A. Kanjilal, P. Kumar, et al., *Transition from necking to cavitation driven tertiary creep with length scale in constrained ductile metal joints*, Materials Science and Engineering: A **845** (2022) 143205.

[49] F. Caupin and E. Herbert, *Cavitation in water: a review*, Comptes Rendus Physique **7** no. 9-10, (2006) 1000–1017.

[50] J. B. Estrada, C. Barajas, D. L. Henann, E. Johnsen, and C. Franck, *High strain-rate soft material characterization via inertial cavitation*, Journal of the Mechanics and Physics of Solids **112** (2018) 291–317.

[51] J. Goeller, A. Wardlaw, D. Treichler, J. O'Bruba, and G. Weiss, *Investigation of cavitation as a possible damage mechanism in blast-induced traumatic brain injury*, Journal of neurotrauma **29** no. 10, (2012) 1970–1981.

[52] V. N. Prakash, M. S. Bull, and M. Prakash, *Motility-induced fracture reveals a ductile-to-brittle crossover in a simple animal's epithelia*, Nature Physics **17** no. 4, (2021) 504–511.

[53] G. N. Kawchuk, J. Fryer, J. L. Jaremko, H. Zeng, L. Rowe, and R. Thompson, *Real-time visualization of joint cavitation*, PloS one **10** no. 4, (2015) e0119470.

[54] G. Wang, D. Zhao, H. Bai, M. Pan, A. Xia, B. Han, X. Xi, Y. Wu, and W. Wang, *Nanoscale periodic morphologies on the fracture surface of brittle metallic glasses*, Physical review letters **98** no. 23, (2007) 235501.

[55] E. Bouchaud, D. Boivin, J.-L. Pouchou, D. Bonamy, B. Poon, and G. Ravichandran, *Fracture through cavitation in a metallic glass*, Europhysics Letters **83** no. 6, (2008) 66006.

[56] P. Murali, T. Guo, Y. Zhang, R. Narasimhan, Y. Li, and H. Gao, *Atomic scale fluctuations govern brittle fracture and cavitation behavior in metallic glasses*, Physical Review Letters **107** no. 21, (2011) 215501.

[57] M. Jiang, G. Wilde, J. Chen, C. Qu, S. Fu, F. Jiang, and L. Dai, *Cryogenic-temperature-induced transition from shear to dilatational failure in metallic glasses*, Acta materialia **77** (2014) 248–257.

[58] I. Singh, R. Narasimhan, and U. Ramamurty, *Cavitation-induced fracture causes nanocorrugations in brittle metallic glasses*, Physical Review Letters **117** no. 4, (2016) 044302.

[59] C. Guerra, J. Scheibert, D. Bonamy, and D. Dalmas, *Understanding fast macroscale fracture from microcrack post mortem patterns*, Proceedings of the National Academy of Sciences **109** no. 2, (2012) 390–394.

[60] A. Pawlak, A. Galeski, and A. Rozanski, *Cavitation during deformation of semicrystalline polymers*, Progress in polymer science **39** no. 5, (2014) 921–958.

[61] F. Célarié, S. Prades, D. Bonamy, L. Ferrero, E. Bouchaud, C. Guillot, and C. Marliere, *Glass breaks like metal, but at the nanometer scale*, Physical Review Letters **90** no. 7, (2003) 075504.

[62] L.-Q. Shen, J.-H. Yu, X.-C. Tang, B.-A. Sun, Y.-H. Liu, H.-Y. Bai, and W.-H. Wang, *Observation of cavitation governing fracture in glasses*, Science Advances **7** no. 14, (2021) eabf7293.

[63] Y. Qiao, X. Cai, C. Ouyang, and Y. Zheng, *Effect of hydrogen on cavitation erosion behaviour of high strength steel*, Int. J. Electrochem. Sci **11** (2016) 10329–10346.

[64] R. Maass, P. Birckigt, C. Borchers, K. Samwer, and C. A. Volkert, *Long range stress fields and cavitation along a shear band in a metallic glass: The local origin of fracture*, Acta Materialia **98** (2015) 94–102.

[65] P. Murali, R. Narasimhan, T. Guo, Y. Zhang, and H. Gao, *Shear bands mediate cavitation in brittle metallic glasses*, Scripta Materialia **68** no. 8, (2013) 567–570.

[66] J. Luo and Y. Shi, *Tensile fracture of metallic glasses via shear band cavitation*, Acta Materialia **82** (2015) 483–490.

[67] P. Guan, S. Lu, M. J. Spector, P. K. Valavala, and M. L. Falk, *Cavitation in amorphous solids*, Physical Review Letters **110** no. 18, (2013) 185502.

[68] P. Chaudhuri and J. Horbach, *Structural inhomogeneities in glasses via cavitation*, Physical Review B **94** no. 9, (2016) 094203.

[69] D. Richard, E. Lerner, and E. Bouchbinder, *Brittle-to-ductile transitions in glasses: Roles of soft defects and loading geometry*, MRS bulletin **46** no. 10, (2021) 902–914.

[70] F. Célarié, S. Prades, D. Bonamy, L. Ferrero, E. Bouchaud, C. Guillot, and C. Marliere, *Glass breaks like metal, but at the nanometer scale*, Physical Review Letters **90** no. 7, (2003) 075504.

[71] D. Bonamy, S. Prades, C. Rountree, L. Ponson, D. Dalmas, E. Bouchaud, K. Ravi-Chandar, and C. Guillot, *Nanoscale damage during fracture in silica glass*, International Journal of Fracture **140** (2006) 3–14.

[72] E. Bouchaud, D. Boivin, J.-L. Pouchou, D. Bonamy, B. Poon, and G. Ravichandran, *Fracture through cavitation in a metallic glass*, Europhysics Letters **83** no. 6, (2008) 66006.

[73] K. Paul, R. Dasgupta, J. Horbach, and S. Karmakar, *Cavity formation in deformed amorphous solids on the nanoscale*, Phys. Rev. Research **2** (Oct, 2020) 042012.

[74] J. Scheibert, C. Guerra, F. Célarié, D. Dalmas, and D. Bonamy, *Brittle-quasibrittle transition in dynamic fracture: An energetic signature*, Physical Review Letters **104** no. 4, (2010) 045501.

[75] S. Sastry, *Liquid limits: Glass transition and liquid-gas spinodal boundaries of metastable liquids*, Phys. Rev. Lett. **85** (Jul, 2000) 590–593.

[76] Y.-C. Chen, Z. Lu, K.-i. Nomura, W. Wang, R. K. Kalia, A. Nakano, and P. Vashishta, *Interaction of voids and nanoductility in silica glass*, Physical Review Letters **99** no. 15, (2007) 155506.

[77] I. Singh, T. Guo, P. Murali, R. Narasimhan, Y. Zhang, and H. Gao, *Cavitation in materials with distributed weak zones: implications on the origin of brittle fracture in metallic glasses*, Journal of the Mechanics and Physics of Solids **61** no. 4, (2013) 1047–1064.

[78] X. Huang, Z. Ling, Y. Wang, and L. Dai, *Intrinsic structural defects on medium range in metallic glasses*, Intermetallics **75** (2016) 36–41.

[79] C. Liu, V. Roddatis, P. Kenesei, and R. Maaß, *Shear-band thickness and shear-band cavities in a zr-based metallic glass*, Acta Materialia **140** (2017) 206–216.

[80] Y. He, P. Yi, and M. L. Falk, *Critical analysis of an fep empirical potential employed to study the fracture of metallic glasses*, Physical review letters **122** no. 3, (2019) 035501.

[81] X. Tang, L. Shen, H. Zhang, W. Li, and W. Wang, *Crack tip cavitation in metallic glasses*, Journal of Non-Crystalline Solids **592** (2022) 121762.

[82] E. Bouchbinder, T.-S. Lo, and I. Procaccia, *Dynamic failure in amorphous solids via a cavitation instability*, Physical Review E **77** no. 2, (2008) 025101.

[83] E. Bouchbinder, T.-S. Lo, I. Procaccia, and E. Shtilerman, *Stability of an expanding circular cavity and the failure of amorphous solids*, Physical Review E **78** no. 2, (2008) 026124.

[84] S. Karmakar, E. Lerner, and I. Procaccia, *Plasticity-induced anisotropy in amorphous solids: The bauschinger effect*, Physical Review E **82** no. 2, (2010) 026104.

[85] Y. E. Altabet, F. H. Stillinger, and P. G. Debenedetti, *A cavitation transition in the energy landscape of simple cohesive liquids and glasses*, The Journal of Chemical Physics **145** no. 21, (2016) 211905.

[86] Y. E. Altabet, A. L. Fenley, F. H. Stillinger, and P. G. Debenedetti, *Cavitation transition in the energy landscape: Distinct tensile yielding behavior in strongly and weakly attractive systems*, The Journal of Chemical Physics **148** no. 11, (2018) 114501.

[87] K. Paul, R. Dasgupta, J. Horbach, and S. Karmakar, *Cavity formation in deformed amorphous solids on the nanoscale*, Physical Review Research **2** no. 4, (2020) 042012.

[88] S. Karmakar, C. Dasgupta, and S. Sastry, *Growing length and time scales in glass-forming liquids*, Proceedings of the National Academy of Sciences **106** no. 10, (2009) 3675–3679.

[89] K. W. Desmond and E. R. Weeks, *Measurement of stress redistribution in flowing emulsions*, Physical review letters **115** no. 9, (2015) 098302.

[90] W.-T. Yeh, M. Ozawa, K. Miyazaki, T. Kawasaki, and L. Berthier, *Glass stability changes the nature of yielding under oscillatory shear*, Phys. Rev. Lett. **124** (Jun, 2020) 225502. `https://link.aps.org/doi/10.1103/PhysRevLett.124.225502`.

[91] G. Biroli and J.-P. Bouchaud, *The random first-order transition theory of glasses: A critical assessment*, Structural Glasses and Supercooled Liquids: Theory, Experiment, and Applications (2012) 31–113.

[92] S. Karmakar, C. Dasgupta, and S. Sastry, *Growing length scales and their relation to timescales in glass-forming liquids*, Annu. Rev. Condens. Matter Phys. **5** no. 1, (2014) 255–284.

[93] T. S. Grigera and G. Parisi, *Fast monte carlo algorithm for supercooled soft spheres*, Physical Review E **63** no. 4, (2001) 045102.

[94] A. Ninarello, L. Berthier, and D. Coslovich, *Models and algorithms for the next generation of glass transition studies*, Physical Review X **7** no. 2, (2017) 021039.

[95] C. Scalliet, B. Guiselin, and L. Berthier, *Thirty milliseconds in the life of a supercooled liquid*, Physical Review X **12** no. 4, (2022) 041028.

[96] W. Kob and H. C. Andersen, *Testing mode-coupling theory for a supercooled binary lennard-jones mixture i: The van hove correlation function*, Physical Review E **51** no. 5, (1995) 4626.

[97] R. Brüning, D. A. St-Onge, S. Patterson, and W. Kob, *Glass transitions in one-, two-, three-, and four-dimensional binary lennard-jones systems*, Journal of Physics: Condensed Matter **21** no. 3, (2008) 035117.

[98] G. Wahnström, *Molecular-dynamics study of a supercooled two-component lennard-jones system*, Phys. Rev. A **44** (Sep, 1991) 3752–3764. `https://link.aps.org/doi/10.1103/PhysRevA.44.3752`.

[99] U. R. Pedersen, T. B. Schrøder, J. C. Dyre, and P. Harrowell, *Geometry of slow structural fluctuations in a supercooled binary alloy*, Physical review letters **104** no. 10, (2010) 105701.

[100] F. Lançon, L. Billard, and P. Chaudhari, *Thermodynamical properties of a two-dimensional quasi-crystal from molecular dynamics calculations*, Europhysics Letters **2** no. 8, (1986) 625.

[101] M. L. Falk and J. S. Langer, *Dynamics of viscoplastic deformation in amorphous solids*, Phys. Rev. E **57** (Jun, 1998) 7192–7205. `https://link.aps.org/doi/10.1103/PhysRevE.57.7192`.

[102] M. P. Allen and D. J. Tildesley, Computer simulation of liquids. Oxford university press, 2017.

[103] E. Polak and G. Ribiere, *Note sur la convergence de méthodes de directions conjuguées*, ESAIM: Mathematical Modelling and Numerical Analysis - Modélisation Mathématique et Analyse Numérique **3** no. R1, (1969) 35–43.

[104] E. Anderson, Z. Bai, C. Bischof, S. Blackford, J. Demmel, J. Dongarra, J. Du Croz, A. Greenbaum, S. Hammarling, A. McKenney, and D. Sorensen, LAPACK Users' Guide. Society for Industrial and Applied Mathematics, Philadelphia, PA, third ed., 1999.

[105] B. N. Parlett and O. A. Marques, *An implementation of the dqds algorithm (positive case)*, Linear Algebra and its Applications **309** no. 1-3, (2000) 217–259.

[106] S. Karmakar, E. Lerner, and I. Procaccia, *Statistical physics of the yielding transition in amorphous solids*, Phys. Rev. E **82** (Nov, 2010) 055103. `https://link.aps.org/doi/10.1103/PhysRevE.82.055103`.

[107] M. Shimada and N. Oyama, *Gas–liquid phase separation at zero temperature: mechanical interpretation and implications for gelation*, Soft Matter **18** no. 44, (2022) 8406–8417.

[108] B. P. Bhowmik, P. Chaudhuri, and S. Karmakar, *Effect of pinning on the yielding transition of amorphous solids*, Phys. Rev. Lett. **123** (Oct, 2019) 185501. `https://link.aps.org/doi/10.1103/PhysRevLett.123.185501`.

[109] S. Plimpton, *Fast parallel algorithms for short-range molecular dynamics*, Journal of Computational Physics **117** no. 1, (1995) 1–19.

[110] D. Richard, C. Rainone, and E. Lerner, *Finite-size study of the athermal quasistatic yielding transition in structural glasses*, The Journal of Chemical

Physics **155** no. 5, (2021) 056101, https://doi.org/10.1063/5.0053303. https://doi.org/10.1063/5.0053303.

[111] D. Richard, M. Ozawa, S. Patinet, E. Stanifer, B. Shang, S. A. Ridout, B. Xu, G. Zhang, P. K. Morse, J.-L. Barrat, L. Berthier, M. L. Falk, P. Guan, A. J. Liu, K. Martens, S. Sastry, D. Vandembroucq, E. Lerner, and M. L. Manning, *Predicting plasticity in disordered solids from structural indicators*, Phys. Rev. Mater. **4** (Nov, 2020) 113609. https://link.aps.org/doi/10.1103/PhysRevMaterials.4.113609.

[112] H. G. E. Hentschel, S. Karmakar, E. Lerner, and I. Procaccia, *Do athermal amorphous solids exist?*, Phys. Rev. E **83** (Jun, 2011) 061101. https://link.aps.org/doi/10.1103/PhysRevE.83.061101.

[113] B. Shang, P. Guan, and J.-L. Barrat, *Elastic avalanches reveal marginal behavior in amorphous solids*, Proceedings of the National Academy of Sciences **117** no. 1, (2020) 86–92.

[114] J.-L. Barrat and A. Lemaitre, *Heterogeneities in amorphous systems under shear*, Dynamical heterogeneities in glasses, colloids, and granular media **150** (2011) 264.

[115] A. D. S. Parmar, S. Kumar, and S. Sastry, *Strain localization above the yielding point in cyclically deformed glasses*, Phys. Rev. X **9** (Apr, 2019) 021018. https://link.aps.org/doi/10.1103/PhysRevX.9.021018.

[116] D. Fiocco, G. Foffi, and S. Sastry, *Oscillatory athermal quasistatic deformation of a model glass*, Phys. Rev. E **88** (Aug, 2013) 020301. https://link.aps.org/doi/10.1103/PhysRevE.88.020301.

[117] V. Testard, L. Berthier, and W. Kob, *Influence of the glass transition on the liquid-gas spinodal decomposition*, Physical review letters **106** no. 12, (2011) 125702. https://link.aps.org/doi/10.1103/PhysRevLett.106.125702.

[118] I. Regev, T. Lookman, and C. Reichhardt, *Onset of irreversibility and chaos in amorphous solids under periodic shear*, Physical Review E **88** no. 6, (2013) 062401.

[119] M. Mungan and S. Sastry, *Metastability as a mechanism for yielding in amorphous solids under cyclic shear*, Physical review letters **127** no. 24, (2021) 248002.

[120] D. Kumar, S. Patinet, C. E. Maloney, I. Regev, D. Vandembroucq, and M. Mungan, *Mapping out the glassy landscape of a mesoscopic elastoplastic model*, The Journal of Chemical Physics **157** no. 17, (2022) 174504.

[121] M. Mungan, S. Sastry, K. Dahmen, and I. Regev, *Networks and hierarchies: How amorphous materials learn to remember*, Phys. Rev. Lett. **123** (Oct, 2019) 178002. `https://link.aps.org/doi/10.1103/PhysRevLett.123.178002`.

[122] U. A. Dattani, R. Sharma, S. Karmakar, and P. Chaudhuri, *Cavitation instabilities in amorphous solids via secondary mechanical perturbations*, arXiv preprint arXiv:2303.04529 (2023) .

[123] C. Liu, S. Dutta, P. Chaudhuri, and K. Martens, *Elastoplastic approach based on microscopic insights for the steady state and transient dynamics of sheared disordered solids*, Physical Review Letters **126** no. 13, (2021) 138005.

[124] D. C. Hofmann, J.-Y. Suh, A. Wiest, G. Duan, M.-L. Lind, M. D. Demetriou, and W. L. Johnson, *Designing metallic glass matrix composites with high toughness and tensile ductility*, Nature **451** no. 7182, (2008) 1085–1089.

[125] T. J. Hardin and E. R. Homer, *Microstructural factors of strain delocalization in model metallic glass matrix composites*, Acta Materialia **83** (2015) 203–215.

[126] O. Gendelman, A. Joy, P. Mishra, I. Procaccia, and K. Samwer, *On the effect of microalloying on the mechanical properties of metallic glasses*, Acta materialia **63** (2014) 209–215.

[127] B. P. Bhowmik, S. Karmakar, I. Procaccia, and C. Rainone, *Particle pinning suppresses spinodal criticality in the shear-banding instability*, Phys. Rev. E **100** (Nov, 2019) 052110. `https://link.aps.org/doi/10.1103/PhysRevE.100.052110`.

[128] Y. Liu, H. Liu, and H. Peng, *Pinning effect on the correlations of nonaffine displacement in metallic glasses*, Journal of Non-Crystalline Solids **601** (2023) 122052.

[129] U. A. Dattani, S. Karmakar, and P. Chaudhuri, *Universal mechanical instabilities in the energy landscape of amorphous solids: Evidence from athermal quasistatic expansion*, Physical Review E **106** no. 5, (2022) 055004.

[130] A. Lemaître and C. Caroli, *Rate-dependent avalanche size in athermally sheared amorphous solids*, Phys. Rev. Lett. **103** (Aug, 2009) 065501. `https://link.aps.org/doi/10.1103/PhysRevLett.103.065501`.

[131] S. Karmakar, E. Lerner, I. Procaccia, and J. Zylberg, *Statistical physics of elastoplastic steady states in amorphous solids: Finite temperatures and strain rates*, Phys. Rev. E **82** (Sep, 2010) 031301. `https://link.aps.org/doi/10.1103/PhysRevE.82.031301`.

[132] S. P. Niblett, V. K. de Souza, R. L. Jack, and D. J. Wales, *Effects of random pinning on the potential energy landscape of a supercooled liquid*, The Journal of Chemical Physics **149** no. 11, (2018) 114503, `https://doi.org/10.1063/1.5042140`. `https://doi.org/10.1063/1.5042140`.

[133] A. Argon and H. Kuo, *Plastic flow in a disordered bubble raft (an analog of a metallic glass)*, Materials Science and Engineering **39** no. 1, (1979) 101–109. `https://www.sciencedirect.com/science/article/pii/0025541679901745`.

[134] D. Richard, G. Kapteijns, J. A. Giannini, M. L. Manning, and E. Lerner, *Simple and broadly applicable definition of shear transformation zones*, Phys. Rev. Lett. **126** (Jan, 2021) 015501. `https://link.aps.org/doi/10.1103/PhysRevLett.126.015501`.

[135] L. Gartner and E. Lerner, *Nonlinear plastic modes in disordered solids*, Phys. Rev. E **93** (Jan, 2016) 011001. `https://link.aps.org/doi/10.1103/PhysRevE.93.011001`.

[136] A. Tanguy, B. Mantisi, and M. Tsamados, *Vibrational modes as a predictor for plasticity in a model glass*, Europhysics Letters **90** no. 1, (Apr, 2010) 16004. `https://dx.doi.org/10.1209/0295-5075/90/16004`.

[137] M. L. Manning and A. J. Liu, *Vibrational modes identify soft spots in a sheared disordered packing*, Phys. Rev. Lett. **107** (Aug, 2011) 108302. `https://link.aps.org/doi/10.1103/PhysRevLett.107.108302`.

[138] E. Stanifer and M. L. Manning, *Avalanche dynamics in sheared athermal particle packings occurs via localized bursts predicted by unstable linear response*, Soft Matter **18** no. 12, (2022) 2394–2406.

[139] U. A. Dattani, S. Karmakar, and P. Chaudhuri, *Athermal quasistatic cavitation in amorphous solids: effect of random pinning*, arXiv preprint arXiv:2306.05348 (2023) .

[140] D. Richard, C. Rainone, and E. Lerner, *Finite-size study of the athermal quasistatic yielding transition in structural glasses*, The Journal of Chemical Physics **155** no. 5, (2021) 056101.

[141] R. Das, B. P. Bhowmik, A. B. Puthirath, T. N. Narayanan, and S. Karmakar, *Soft-pinning: experimental validation of static correlations in supercooled molecular glass-forming liquids*, arXiv preprint arXiv:2106.06325 (2021) .